REPORT DOCUMENTATION PAGE

Form Approved OMB No. 0704-0188

Public reporting burden for this collection of information is estimated to average 1 hour per response, including the time for reviewing instructions, searching existing data sources, gathering and maintaining the data needed, and completing and reviewing the collection of information. Send comments regarding this burden estimate or any other aspect of this collection of information, including suggestions for reducing this burden to Washington Headquarters Services, Directorate for Information Operations and Reports, 1215 Jefferson Davis Highway, Suite 1204, Arlington, VA 22202-4302, and to the Office of Management and Budget, Paperwork Reduction Project (0704-0188), Washington, DC 20503.

1. AGENCY USE ONLY (Leave blank)	2. REPORT DATE	3. REPORT TYPE AND DATES COVERED
	14 May 1998	Final Report

4. TITLE AND SUBTITLE	5. FUNDING NUMBERS
Planetary Waves and Mesoscale Disturbances in the Middle and Upper Atmosphere	F6170897W0122
6. AUTHOR(S)	
Dr. Alexander Ivanovich Pogoreltsev	
7. PERFORMING ORGANIZATION NAME(S) AND ADDRESS(ES)	8. PERFORMING ORGANIZATION REPORT NUMBER
Ministry - Academy of Science of Kazakhstan Republic Almaty 480068 Kazakhstan	N/A
9. SPONSORING/MONITORING AGENCY NAME(S) AND ADDRESS(ES)	10. SPONSORING/MONITORING AGENCY REPORT NUMBER
EOARD PSC 802 BOX 14 FPO 09499-0200	SPC 97-4017

11. SUPPLEMENTARY NOTES

12a. DISTRIBUTION/AVAILABILITY STATEMENT	12b. DISTRIBUTION CODE
Approved for public release; distribution is unlimited.	A

13. ABSTRACT (Maximum 200 words)

This report results from a contract tasking Ministry - Academy of Science of Kazakhstan Republic as follows: The contractor will investigate wave motions of different scales in the middle and upper atmosphere.

19980617 114

14. SUBJECT TERMS	15. NUMBER OF PAGES
Space Science, Gravity Waves, Gravity Waves, Mesopause	113
	16. PRICE CODE N/A

17. SECURITY CLASSIFICATION OF REPORT	18. SECURITY CLASSIFICATION OF THIS PAGE	19, SECURITY CLASSIFICATION OF ABSTRACT	20. LIMITATION OF ABSTRACT
UNCLASSIFIED	UNCLASSIFIED	UNCLASSIFIED	UL

NSN 7540-01-280-5500

Standard Form 298 (Rev. 2-89)
Prescribed by ANSI Std. 239-18
298-102

Planetary Waves and Mesoscale Disturbances in the Middle and Upper Atmosphere.

Alexander I. Pogoreltsev
Arthur F. Yakovets
Victor M. Aushev
Malik Z. Kaliev
Dmitry E. Zachateiskiy
Victor V. Vodyannikov
Oleg V. Zukin

Institute of Ionosphere
Ministry – Academy of Science
Republic of Kazakstan

May 14, 1998

This is a final report. Work was performed under special contract SPC-97-4017

DISTRIBUTION STATEMENT A
Approved for public release;
Distribution Unlimited

DTIC QUALITY INSPECTED 1

Special contract SPC-97-4017

Planetary Waves and Mesoscale Disturbances in the Middle and Upper Atmosphere.

Final report

I. Measurements and analysis.

1.1. Emission rate and temperature observations by MORTI.

Mesopause Oxygen Rotational Temperature Imager (MORTI) is ground-based optical instrument for emission rate/temperature measurements by using the molecular oxygen nightglow emission. Its construction was described in details by Wiens et al. (1991). Here we present a general concept of an instrument construction and discuss some preliminary results of observations in Almaty. MORTI uses the (0-1) band of O_2 spectrum around 866.5 nm. The instrument consists of a conical mirror, a Fresnel lens, an interference filter, a photographic lens, and CCD camera. The optical axis of the MORTI is directed vertically and the conical mirror provides a view of the annulus with an inner radius of 47 km and an outer radius of 63 km at altitude of 95 km. The interference filter is centered at 867.6 nm and has bandpass of 0.27 nm. It transmits the O_2 lines with different wavelength at different angular distances from the optical axis forming six concentric rings at the CCD plane corresponding to six pairs of the rotational lines. CCD (charge coupled device) camera operates as a detector of the sky image. The radial distribution of the image intensity contains the information on a rotational temperature, and integration of the intensity radially over the image gives the emission rate for the corresponding sky region. Evaluations show that the emission rate/temperature measurements have a precision of $\pm$ 2% and $\pm$ 2 K, respectively. Passing overhead acoustic-gravity waves (AGW) modulate the rotational temperature and the emission rate so the temporal behaviour of these parameters gives the information on AGW frequency spectra and their spatial characteristics. In order to estimate the AGW frequency spectra the temperature and emission rate are processed by a Fourier analysis. To obtain information on an azimuth and a phase speed of the AGW propagation the sky field of view is divided into 12 sectors, and time series of the temperature and emission rate in these sectors have to be used for estimation of the AGW propagation characteristics. The apparent phase differences between similar signatures from the various image sectors give the information on the azimuth of AGW propagation and phase speed.

The interference spectro-photometer MORTI, using advanced CCD imaging technology, has been installed at the Institute of Ionosphere in September 1997. Since October 1997 until April 1998 the compaign type measurements (10-12 days a month) were carried out during clear sky nights when the moon was not full. To obtain the images we used 5 min exposure time. A distance of 10 km between Almaty city and Institute of Ionosphere ensure good conditions and effectively abolished the background illumination.

The following tables show the statistics of our observations

October 1997

23 (321 min)	clouds
24 (376 min)	clouds
25 (432 min)	clouds
26 (681 min)	clear sky
27 (683 min)	clear sky
28 (685 min)	clear sky
29 (688 min)	clear sky
30 (690 min)	clear sky
31 (693 min)	clear sky

November 1997

1 (695 min)	clear sky
2 (697 min)	clouds
3 (700 min)	clear sky
4 (702 min)	clouds
5 (704 min)	clouds
6 (520 min)	clouds
7 (461 min)	clouds
8 (398 min)	clouds
9 (333 min)	clouds

November 1997

21 (331 min)	clouds
22 (387 min)	clouds
23 (442 min)	clouds
24 (498 min)	clear sky
25 (743 min)	clear sky
26 (744 min)	clear sky
27 (745 min)	clear sky
28 (747 min)	clear sky
29 (749 min)	clear sky
30 (750 min)	clear sky

December 1997

1 (751 min)	clouds
2 (752 min)	clouds
3 (753 min)	clouds
4 (754 min)	clouds
5 (556 min)	clear sky
6 (492 min)	clear sky
7 (427 min)	clear sky
8 (361 min)	clear sky

December 1997

21 (359 min)	clouds
22 (413 min)	clouds
23 (468 min)	clouds
24 (523 min)	clear sky
25 (764 min)	clouds
26 (763 min)	clouds
27 (763 min)	clouds
28 (763 min)	clouds
29 (762 min)	clouds
30 (762 min)	clouds
31 (762 min)	clear sky

January 1998

1 (761 min)	clouds
2 (760 min)	clear sky
3 (759 min)	clouds
4 (511 min)	clouds
5 (444 min)	clouds
6 (378 min)	clouds

January 1998

21 (413 min)	clear sky
22 (469 min)	clouds
23 (525 min)	clear sky
24 (581 min)	clouds
25 (730 min)	clear sky
26 (728 min)	clouds
27 (726 min)	clouds
28 (724 min)	clouds
29 (722 min)	clear sky
30 (720 min)	clear sky
31 (718 min)	clear sky

February 1998

1 (716 min)	clouds
2 (496 min)	clear sky
3 (429 min)	clear sky
4 (361 min)	clear sky

February 1998

19 (362 min)	clear sky
20 (418 min)	clouds
21 (473 min)	clouds
22 (526 min)	clouds
23 (663 min)	clouds
24 (660 min)	clear sky
25 (657 min)	clouds
26 (654 min)	clear sky
27 (652 min)	clear sky
28 (649 min)	clear sky

March 1998

1 (646 min)	clouds
2 (643 min)	clouds
3 (640 min)	clouds
4 (383 min)	clouds

March 1998

19 (266 min)	clear sky
20 (321 min)	clouds
21 (373 min)	clouds
22 (423 min)	clouds
23 (471 min)	clear sky
24 (577 min)	clouds
25 (574 min)	clouds
26 (571 min)	clouds
27 (568 min)	clouds
28 (565 min)	clouds
29 (562 min)	clouds
30 (558 min)	clear sky
31 (555 min)	clouds

April 1998

1 (552 min)	clouds
2 (290 min)	clear sky
3 (269 min)	clear sky

1.2. Periodogram analysis of MORTI data.

Lomb-Scargle (LS) periodogram analysis (Lomb, 1976; Scargle, 1982) was first applied to assess the statistically significant oscillations present in the data (Press and Teukolsky, 1988). A quadratic fit was subtracted from each data set to remove trends whose periods were commensurate with the data set length. This was necessary to minimize spectral leakage and to preserve the probability distribution of the periodogram (Scargle, 1982; Horne and Baliunas, 1986). The typical examples of the data observed over Almaty (43.6 N, 76.6 E) and the results of the periodogram analysis are shown in Figs. 1-8. Two groups of statistically significant (> 99% confidence level) peaks appear in Figs. 1-8. The lower frequency group corresponds to the periods of 5-9 hours (Figs. 1-4, 7, 8). These variations are most likely due to the tidal (6h and/or 8h) oscillations similar to reported by Wiens et al. (1995) and Ozonovich et al. (1997). The higer frequency group corresponds to the periods of 2-3 hours (Figs. 5, 6), and these variations are due to the AGW propagation at the mesopause heghts.

Krassovsky's ratio η (1972) is a complex quantity which can be considered as a transfer function between planetary wave, tidal, or AGW driven temperature oscillations and resultant emission rate oscillations. In a ground-based measurements the parameter η may be expressed as follows (Zhang et al., 1993b)

$$\eta = \frac{B'/B_0}{T'_m/T_0} = \frac{\int_0^\infty \varepsilon' dz}{\int_0^\infty \varepsilon_0 T'/T_0 dz}, \tag{1}$$

where B is the apparent emission rate, T_m is the measured temperature weighted by the apparent emission rate, and ε is the volume emission rate. The subscript zero denotes the unperturbed values and the perturbations are denoted by a prime. The phase of Krassovsky's ratio is given by relative phase of the emission rate and temperature oscillations $\varphi_\eta = \varphi_B - \varphi_T$. Confusion exists in regard to the sign of the phase of Krassovsky's ratio For instance, in the paper Zhang et al. (1993a) on can read that "when $\varphi_\eta > 0$, the temperature leads the emission rate; when $\varphi_\eta < 0$ the emission rate leads" (see page 369), however, when the authors discuss the phase of Krassovsky's ratio predicted by the theory (for most cases the phase is negative), they make a conclusion that "the temperature fluctuations lead the column emission rate fluctuations for all wavelengths and periods" (Zhang et al., 1993b, page 388). It seems that source of this ambiguity is a possibility to determine the phase of Fourier components in time series by two different ways: as the cosine argument of $y(t)$ at the time t=0, where $y(t) = A\cos(\omega t + \varphi)$, A is amplitude, and φ is the phase (Hocke, 1998); or as a position of the maximum, i.e., $y(t) = A\cos(\omega t - \varphi)$ (Ozonovich et al., 1997). Another possible source of the confusion is the different choice of sign in the presentation of perturbations by plane waves. To avoid the ambiguity connected with the sign of the phase of Krassovsky's ratio we adopt the following

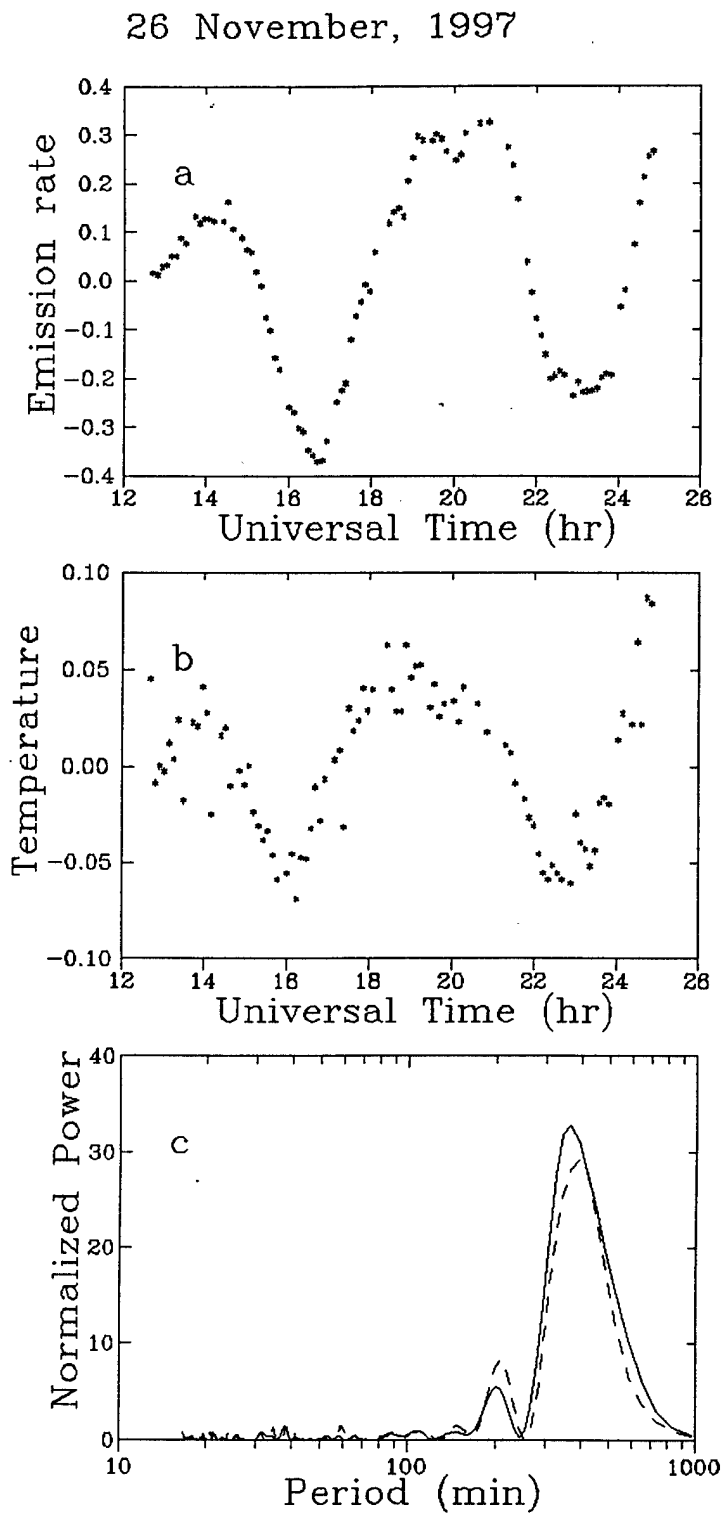

Figure 1: The relative emission rate (a) and rotational temperature (b). The normalized LS periodograms (c) from B'/B_0 – solid line and T'_m/T_0 – dashed line for the data observed over Almaty on Nov. 26 to Nov. 27, 1997. The quadratic trends are removed.

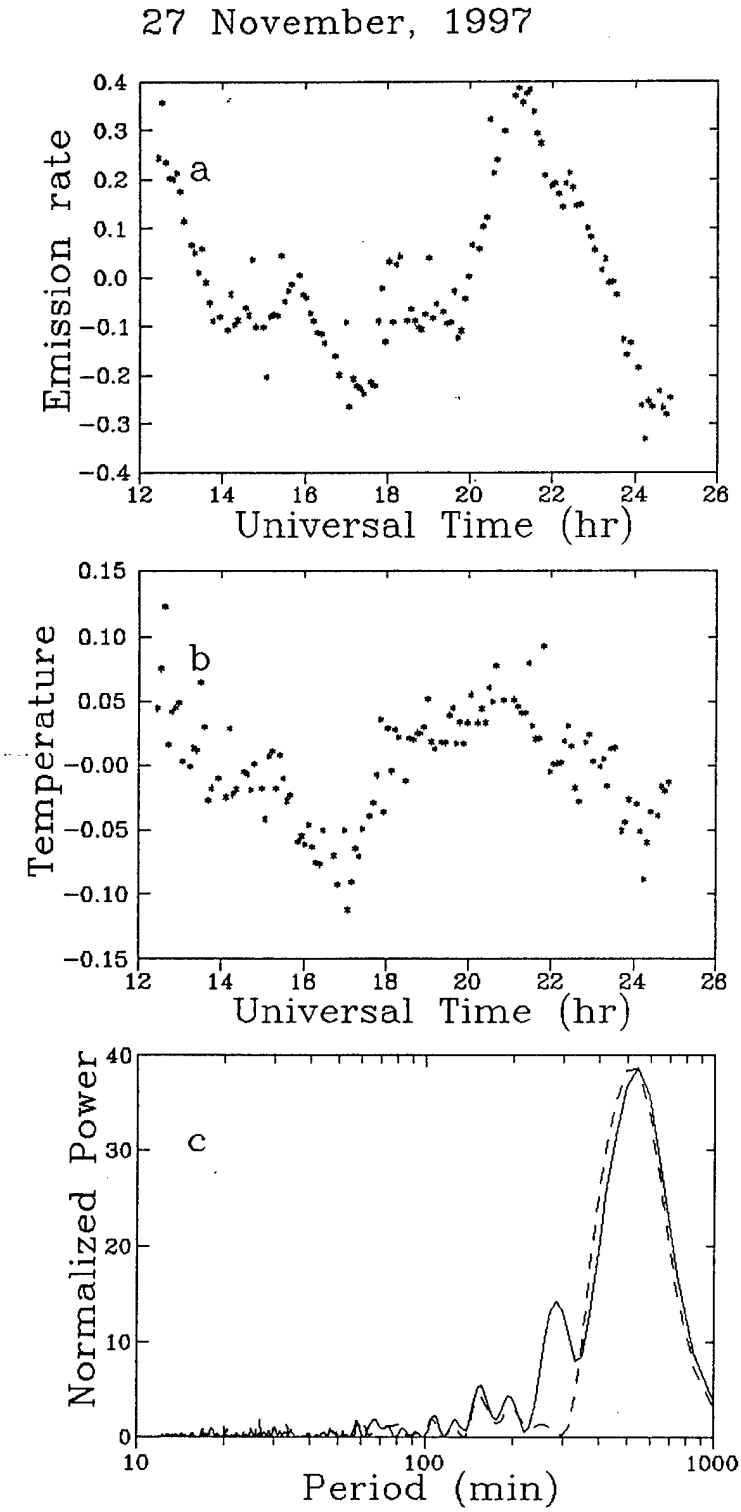

Figure 2: As in Fig. 1, but for the data observed on Nov. 27 to Nov. 28, 1997.

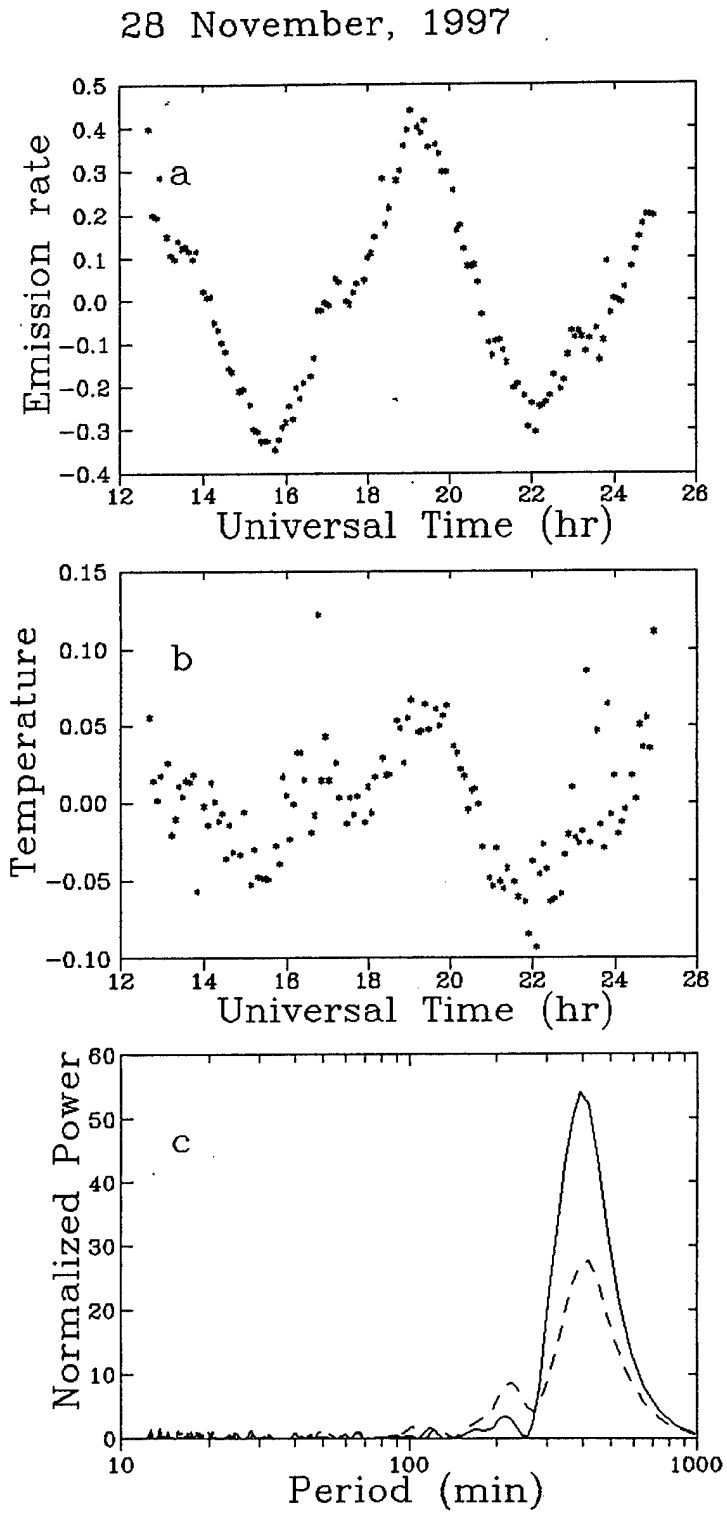

Figure 3: As in Fig. 1, but for the data observed on Nov. 28 to Nov. 29, 1997.

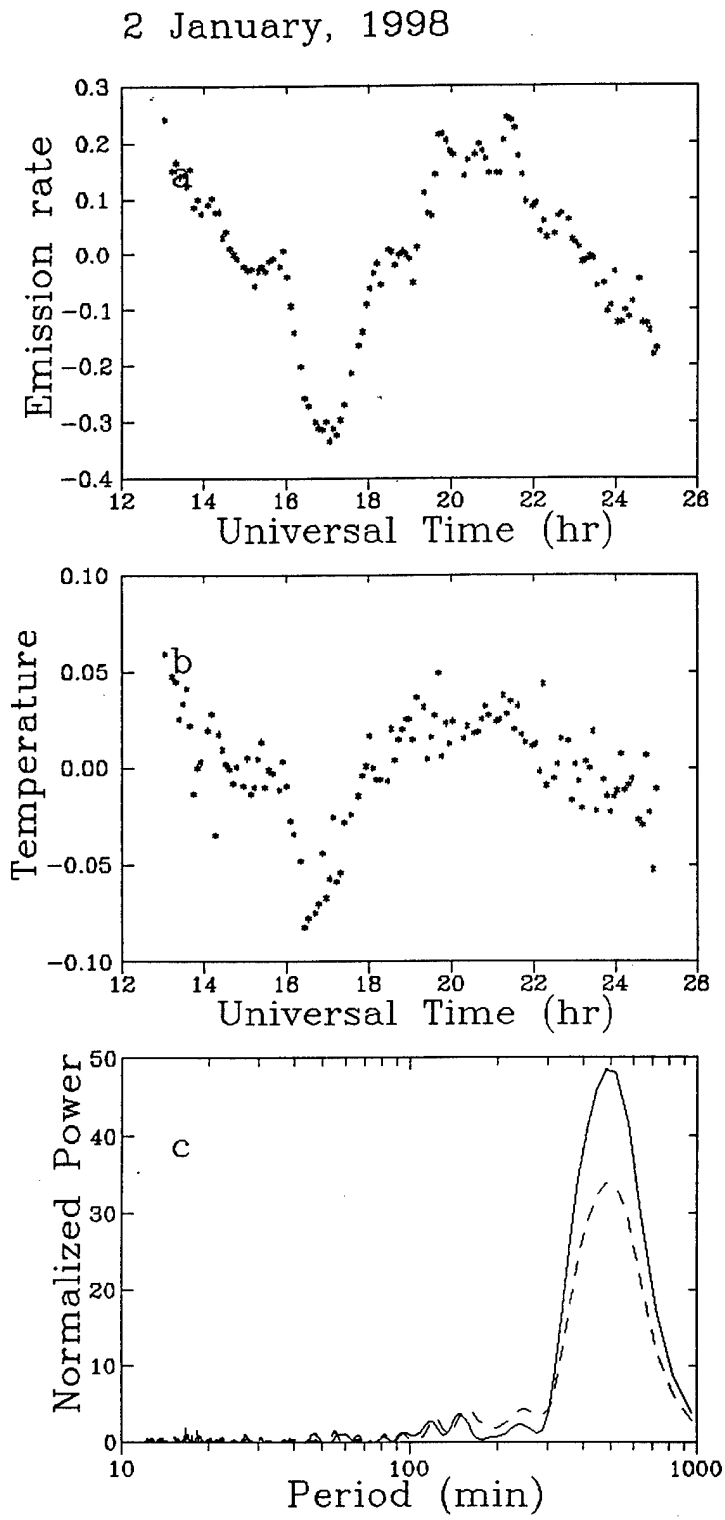

Figure 4: As in Fig. 1, but for the data observed on Jan. 2 to Jan. 3, 1998.

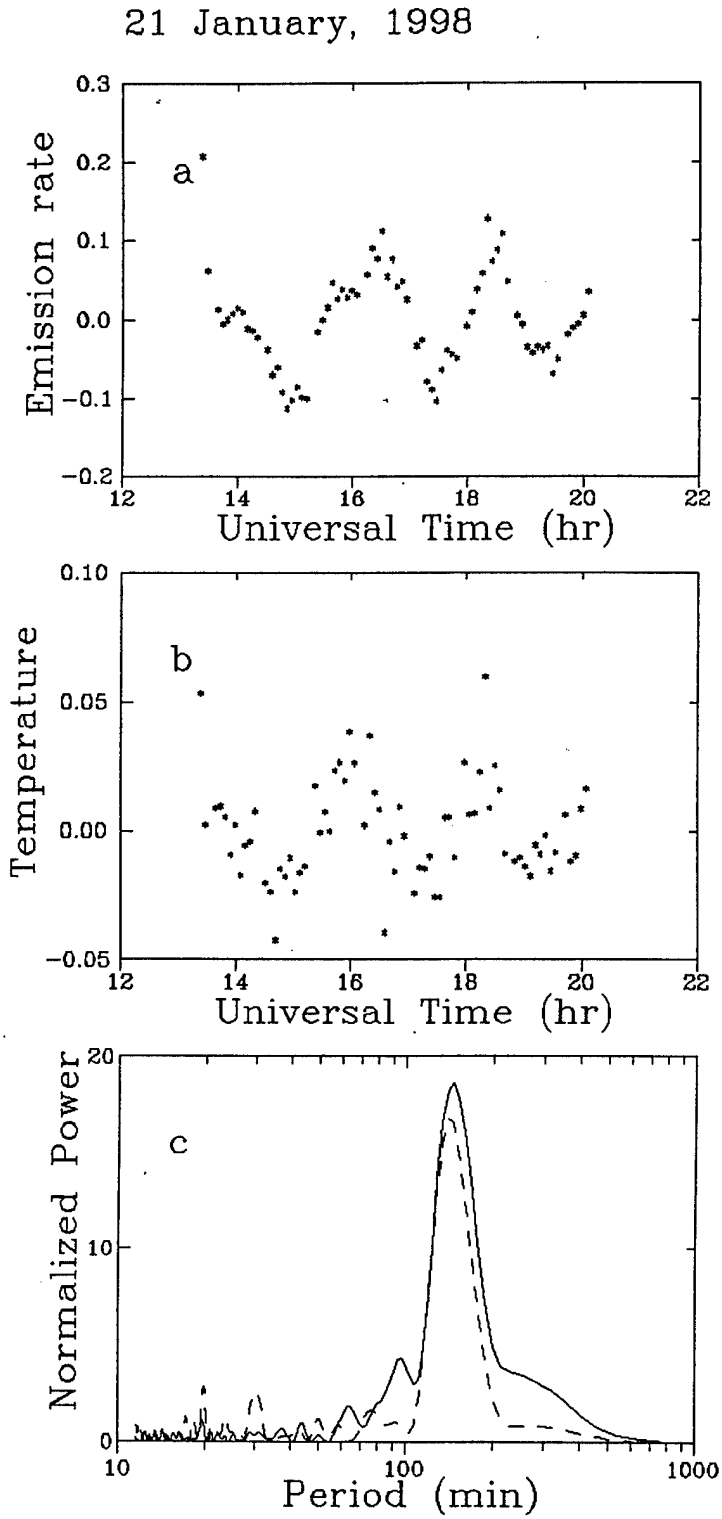

Figure 5: As in Fig. 1, but for the data observed on Jan. 21 to Jan. 22, 1998.

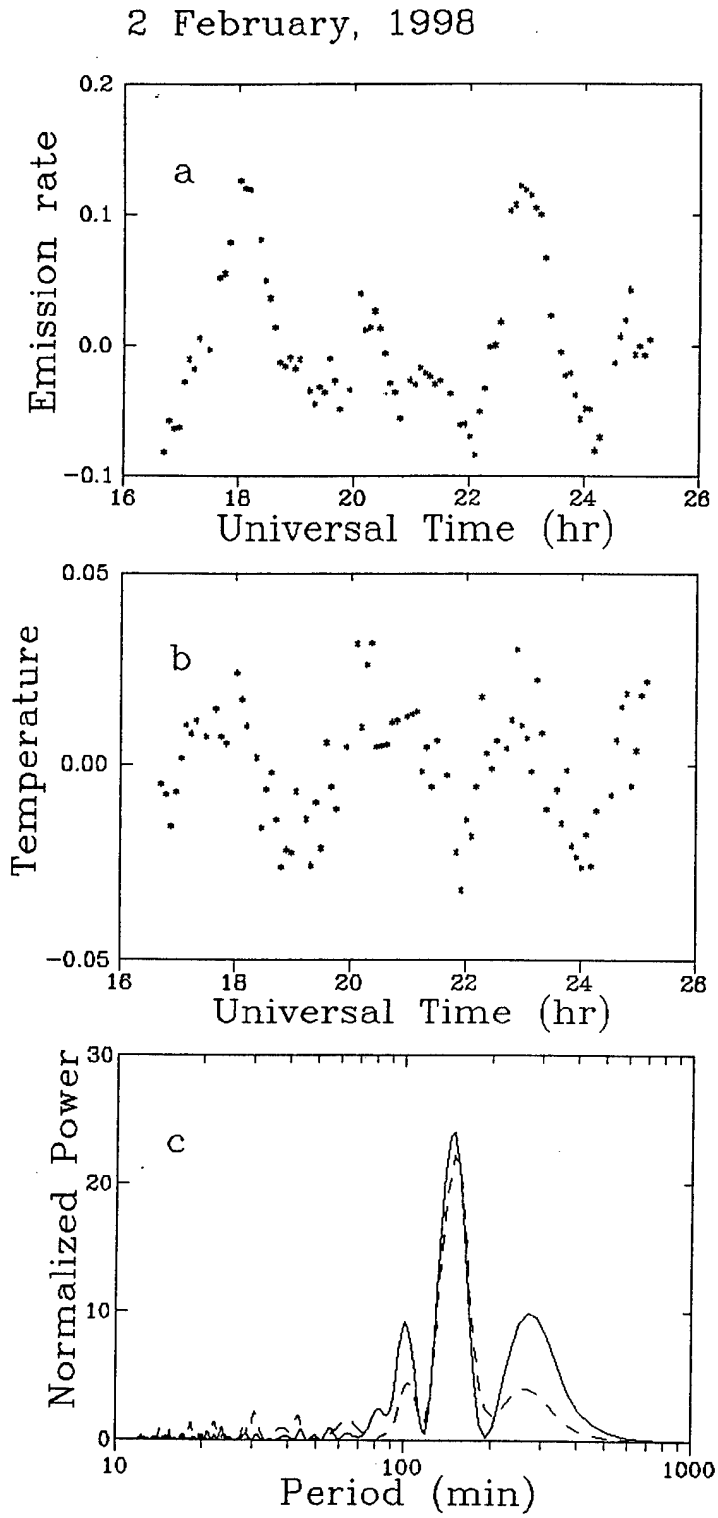

Figure 6: As in Fig. 1, but for the data observed on Feb. 2 to Feb. 3, 1998.

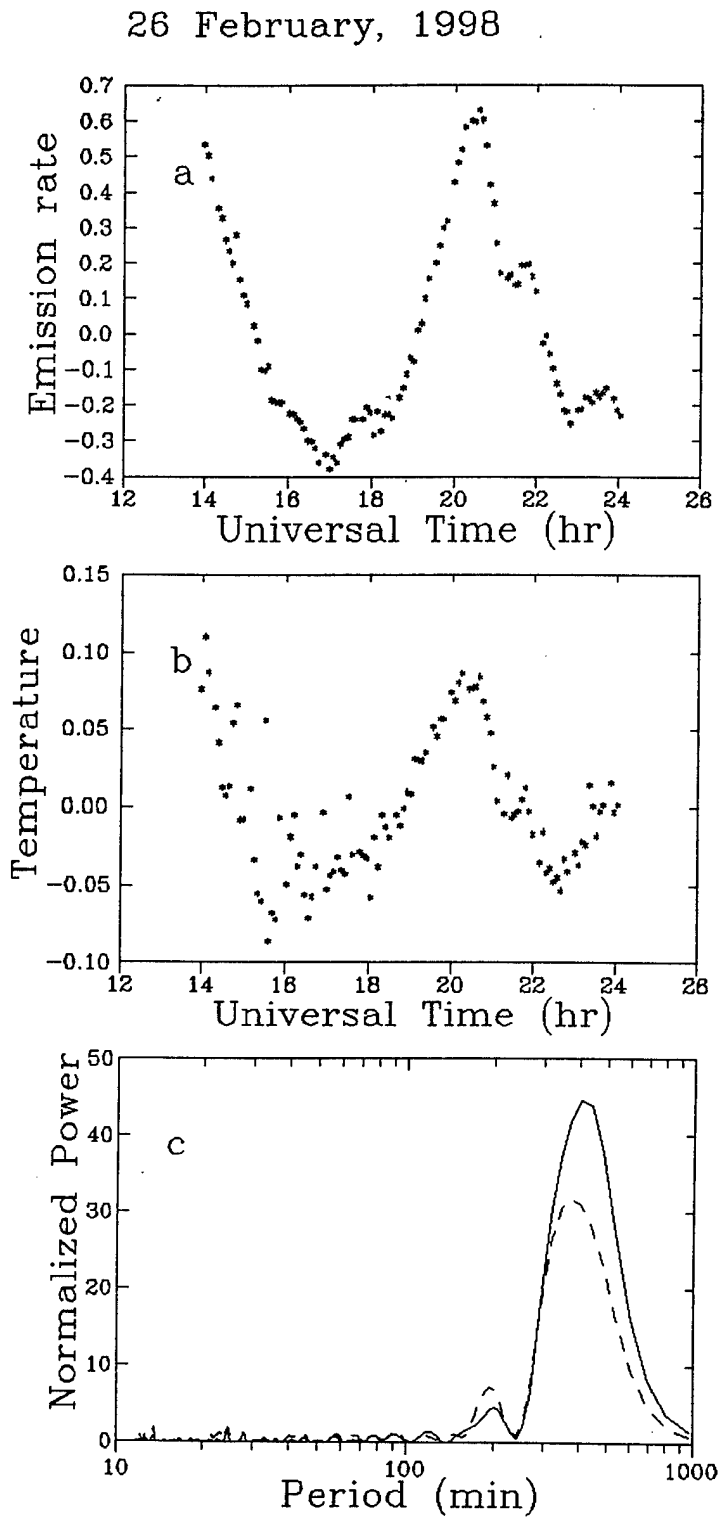

Figure 7: As in Fig. 1, but for the data observed on Feb. 26 to Feb. 27, 1998.

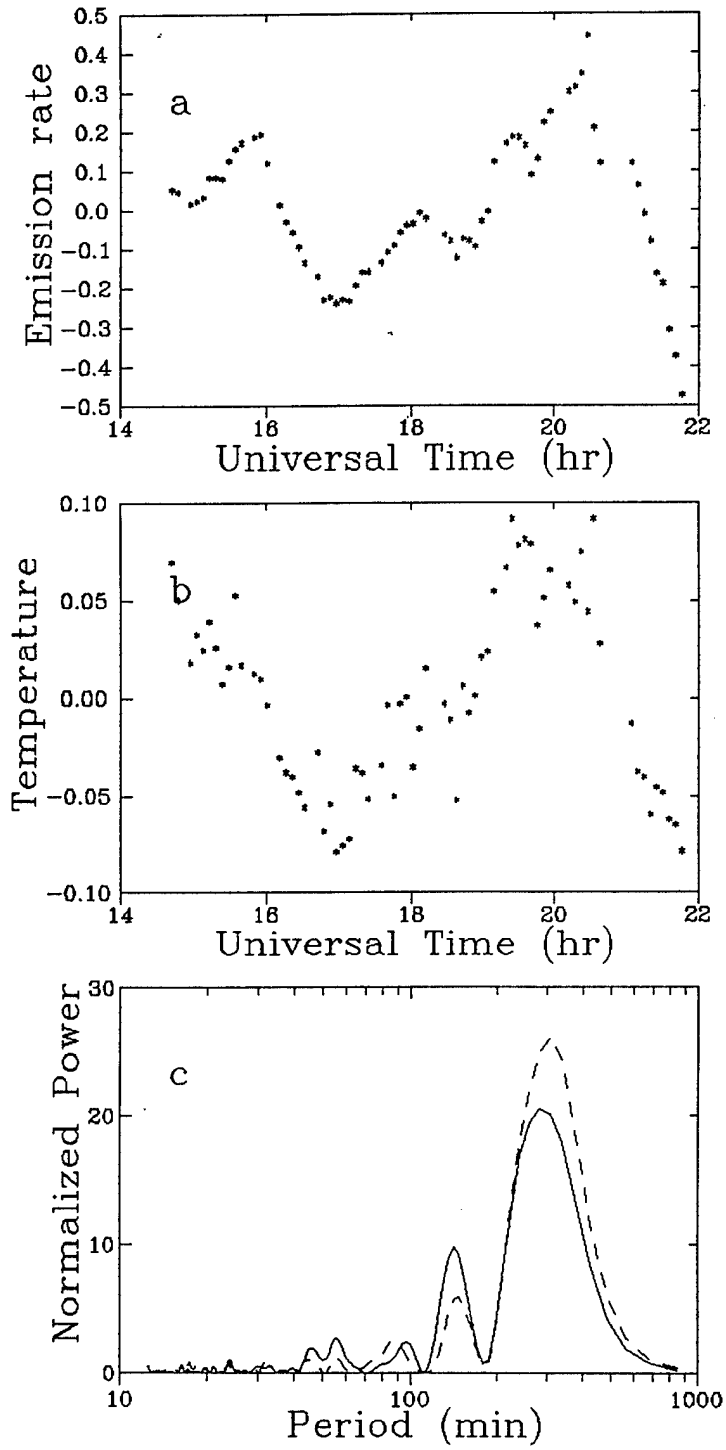

Figure 8: As in Fig. 1, but for the data observed on March 23 to March 24, 1998.

presentation of perturbed quantities

$$f'(x,z,t) = f_{k_x,\omega}(z)e^{i(k_x x-\omega t)} = |f_{k_x,\omega}|e^{i(k_x x-\omega t+\varphi)}, \tag{2}$$

where the phase $\varphi(z)$ is the argument of complex amplitude $f_{k_x,\omega}(z)$. It is possible to show that such determination of the phase of the wave is equivalent to the second determination of the phase in Fourier analysis of time series, i.e., $y(t) = A\cos(\omega t - \varphi)$. In our determination the phase of Krassovsky's ratio is positive if the temperature leads the emission rate, and negative if the emission rate leads the temperature. It is necessary also to note that our agreement is different from the one traditionally accepted in the papers on airglow emissions, but usually it is accepted in the hydrodynamics.

In order to obtain the amplitude and phase of Krassovsky's ratio from the experimental data, we used the LS periodogram method for estimation the amplitude and phase spectra (Hocke, 1998). The results obtained with data shown in Fig. 1-8 are presented in Table 1.

Table 1

Date	Period (min)	B'/B_0 (percent)	T'/T_0 (percent)	$\|\eta\|$	φ_η (deg)
26.11.97	377.3	23.7	4.2	5.7	37.8
	198.0	5.9	1.6	3.6	30.1
	102.5	2.6	Uncert.	Uncert.	Uncert
27.11.97	541.5	20.2	4.8	4.2	16.6
	297.8	8.2	Uncert.	Uncert.	Uncert.
	165.4	6.5	1.5	4.4	17.9
28.11.97	406.4	27.8	3.9	7.1	21.8
	183.5	5.0	Uncert.	Uncert.	Uncert.
	127.9	3.3	Uncert.	Uncert.	Uncert.
2.01.98	479.2	18.4	3.0	6.1	10.3
	250.0	3.8	Uncert.	Uncert.	Uncert.
	166.5	3.7	1.15	3.2	2.7
21.01.98	142.8	6.3	1.9	3.3	32.2
	100.3	2.7	Uncert.	Uncert.	Uncert.
2.02.98	149.8	5.9	1.6	3.8	22.1
	102.4	3.5	0.65	5.3	6.4
26.02.98	388.8	35.5	4.9	7.3	20.2
	206.4	9.1	1.9	4.9	11.3
	127.6	4.4	Uncert.	Uncert.	Uncert.
	83.6	4.3	Uncert.	Uncert.	Uncert.
23.03.98	295.5	19.1	5.8	3.3	19.7
	154.1	8.1	Uncert.	Uncert.	Uncert.
	99.7	4.9	Uncert.	Uncert.	Uncert.
	65.2	4.3	Uncert.	Uncert.	Uncert.
	54.7	3.9	Uncert.	Uncert.	Uncert.

This table shows that in general the amplitude of the emission rate and temperature oscillations decreases with the decreasing of the wave period. The comparison of $|\eta|$ and φ_η obtained from our measurements with the ones obtained in other investigations (Zhang et al., 1993a,b; Ozonovich et al., 1997) shows a good agreement. The largest amplitudes of Krassovsky's ratio are obtained for long-period waves (28.11.97 and 26.02.98), but clear dependences of the amplitude and phase of η on the wave period are not evident. Perhaps the later is due to different nature of long period waves [migrating and nonmigrating tides or inertia-gravity waves, see the discussion in Ozonovich et al. (1997) and Lindzen (1984)]. In all cases the phase of Krassovsky's ratio is positive and the temperature variations leads the emission rate variations. Our results also show that the determination of the wave parameters from the measurements of the emission rate variations is more reliable then from the measurement of the temperature, because the temperature fluctuations are not as large as the emission rate fluctuations (the amplitude of Krassovsky's ratio changes from 3 to 7). However, it is necessary to note that thin tropospheric clouds can change the measured emission rate without appreciably changing the measured rotational temperature, because we see no reason that the clouds would change the spectral distribution from which we determine the temperature (Wiens et al., 1991).

Numerical calculations of Krassovsky's ratio were performed using the approach considered in Zhang et al. (1993b). The AGW propagation at the mesopause heights was simulated with the numerical model developed by Bidlingmayer and Pogoreltsev (1992). The AGW simulations were performed for nonisothermal atmosphere, but without account of the background wind. It is possible to include the background wind into consideration (Pogoreltsev and Pertsev, 1995), but we have not yet the software for devision of images into 12 sectors and we cannot determine the azimuth of AGW propagation (Dr. Rudy Wiens promissed to provide us with this software shortly). The calculations were carried out for the model atmosphere (Hedin et al., 1996).

Table 2 lists theoretical calculations of the amplitude and phase of Krassovsky's ratio.

Table 2

Frequency rad/sec	λ_x km	$\|\eta\|$	φ_η (deg)
$7 \cdot 10^{-4}$ (T=150 min)	600	6.96	54.8
	1000	4.54	38.3
	1400	4.16	27.4
$2.5 \cdot 10^{-4}$ (T=400 min)	2000	5.87	50.7
	3000	4.53	35.8
	4000	4.20	26.2
	5000	4.17	17.2

One can see that the results of simulation are reasonable and can explain the most of experimental results listed in Table 1.

1.3. Cophase analysis of MORTI data.

Although we cannot apply directly the sector analysis to the MORTI data obtained in Almaty, it is possible to develop the software which will be used in future, when we will have the program of division the MORTI image into 12 sectors. For this purpose MORTI data obtained at Bear Lake Observatory in January 1993 (Wiens et al., 1997) have been used. The MORTI image maps an annular field of view down to a solid circle in which azimuth is preserved. By analyzing each image in 12 sectors, 12 time series become available in relative temperature and relative column emission rate for fixed point of sky. The amplitude and phase spectra can be found by modified LS periodogram method for each of these 12 sectors. Knowing the phase distribution of the wave (the variations with the frequency of maximum in the power spestrum of periodogram) around the annulus, the propagation direction (azimuth) and horizontal phase speed can be determined by algorithm described by Zhang et al. (1993a). This algorithm is based on the last squares fitting. Here we will discuss the new approach to the analysis of the amplitude and phase spectra in 6 sectors which is based on the COPHASE method (Posmentier and Herrmann, 1971; Montes and Posmentier, 1971).

COPHASE, an ad hoc statistic characterizing signal strength as a function of velocity and direction, for data from an array of detector receiving a signal and uncorrelated noise, has been defined by Posmentier and Herrmann (1971) as follows

$$C(V,\theta) = \frac{\sum_{n=N_1}^{N_2} \sum_{j=k+1}^{K} \sum_{k=1}^{K-1} [A_j(\omega_n) + A_k(\omega_n)] \cos[(\varphi_j^F - \varphi_k^F) - (\varphi_j^V - \varphi_k^V)]}{\sum_{n=N_1}^{N_2} \sum_{j=k+1}^{K} \sum_{k=1}^{K-1} [A_j(\omega_n) + A_k(\omega_n)]}, \tag{3}$$

where V is the assumed phase speed; θ is the assumed azimuth from which signal arrives (note that in our realization the azimuth indicate the direction to what signal propagates); n is the index of frequency (frequencies in the band from the N_1'th to the N_2'th harmonic are used); j is the station number (there are K stations; ω_n is the n'th frequency; $A_j(\omega_n)$ is the n'th Fourier amplitude at the j'th detector; φ_j^F is the n'th Fourier phase at the j'th detector; φ_j^V is the phase of the n'th frequency, arriving at the j'th detector, based on the position of the detector and the assumed values of V and θ.

Basically, $C(V,\theta)$ calculates the normalized, weighted sum over all $\frac{1}{2}K(K-1)$ detector pairs, and over all frequencies, of the cosines of the difference between the Fourier phase differences and the assumed phase differences. Note that $C(V,\theta)$ is a statistic with an expectation of 0 if the K records are non-correlated, and an expectation 0f +1.0 if the K records represent a non-dispersive propagating signal, at the assumed value of V and θ corresponding the the actual velocity and direction of the signal. COPHASE technique was successfully aplied to the analysis of seismic Rayleigh waves and acoustic signals generated by the Saturn-Apollo rocket launches (Montes and Postmentier, 1971). In the case of MORTI data we have 12 records for each sectors and COPHASE technique can be directly applied to the analysis of atmospheric

waves. However, to exclude the errors due to small phase differences in neighbour sectors, we used only 6 pairs of opposite sectors to calculate $C(V,\theta)$. Besides, in the case if the amplitude of considered harmonic fore some sector is small in comparison with the amplitude of this harmonic in the record of data averaged over 12 sectors, the corresponding pair is excluded from the consideration.

The relative airglow column emission rate, O_2 rotational temperature, and results of LS periodogram analysis applied to the averaged over all sectors MORTI data obtained at Bear Lake Observatory on January 20, 1993 are shown in Fig. 9. One can see well defined maxima in the relative emission rate and temperature power spectra at the period of 180 min. The periodogram analysis of data for each of 12 sectors shows the presence of these maxima in all time series. A contour plots of COPHASE for the emission rate and temperature are shown in Fig. 10. The calculations were made for velocities from 100 to 400 m/s and include 5 harmonics (from 171 to 195 min periods). COPHASE analysis indicates that atmospheric wave was propagating with a horizontal phase speed of about 250 m/s and that azumuth of the propagation was $50^0 \pm 10^0$ counterclockwise from the first sector. Unfortunately, we do not know now what was the orientation of the MORTI sectors at Bear Lake Observatory. Fig. 10 also shows that the results obtained by COPHASE analysis applied to the column emission rate and temperature data are very similar. The values of azimuth and horizontal phase speed obtained by COPHASE technique and last squares method (Zhang et al., 1993a) are presented in Table 3.

Table 3

Bear Lake January 20-21, 1993		Azimuth deg	Phase speed m/s
Emission rate	COPHASE	35	250
	Last squares	33	247
Temperature	COPHASE	60	250
	Last squares	25	486

This table shows that COPHASE analysis is more reliable for determination of the azimuth of propagation and horizontal phase speed of atmospheric waves then last squares method (the differences between the values obtained from the emision rate and temperatire data are smaller). Using the value of the horizontal phase speed from Table 3 we can estimate the horizontal wave length of considered disturbance $\lambda_h = c_h T$=2700 km. This wave length is significantly larger then the distance between the points in the mesopause region from what we registrate the column emission rate (for opposite sectors this distance is about 110 km). In result the phase shifts are very small ($\ll 360^0$) and small errors in determination of the phase due to influence of long period harmonics can change the final result substantially. To avoid the influence of long period harmonics (T= 497.9, 288.3 min, see Fig. 9c), we removed these harmonics from the time series using last squares fitting and repeat the COPHASE analysis. The relative emission rate, temperature, and results of LS periodogram analysis applied to the averaged over all sectors data after removing quadratic trends and two long period harmonics from time series

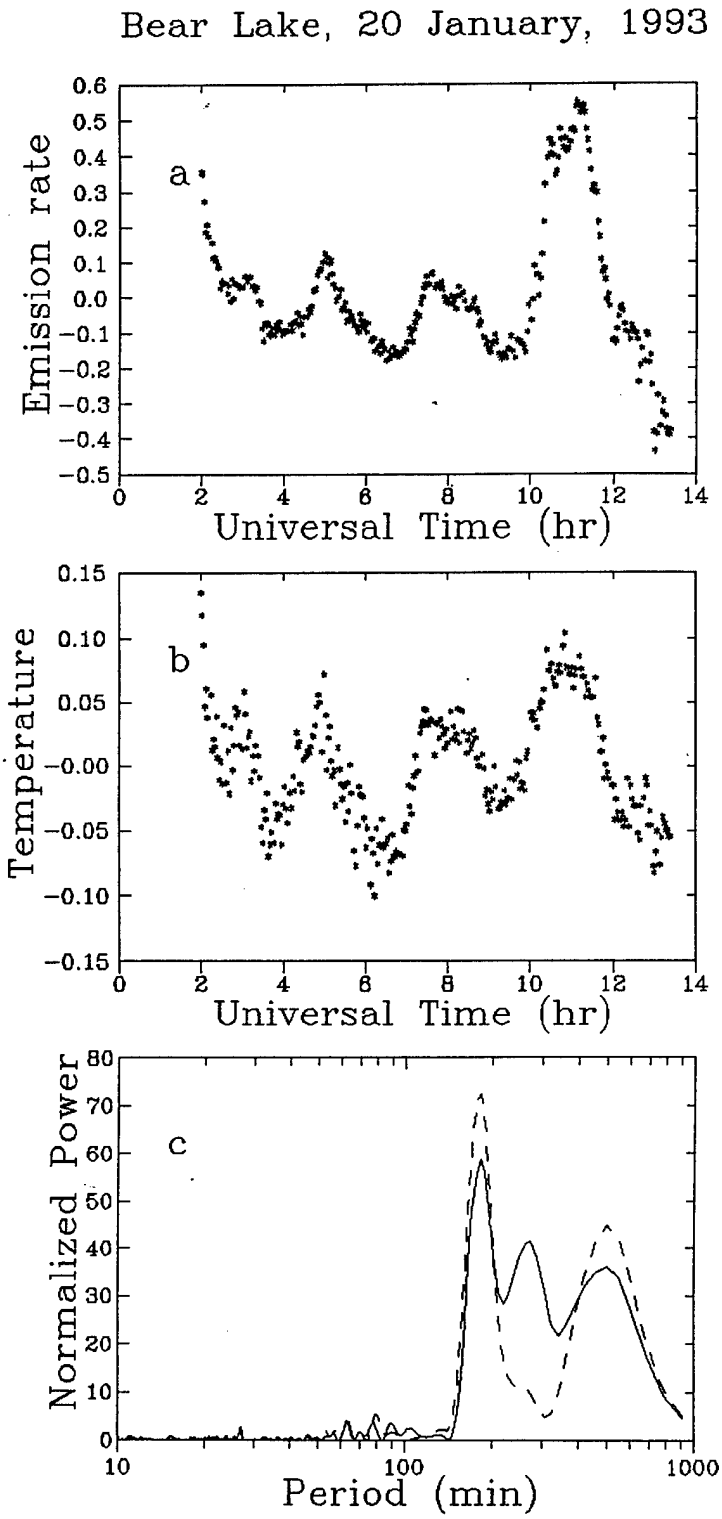

Figure 9: The relative emission rate (a) and rotational temperature (b). The normalized LS periodograms (c) from B'/B_0 – solid line and T'_m/T_0 – dashed line for the data observed at Bear Lake Observatory on Jan. 20 to Jan. 21, 1993. The quadratic trends are removed.

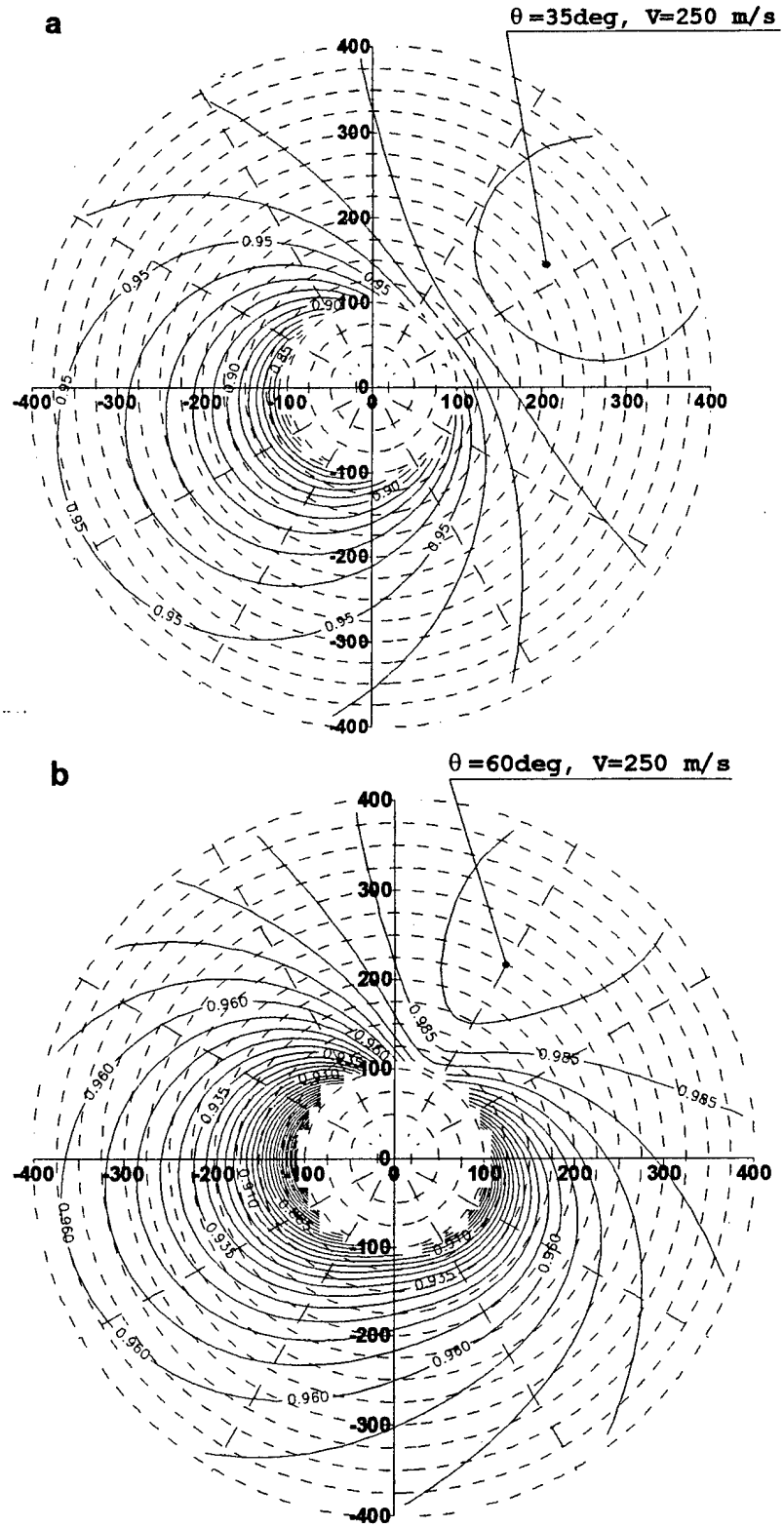

Figure 10: COPHASE of the emission rate (a) and temperature (b). The calculations include 5 harmonics (from 171 to 195 min periods). Radius is velocity, from 100 to 400 m/s in steps of 10 m/s. Contour intervals are 0.01 for emission rate and 0.005 for temperature.

are shown in Fig. 11. The results of COPHASE analysis applied to the amplitude and phase spactra for 12 sectors time series after similar procedure are shown in Fig. 12. The values of azimuth and horizontal phase speed obtained by COPHASE technique and last squares method (Zhang et al., 1993a) applied to the data after removing two long period harmonics from time series are presented in Table 4.

Table 4

Bear Lake January 20-21, 1993		Azimuth deg	Phase speed m/s
Emission rate	COPHASE	45	135
	Last squares	43	130
Temperature	COPHASE	60	165
	Last squares	44	274

The comparison of Figures 10, 12 and the results listed in Tables 3, 4 shows that long period variations strongly influence on the accuracy of the phase speed determination by COPHASE and last squares methods. The results obtained from the time series without long period variations (Fig. 12, Table 4) show that true values of horizontal phase speed and wave length are appoximately half as much as the values obtained from initial data. Besides, the maxima in COPHASE analysis become better defined and localized. The results obtained by last squares method applied to the emission rate time series show good agreement with COPHSE analysis, but the determination of azimuth and phase speed is incorrect for temperature data. Thus we can conclude that COPHASE technique is more reliable and useful for analysis of MORTI data then last squares method, and especially this may be important if we have not so good time series as the ones presented in Figures 9, 11 (for instance, when there are thin tropospheric clouds and/or faint background illumination).

Acknowledgements – We are grateful to Prof. G.G.Shepherd and Dr. R.H.Wiens for providing us with the MORTI instrument, usefull discussion of results, and for sending MORTI data obtained at Bear Lake Observatory.

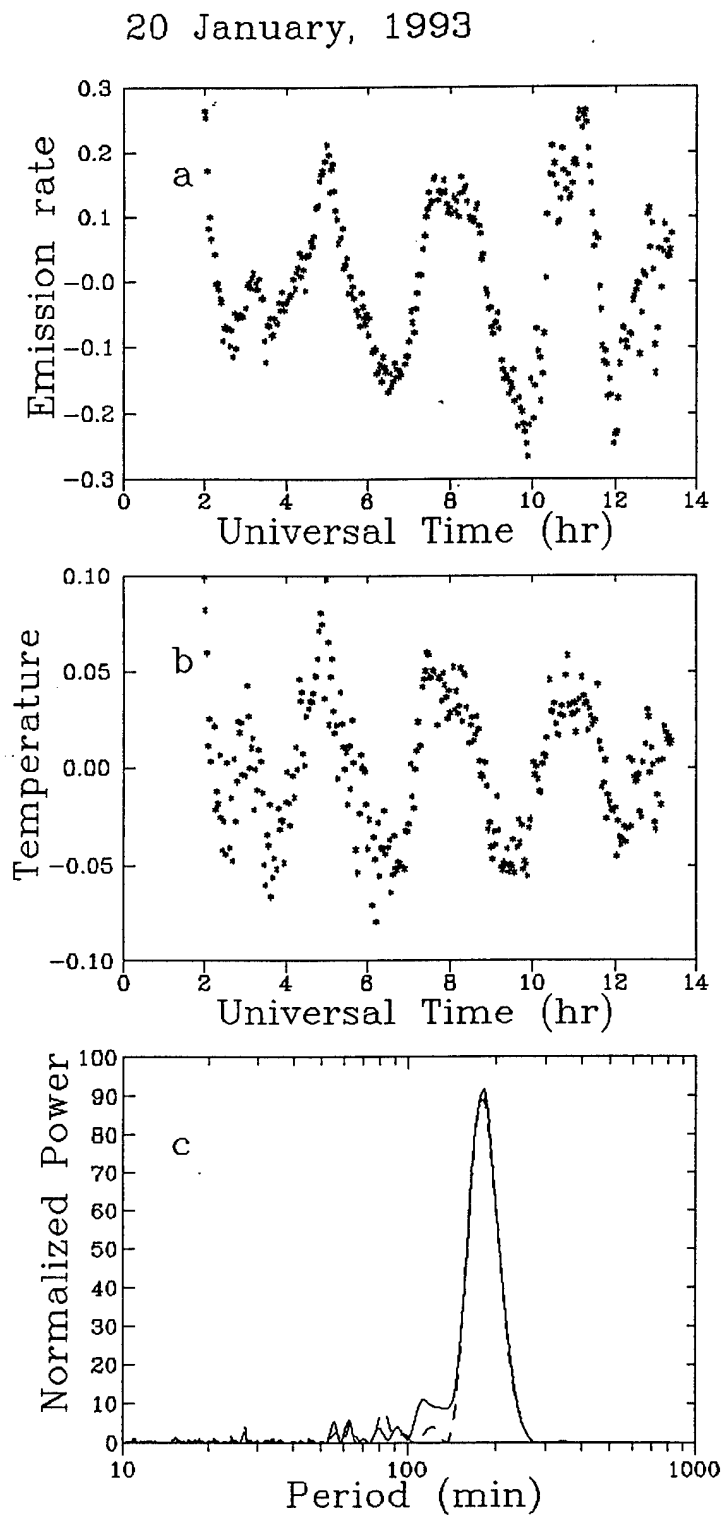

Figure 11: As in Fig. 9, but two long period harmonics ($T = 497.9, 288.3$ min) were removed by last squares fitting.

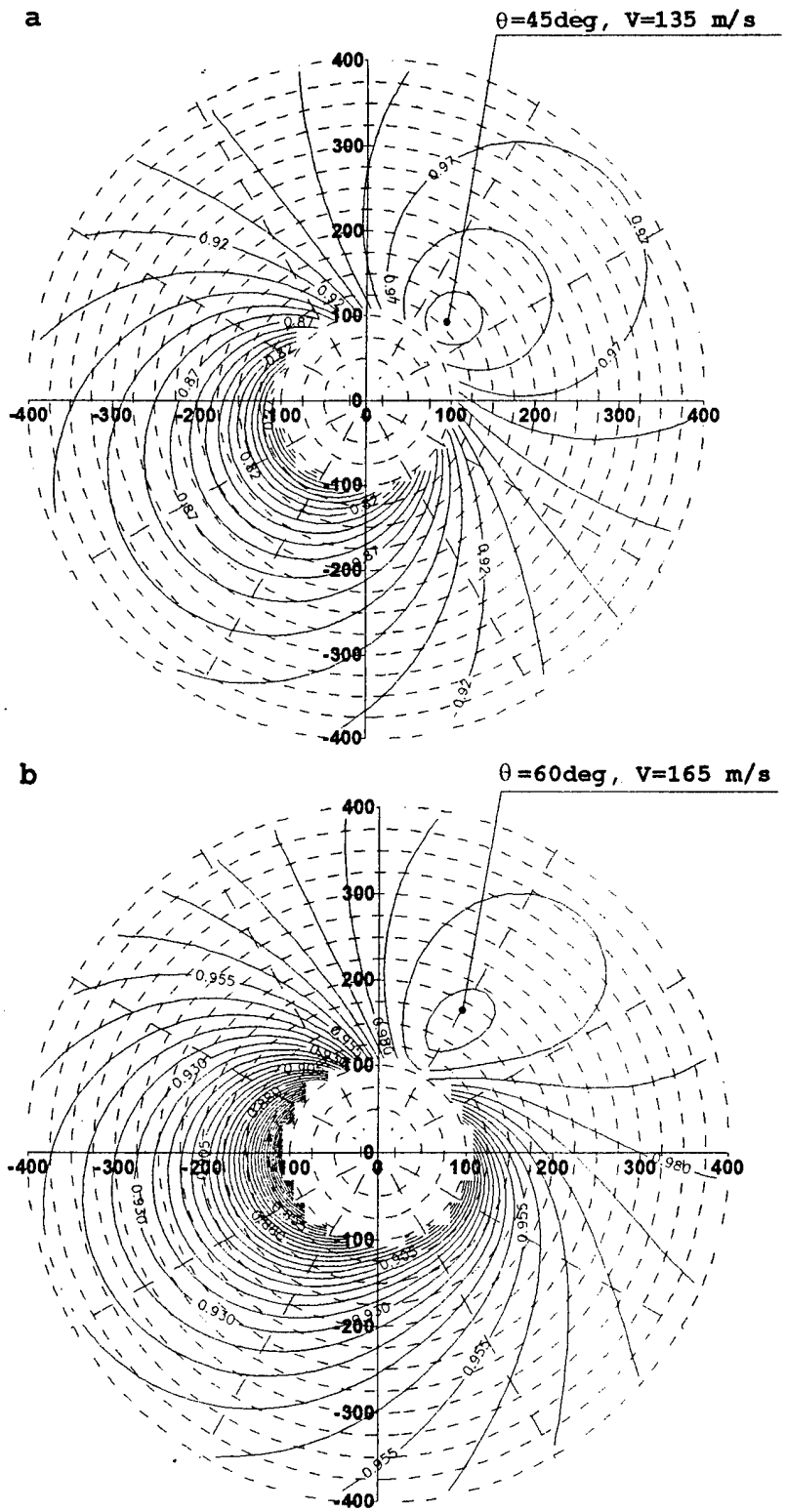

Figure 12: As in Fig. 10, but two long period harmonics ($T = 497.9, 288.3$ min) were removed from time series in each of 12 sectors.

II. IONOSPHERIC OBSERVATIONS

2.1 The BASIS ionosonde and Doppler sounder.

Digital multi-functional ionosonde called BASIS is a basic instrument which is employed for ground - based research and prediction purposes at Institute of Ionosphere. BASIS was also used in the campaign - type research program considered at this report. BASIS is operated as a vertical incidence sounder giving information on the ionospheric parameters. BASIS provided direct information of the ionospheric signal delays (virtual height of radio pulse reflections called ionograms) as a function of frequency. The main parameters of the ionosonde are presented in Table 5

Table 5

SPECIFICATIONS	
Pulse Power	15 kW
Frequency Range	0.3 to 20 MHz
Pulse Coding	Single pulse
Frequency Sweeps	400 frequencies
Height Range	50 to 540 km
Height Resolution	1.5 km

BASIS was designed to record ionograms on film and electrographic paper. Limitations connected with storing, scaling and processing of ionogram records made us to begin designing a computer - controlled system to collect, store, display and scale the ionograms in digital form. A realization of these functions was made on the basis of a " Pentium - 166" computer. The ionosonde and the computer were coupled by a printed circuit board " L - 154". L - 154 passed signals from the receiver and the system of the control to computer in order to collect in for motion and synchronize operations of the ionosonde and the computer. The designed system allows to record an amplitude of reflected signals as well. In order to improve a quality of ionograms the changing threshold of a signal detection was used. Various levels of the threshold allows to operate under different levels of interference from broadcasting. A software package was developed to implement next functions:

a) recording of signal amplitudes in memory of the computer

b) recording of ionograms on the computer screen and in memory of the computer,

c) scaling of the stored data by arrow keys.

" BASIS " sounds 4 times at each frequency . Each of 400 operating frequencies has 4096 levels of an amplitude quantization and 360 levels of effective height quantization. The signal amplitudes at the same frequency are summed. One ionogram with amplitudes of recorded signals requires 288 kB. Each ionogram is stored with header, date and time information.

Scaling of data is carried out by using a semi - automatic method. O and X - components are scaled separately.

Virtual height (h′(t)) temporal variations at fixed frequencies can be obtained from digital ionogram. These variations are used for the estimations of parameters of traveling ionospheric disturbances. To obtain the h′(t) temporal variations digital ionograms were recorded every 5 minutes. Fig. 13 gives an example of h′(t) temporal variations at several fixed frequencies. These variations appear to be caused by the passage of internal atmospheric gravity waves (AGWs) through the ionosphere above the ionosonde. The variations are seen to travel downward indicating well known property of the AGWs vertical phase speed.

Doppler sounder was designed in Institute of Ionosphere to study traveling ionospheric disturbances (Yakovets et al., 1995). The equipment uses two cross - polarized 20 m high delta type antenna for transmission and reception. A frequency synthesizer generates four predetermined frequencies (f_i, i=1...4) which were selected empirically in every observation in order to ensure an approximately equidistant distribution of reflection points below F - layer peak and to avoid interference from broadcasting at HF frequencies.

Reflected from the ionosphere signals at frequencies $f_i + f_{di}$ (where f_{di} is the Doppler shift caused by the motion of the ionospheric screen) were received and Doppler shifts were computed and stored for further processing. During this winter the facility was equipped by two channel transformer set up between the receiver and computer so we could record only two operating frequencies. Fig .14 show Doppler shift variations . There is noticeable difference between h′(t) and Doppler shift variations. The first ones are mostly composed of long period variations which are typical for the TIDs night observations (Yakovets, 1995).

Doppler shift variations are a time derivative of the phase path of radio waves and therefore, Doppler technique enlarges a contribution of high frequency components into TIDs spectra. Simultaneous observations of TIDs by the ionosonde and Doppler sounder showed that the first technique was more informative than the second one.

So the ionosonde was considered to be the main instrument to obtain TIDs parameters and data of the Doppler sounder played an additional role.

2.2. Experimental results

During campaigns conducted from October 1997 till April 1998 the ionosphere was sounded at 5 - min intervals. Altogether, over 5000 ionograms were recorded and analysed. Most of h′(t) records was obtained for extra ordinary component of ionospheric signals.

In order to study a process of TIDs propagation a behaviour of virtual heights (h′(t)) at specific frequencies and the F - region critical frequencies were presented.

He lowest specific (operating) frequency was chosen to be of 2.5 MHz because the real height of its reflection was close to a bottom of the night F2 - region. The adjacent operating frequencies were separated by 0.5 MHz in October, 1997 and by 0.25 MHz in other months.

About 15% of the total number of h′(t) records were rejected from the analysis because of a presence of the E_s - layer which screened the F - region and other reasons.

Fig.15 a shows typical variations of h′(t) on the set of operating frequencies.

In our Figures we use local time which leave behind 75° E solar mean time by 1 hour in the winter time (from October, 27 till March, 28) and 2 hour in the summer (from March, 29). Visual examination of the records allows to do some conclusions. It seems obvious the existence of single the dominant periodicity with a period of ~ 2.2 hours with definite TIDs wave structures. Also it is evident of downward phase propagation of the observed waves especially at high operating frequencies that imply upward propagation of AGWs energy (Hines, 1960). Additionally to a wave process observed at h′(t) variations there is a slow trend which being remained in data can distort a result of a spectral analysis.

It is known that processes in ionospheric plasma and neutral atmosphere drive the height of the F - region (Bousanto, 1990, Miller et. al., 1986).

After sunset median heights increase and continue to be approximately constant during the night. At the end of the night median heights decrease. In addition to the broad night - time plateau in the h′(t) running the morning peak occurs frequently close to the F - region sunrise time. Hajkowicz (1991) proposed to consider this peak as a result of AGWs generation by the supersonic motion of the sunrise terminator.

In sprite of an apparent regular nature of the night h′(t) trend the last demonstrates great variety of its behaviour. Therefore, we could not approximate it by a certain function in order to remove it from original records. A filter of running means was used to remove a trend from the row records. Choosing a length of the running window one has to satisfy to two contradictories. From the one hand cutting of original records because of this filtration should be minimised and from the other hand the length of the running window is recommended to be enlarged to provide the proper filter cut - off. Visual examination all of row h′(t) records obtained

showed that most of period of dominant waves were in the vicinity of 2 hours and this value was chosen to be a length of the running window. The length of the running window is considered to be a filter cut-off period, but data processing showed that the filter cut-off was rather smooth and therefore even when periods of dominant waves exceeded the cut-off period they preserved a significant peak in spectral estimations.

Fig. 15 a shows that an amplitude of h′(t) variations grows with growing of an operating frequency. But it does not mean that an amplitude of electron density fluctuations grows in the same way. The reason of this is following. Commonly the night profile of an electron density is approximated by a parabola with is a good accuracy. That means fast rate of growing of the electron density in the bottom of the F - region and slow rate near the maximum of the F - region. If TIDs propagate through the ionosphere with relative amplitudes $\delta = \frac{\Delta N}{N_0}$ (N_0 - electron density, ΔN - an amplitude of electron density fluctuations) no depending of a height this cause small variations of a real height of a signal reflection in the bottom of the layer and large ones near the maximum of the layer. Those fact that we recorded virtual height variations enhances effect of apparent growing of TIDs amplitude upward. So virtual height variations do not allow to define a TIDs amplitude. For this purpose critical frequency variations were used.

Square of the critical frequency of the ordinary component is proportional to the electron content in the F - layer maximum (Budden, 1961):

$$f_o^2 = kN_{max}$$

The amplitude of electron density variations $\frac{\Delta N}{N}$ (half of the peak-to-peak variations) is found from the amplitude of critical frequency variations as:

$$\frac{\Delta N}{N} = 2\frac{\Delta f}{f_0} \qquad (4)$$

The expression (4) can be used to estimate the relative amplitude of electron content variations in F - layer maximum caused by TIDs. Fig. 15 b shows variations of F - region critical frequencies (f_oF, f_xF) of ordinary and extraordinary components of the ionospheric signal for the same night as in Fig. 15 a. Comparing h′(t) and f_oF, f_xF variations one can see that the last are about in antiphase with h′(t) ones.

This effect is always present in the experimental records. It seems can be explained by a large difference between estimated vertical wavelength (λ_z) and a half thickness of the night F- layer. An average distance between a height of the night F - layer maximum and its bottom does not exceed ~50 km. Taking into account that average $\lambda_z \cong 250$ km (Table 6) one can conclude that the electron density below the

F - layer maximum fluctuates practically synchronously at all heights. That means that, for example, decreasing of the electron density in the F - layer maximum caused by wave propagation accompanies with electron decreasing at all F - layer heights. This decreasing shifts points of a reflection for all operating frequencies upward and, as a result, antiphase variations of $f_{o,x}$ F(t) and h′(t) are observed.

In order to obtain power spectra and phase differences between h′(t) variations occurred at various height the method of Blackman and Tukey (Ienkins and Watts, 1968) has been employed. The Tukey window was used as a lag window. The maximum lag of 120 min has been adopted to obtain a reasonable frequency resolution and accuracy of phase differency estimations. Fig.16 shows power spectra for h′(t) records of operating frequencies f_1 and f_5 shown in Fig. 15a.

The f_1 is the lowest operating frequency and the f_5 is the fifth operating frequency spaced by 16 km from the f_1. Power spectra show a prominent peaks at the frequency F≅ 0.54 cph (cycles per our) and their positions on the frequency axis are very close.

These spectra are typical for h′(t) records obtained. They consist of a single prominent peak corresponding to dominant wave. Small peaks on the lower periods are often present but their values are significantly less.

Not all of h′(t) power spectra demonstrates a coincidence of spectral peaks. Fig.17 shows spectra h′(t) variations at frequencies f_1 and f_5 obtained in December 25, 1987. It is seen that a spectral peak at the lower (f_1) operating frequency is slightly shifted toward a shorter period.

T.Shibata and K. Schlegel (1993) also observed a frequency shift of spectral peaks and gave a reasonable explanation of this fact. TIDs propagate on the background of a neutral horizontal wind which shift an TIDs intrinsic frequency due to a Doppler effect. The Doppler effect of a horizontal wind may be expressed in the following form:

$$F' = F + \frac{1}{2\pi}\vec{k}\cdot\vec{u}(h)$$

Here F' is a TID apparent frequency which is recorded by an observer on the ground, F is a TID intrinsic frequency, $\vec{k}$ is wave number vector and $\vec{u}(h)$ is a horizontal wind velocity vector Assuming that the intrinsic wave parameters, F and $\vec{k}$, are independent of a height, one can conclude that a vertical gradient of the horizontal wind velocity vector causes a height dependence of apparent frequency. It is seen from (4) that a set of F' for series heights gives a possibility to compute a vertical gradient of the horizontal wind if $\vec{k}$ is known. We could not define $\vec{k}$ because we sounded the ionosphere from the single point.

Frequency shifts between positions of spectral peaks have to be accompanied with gradual temporal changing the phase difference between h′(t) variations occurred at different operating frequencies. Fig .18 gives a set of h′(t) variations which spectra are plotted in Fig.17 Visual check confirms this fact. One can see that a phase lag between the same h′(t) signatures at various operating frequencies changes in time. Vary fast changing takes place between the first and second crests of the waves. Next crests reveal more moderate changing in the phase lag. These noticeable fluctuations of phase lag changing are smoothed by a technique of processing which give an average rate of phase lag changing. Temporal fluctuations of phase lag changing may be caused by fluctuations of a vertical gradient of the horizontal wind.

From the study of data obtained it is clear that TIDs are practically always present in the night ionosphere. Now we will classify TIDs according to their behavior during the period of observations. The first type presents TIDs existing during all night with approximately constant amplitude and period (Fig. 13, 15a).In these figures gaps in the run of the top operating frequencies correspond to periods when the critical frequency becomes below the operating frequency.

The second type presents TIDs with large amplitudes in the beginning of records and their further gradual attenuation (Fig. 19,20). These two types of h'(t) variations are the most frequently met in the analyzed observations. This types appear to be understood on the basis of packet-like TIDs structure considered in section 2.3.

Kaliev et al. (1989) analyzing packet with the periods of oscillations of 7-60 min. found a correlation between a period of oscillations and a duration of a packet. Long period packets could last as long as 6 hours. Hence, a duration of packets with a period of oscillations of two hours may reach a significant value exceeding a course of observations. We can think that nights with the constant amplitude of h'(t) variations correspond to a middle fraction of a wave packet. The second type of the amplitude variations behavior may present the end of current packet.

Fig.21 shows small variations of h'(t) during the night and large surge in the premorning hours. This surge seems to be caused by the solar terminator generating AGW near sunrise on the height of the F-region.

In order to summarize TIDs characteristics measured during the period of observations a table 6 was made.

Table 6.

Date	Period (min)	$\delta=\Delta N/N$ (percent)	V_z (m/sec)	λ_z (km)	Freq. shift	K_p– index
1	2	3	4	5	6	7
1.10.97	96	7	40	230	no	36(D)
2.10.97	Uncert.	Uncert.				10
4.10.97	120	Uncert.	49	352	no	8(Q)
7.10.97	180	10	23	248	-	17
12.10.97	78	3	53	248	+	11
27.10.97	140	6	31	260	+	25(D)
30.10.97	108	7	48	300	no	14
1.11.97	84	8	66	332	no	16
3.11.97	96	10	91	520	no	7
25.11.97	66	6	28	110	-	4(Q)
27.11.97	96	4	12	69	+	3(Q)
29.11.97	144	Uncert.	26	250	no	1(Q)
30.11.97	108	Uncert.			no	12
5.12.97	138	7	42	347	no	16
6.12.97	96	6	52	299	no	8
8.12.97	108	Uncert.	43	278	no	1(Q)
24.12.97	150	15	18	162	no	8
25.12.97	96	12	59	340	+	2(Q)
30.12.97	90	8	46	248	no	26(D)
31.12.97	180	8	34	208	+	6
5.01.98	108	15			no	6(Q)
23.01.98	102	12	40	368	no	7(Q)
29.01.98	126	5	17	122	+	15
30.01.98	108	10	28	171	no	26(D)
2.02.98	111	14	48	319	no	5(Q)
24.02.98	120	Uncert.	45	324	+	6(Q)
25.02.98	210	5	55	693	+	6(Q)
27.02.98	108	Uncert.			no	10
28.02.98	102	7	36	259	no	21(D)
2.03.98	90	4	23	124	no	25
23.03.98	130	6	41	344	+	10
24.03.98	120	Uncert.	50	360	no	13
29.03.98	96	5			no	26
30.03.98	132	5			+	16
2.04.98	108	7			-	

The first column contents dates of observations analyzed. The second one gives a period of a dominant wave observed in the certain night. The sign ''uncert.'' Denotes uncertain data. Relative amplitudes computed from formula (4) are listed at the third column. Here, the sign ''uncert.'' Corresponds to events when wave oscillations occurred on the level or below of a noise amplitude which average value was estimated to be of 2 %. The fourth column contents vertical phase speeds estimated from a difference of real heights of ionospheric signal reflections and lags obtained from cross-correlation analysis. For seven nights speeds could not be estimated because very low time delays. Four of these events corresponded to low wave amplitude may be caused by errors of statistical processing. But three events (29.03.98, 30.03.98, 2.04.98) for wave amplitudes exceeding noise levels. Here, low lags could be explained on the basis of Perkins (1973) instability. Perkins instability develops in the night F-region and force the ionosphere to move up and down as whole.. So the vertical phase speed estimated from record obtained for different operating frequencies would be uncertainly large.. Kelley and Fukao (1991) proposed that gravity waves in the certain conditions can initiate the Perkins instability.

Next column gives values of the vertical wavelength estimated from the product of a period by V_z.

The column with a frequency shift gives a difference between the spectral peaks at operating frequencies f_1 and f_5. The positive sign corresponds to an event when a spectral peak at the lower (f_1) operating frequency is shifted toward a shorter period. The negative sign corresponds to the opposite direction of a frequency shift. And sign ''no'' corresponds to events when no shifts were observed.

In the last column K_p-indices of geomagnetic activity are listed.

Parameters from the Table 6 are presented by distributions in the Fig.22. Plots show that the main part of parameters analyzed is distributed in relatively narrow ranges. Fig. 23 presents a relative amplitude of TIDs (8) versus K_p-index. There is not evident correlation between these values, but one can see that under high geomagnetic activity wave amplitudes noticeably exceeded the noise level. This confirm results of TIDs observations after great geomagnetic storm (Hajkowicz,1987, 1991, Yeh et al., 1994). At the same time for nights with low geomagnetic activity wave amplitudes are distributed in the rather wide range. Large amplitudes for the low K_p-indices prove that there are sources of TIDs activity not connected with auroral regions.

Fig. 23b presents a seasonal dependence of an average relative amplitude. It grows noticeable in the winter months.

To compare the results of measurements in the ionosphere and mesosphere three days were chosen with wave motions well developed into both regions. Detrending applied for processing of optical data was used for analysis of the ionospheric data. This procedure allowed to reveal the low frequency components eliminated by cut-off high frequency filtering. Fig. 24, 25, 26 give detrended relative virtual height variations at frequencies f1, f5 and their normalized power spectra for Nov. 27, 1997, Feb. 2, 1998 and March 23, 1998. Here, a solid line corresponds to f1 and a dashed line – to f5. Temporal variations of relative emission rate temperature and their spectra are plotted in Fig. 2, 6, 8. Comparing ionospheric and mesospheric wave variations one can found their similarity and this fact is supported by their spectra except the spectra for Nov. 27, 1997. The optical spectra show the very large peaks at period of 500 min., but the ionospheric spectra have no the similar peaks. This fact is explained by different lengths of optical and ionospheric data. The length of optical data equaled to 12 hours allows to resolve the 500 min component. Meanwhile the length of ionospheric data for this date is equal to 8 hours, therefore the 500 min component was considered as trend and was eliminated from row data. In order to equalize the pre-processing procedure the same detrending was applied to optical data and corresponding data are plotted in Fig.27. Periods of prominent spectral peaks for virtual height (h'f5, h'f1) and emission rate (E) variations plotted in Fig. 24-27 are listed in Table 7.

Table 7

	Nov.27, 97		Feb. 2, 98		March 23, 98	
	T1(min)	T2(min)	T1(min)	T2(min)	T1(min)	T2(min)
h'f5	143	300	110	195	130	310
h'f1	135	265	110	195	120	360
E	160	300	100	150	140	300

One can see that there is no the complete coincidence for periods of spectral peaks corresponding to different heights of observations except ionospheric data for Feb. 2, 1988. We suppose that this difference is caused by a vertical gradient of the background neutral wind, which shifts the intrinsic frequency for different heights on a different value.

The comparison of optical and ionospheric data proves simultaneous existence of wave variations with close periods at mesospheric and ionospheric heights. The direction of the vertical phase speed of a wave motion with a middle period of 2 hours at ionospheric heights (the average real height of ionospheric observations was equal to 250 km) showed that these are travelling ionospheric disturbances caused by AGW's. It is of great interest for determine a nature of ionospheric and meso-

spheric variations with periods of ~ 300 min whether they belong to AGW's of tidal waves.

Conclusions.

Observations of travelling ionospheric disturbances during the period from October 1997 till March 1998 showed that TIDs with periods of 80-180 min are common feature of the night ionosphere. Various parameters of TIDs including periods, relative amplitudes, vertical phase speeds, vertical wavelengths were measured and their distributions were constructed. A frequency shift between TID spectral peaks belonging to different heights was found for a part of observations and its possible reason was discussed. A seasonal dependence of TIDs average relative amplitudes for six months was plotted. Evident correlation between TID relative amplitudes and Kp-index was not found. A comparison ionospheric and mesospheric data showed that waves with nearby frequencies exist simultaneously in the both regions.

Several reasons make us to proceed ionospheric and mesospheric observations till October 1988 to complete a year cycle. We hope to obtain a seasonal dependence of various waves parameters. Besides, summer time is favorable for studying travelling planetary waves in the mesopause region, and we are going to perform regular optical measurements this summer if even the period of observations during the night will be short.

Our measurements will be supported by the optical measurements at other sites (Canada, Spain, Japan) and we will have a good possibility for analysis of planetary waves. Moreover, several tasks connected with computations have to be done. It is necessary to compute the vertical phase speed of low frequency wave components (T ~ 300 min.) and define their nature. Calculations of the wave horizontal velocity on the basis of optical data have to be done and vertical gradient of the neutral wind will be obtained.

If the night TIDs spectra reveal a prominent peaks corresponded to dominant waves then day-time spectra seem to be broad and extended toward high frequencies. This fact gives a possibility to study a fine structure of TIDs and relationships between different parts of the spectra. The results of this study will be present in sections 2.3,

2.3. A STUDY OF WAVE PACKETS IN TRAVELLING IONOSPHERIC DISTERBACES

HINES (1960) was the first who suggested that internal atmospheric gravity waves (AGWs) propagating in the neutral thermospheric gas caused travelling ionospheric disturbances (TIDs). Many radio techniques including ground-based and satellite ones were employed to observe TIDs during day- and night-time in the different seasons and under various geomagnetic and solar conditions.

There were at least two approaches to an interpretation of TIDs observations. According the first one, only TIDs visually identified with monochromatic individual AGWs were taken into consideration in order to estimate their parameters (DAVIES and JONES, 1971; WALDOCK and JONES, 1987). This approach gave an opportunity to obtain TIDs characteristics from a small fraction of experimental data. For example, JACOBSON and CARLOS (1991) could find only a few monochromatic TIDs from their database which exceeded 100 hours of observations.

According the second approach, TIDs are considered to be a stationary field with certain spatial and temporal spectra. In order to estimate TIDs parameters at all frequencies of spectra the cross-spectral analysis was employed (HERRON, 1973; TSUTSUI *et al.*, 1984; SHIBATA and OKUZAVA, 1983, YAKOVETS *et al.*, 1995). This technique allowed to utilise practically all Doppler and other continuous TIDs records but was not able to separate monochromatic individual TIDs and background ones which were considered to be a result of a multiple-wave overlap that distort the spatial and temporal coherence (JACOBSON and CARLOS,1991).

Passing TIDs records through pass-band filters, BEGGS and BUTCHER (1989) and KALIEV *et al.* (1989) have found that some frequency ranges had temporal sections which comprised packet-like structures with amplitudes of oscillations that appreciably exceeded the amplitudes of background oscillations. JACOBSON et al. (1995) offered to use temporal sections with large amplitudes to estimate the wave parameters because they are thought to be caused by individual TIDs, while the background oscillations were a result of a multiple TIDs superposition. They looked the records of radio signals from geosynchronous satellite beacons through time- and frequency-windows in order to select dominated single-wave individual TIDs and define azimuths of their propagation.

It should be pointed out that the time- and frequency-window procedure allows to find not only parameters of individual TIDs, but parameters of multiple TIDs superposition as well. A comparison of parameters of individual and multiple TIDs is of great interest because it gives a tool to inspect previous measurements interpreted in the framework of a model of stationary TIDs.

This paper presents results of this comparison. The technique of a computation of the cross-correlation coefficient for individual TIDs existing on the background of a multiple TIDs superposition was developed. This technique was employed to TIDs observations obtained by the multifrequency HF Doppler sounder. Besides the vertical phase speed for individual TIDs was estimated in comparison with the speed of the TIDs superposition and a behaviour of a current phase was studied.

Observations of TIDs at several heights of the F-layer ionosphere were carried out at the Alma-Ata multifrequency HF Doppler sounder (76°55′E, 43°15′N). The sounder operated at five sounding frequencies which were selected for every observation to ensure an approximately equidistant vertical distribution of reflection

points below the F-layer peak. The details of the equipment have been described in our previous paper (YAKOVETS *at al.*, 1995). Fig.2 of this paper shows typical records of the Doppler variations ($f_d(t)$) at four operating frequencies. In order to obtain the power spectra the method of Blackman and Tukey (JENKINS and WATTS, 1968) has been employed. The Tukey window was used as a lag window. The maximum lag of 60 min has been adopted to obtain a reasonable frequency resolution. Figure 3a (YAKOVETS *at al.*, 1995) shows normalised power spectra for the records of Doppler variations presented in Fig. 2a. Careful inspection of the normalised power spectra shows that typical spectra often comprised several spectral peaks on the background of continuous spectra.

In order to study the temporal behaviour of spectral contributions whose amplitudes exceeded the background ones, the complex demodulation method (MARPLE, 1988) was employed . This method operates as a band-pass filter giving an opportunity to obtain both a filtered signal and a current phase of this signal on its output. The current phase is present a difference between a phase of the filtered signal and a reference signal with a fixed frequency equalled to the central frequency of the filter. The filter band-width of 1 cph (cycle per hour) was chosen to be close to spectral resolution of the method of Blackman and Tukey used at the preliminary stage of processing and to ensure a good reconstruction of wave packets whose presence into original records was not usually apparent to the eye especially in the high frequency TIDs range. Figure 28 is the result of filtering of Doppler shift variations at five operating frequencies for the day of 17 March 1988. One can make the certain conclusions about a temporal behaviour of filtered records.

In the first time interval (t = 09.00 ÷ 12.20 LT) of plotting $f_d(t)$ variations there is a narrow band quasi-stochastic process and in the second time interval (t = 12.20 ÷ 14.20 LT) $f_d(t)$ oscillations have the appearance of a wave packet. By using this technique of processing we found that packet-like structure in $f_d(t)$ variations appeared to be common. It is therefore important to compare features of these two types of TIDs separately. A term ,''quasi-stochastic TIDs'', is used instead of ''a multiple TIDs superposition'' to reflect a random character of a behaviour of an amplitude and phase of the wave resulted from the multiple TIDs superposition.

The cross-correlation functions ($R(\tau)$) between filtered records of $f_d(t)$ were computed for quasi-stochastic parts of the records and for packet-like structures separately. Fig. 29 presents cross-correlation functions $\left(R_{n_1,n_2}(\tau)\right)$ for the first, quasi- stochastic parts of records plotted in Fig. 28. Fig. 30 presents cross-correlation functions $\left(R_{x_1,x_2}(\tau)\right)$ for the second, packed-like parts of the same records. From these figures it can be seen that values of peaks of $R_{x_1,x_2}(\tau)$ exceed those of the correspondent peaks of $R_{n_1,n_2}(\tau)$. Besides lags of $R_{x_1,x_2}(\tau)$ peaks rela-

tive to $\tau = 0$ exceed lags of correspondent $R_{n_1,n_2}(\tau)$ peaks. That means that a vertical phase velocity of packets is less than a velocity of quasi-stochastic TIDs.

Values of the vertical phase velocity were computed from the measured heights of radiowaves reflection points and lags of correspondent $R(\tau)$ peaks. The true heights of the reflection points for each observation were computed by using ionograms of the Alma-Ata ionospheric station. All registrated waves had a downward phase motion, and their velocities grew with growing of a height of the radio wave reflection. In Table 8 average velocities computed from records corresponding to maximum and minimum heights for dates indicated are listed.

One can see that for all considered records the vertical phase velocity of quasi-stochastic TIDs markedly exceeded of the velocity of packets. Table 8 contents velocities for both packets and quasi-stochastic parts only for long-period TIDs. The reason of this will be discussed later.

The value of the cross-correlation function peak is the cross-correlation coefficient. It gives a measure of the coherence between records corresponding to different ionospheric heights. It is clear that the cross-correlation coefficient computed for time intervals characterising by a packet-like structure depends not only on the degree of the coherence of wave packets but and a ratio of amplitudes of packets and quasi-stochastic TIDs.

Indeed, caused by numerous sources the quasi-stochastic TIDs field insures continuous variations of measured $f_d(t)$ at any time and place of observations, thus wave packets appear only on the background of quasi-stochastic variations. In order to obtain the cross-correlation coefficient R_{S_1,S_2} for the "pure" wave packets, the method of the definition of R_{S_1,S_2} was developed (Appendix). By using this method R_{S_1,S_2} were estimated and listed in Table 8. One can see that the less correlated quasi-stochastic TIDs behave as an unwanted noise which cause a drop of the resultant cross-correlation coefficient $\left(R_{x_1,x_2}(\tau)\right)$. The results presented may be divided into two groups. For the first group comprising long period TIDs the values of R_{x_1,x_2} and R_{n_1,n_2} are sufficiently large, and R_{S_1,S_2} exceeds them insignificantly. The different situation one finds for the second group comprising short period TIDs (T $\leq$ 20 min). Drastic increasing of R_{S_1,S_2} relative to R_{x_1,x_2} and especially R_{n_1,n_2} occurred. That means that quasi- stochastic TIDs mask the fact that even high frequency TIDs packets propagate practically without changing their form along the large distance on the vertical plane.

We could not obtain accurate values of the vertical velocities for the TIDs period less then 20 minutes from cross-correlation functions because of small lags of their maximums relative to 0 which were of the order of the sample interval of 1 min. In order to estimate vertical phase speeds, current phases were computed by the complex demodulation method. An example of filtering data obtained on 14 Feb.

1990 is plotted in Fig. 31a. The current phase of figured data are plotted in 27b. The current phases corresponding to adjacent heights are spaced 2 π apart to avoid a mishmash of their runs.

Comparing Fig. 31a, 31b one can see two successive wave packets on temporal intervals 12.20 ÷ 13.40 and 13.50 ÷ 14.50. There is a significant difference between a phase behaviour inside and outside wave packets. If a current phase inside wave packets keeps a stable position with small fluctuation, then outside the phases fluctuate with a large amplitudes and independently for different sounding frequencies. Small fluctuations inside the wave packets appear to be caused by the additional quasi-stochastic oscillations. Sometimes a gradual run of the current phase is distorted by its fast jumps. Two types of the phase jumps were found. The first one is characterised by jumps which are less of 2π, and their nature will be discussed further. The second one is characterised by jumps equalled to 2π, and they originate from the phase uncertainty of 2π. A number of these jumps can be decreased by certain changing of the initial phase of the records to shift the most probable phase in the filtered record in the vicinity of π, but it is difficult to eliminate the jumps completely because of large phase fluctuations into quasi-stochastic parts of the records.

After averaging the current phase inside packets, one can find an average phase difference between various heights, and estimate the vertical phase velocity. This procedure can not be applied to temporal intervals with quasi-stochastic TIDs because of large uncorrelated phase fluctuations during interval 09.00 ÷ 12.20 and 14.50 ÷ 16.30. Therefore for TIDs within period less than 20 min the vertical phase velocity was estimated only for the wave packets.

Fig. 32a,b show filtered records and current phases at the frequency of 3 cph on 14 February 1990. Data presented in Fig. 32 are obtained from the same records as in Fig. 31. However, their character is markedly different. Practically the whole length of records is occupied with three distinct wave packets. Looking at the slope of the current phase, one can make several conclusions:

a) the frequencies of oscillations in all packets are slightly different from the central frequency of the filter. It can be seen from the behaviour of the derivative of the phase with respect to time that defines a difference between the central frequency of the filter and a frequency of the filtered signal;
b) the frequency of oscillations of the second and third packets are equal; moreover they are coherent because their frequencies are stable in the course of a packets existence;
c) clear discontinuities occur between the second and the third packets, and a value of the phase jump grows with the height of reflection of radio-signals;
d) the frequency of oscillations of the first packet does not coincide with the frequency of oscillations of the second packet;

e) phase differences between packets corresponded to different heights are reasonably constant except frequency f_1 , where relatively small packet amplitude is distorted by an additional noise.

Table 8

N	Date	T(min)	V(ms^{-1})		Cross- correl. coefficient			
			packet	stoch. field	R_{x_1,x_2}	R_{s_1,s_2}	R_{n_1,n_2}	Δh km.
1.	17.03.88	40	100	195	0.94	0.98	0.83	35
2.	08.02.90	30	175	220	0.95	0.99	0.85	55
3.	14.02.90	50	165	390	0.87	0.96	0.70	70
4.	19.11.90	40	105	165	0.99	0.99	0.82	50
5.	24.02.90	18	470		0.80	0.99	0.4	45
6.	19.11.90	13	350		0.85	0.98	0.6	50
7.	17.03.88	7	580		0.78	0.83	0.7	35
8.	14.02.90	12	500		0.8	0.98	0.4	70
9.	08.02.90	11	660		0.6	0.78	0.35	55
10.	15.02.90	20	650		0.78	0.99	0.4	60

The properties of the individual wave packet phase structure are important because they may help to realise both the wave generation mechanisms and conditions of the wave propagation. We studied 28 series of filtered daytime records comprising 49 series of wave packets. Every series of the filtered records consisted of 4–5 records corresponding to different operating radio frequencies . The average length of the records was 5–6 hours. Under the series of wave packets we meant a wave packet observed at all heights simultaneously.

Most wave packets had a constant period of oscillations, and only five packet series showed a growing period with time as FRANCIS (1974) has predicted for waves originated in the auroral electrojet. No packets were registered with the period of oscillations decreasing with time. These results are consistent with observations of BEGGS and BUTCHER (1989).

Relatively small number of analysed packets did not permit to estimate some temporal statistic parameters for various ranges of periods of oscillations. So we had to do it for a total range of periods from T= 7 min to T= 50 min. The average duration of wave packets was 90 min with average number of oscillations of five. The maximum duration of wave packets was observed to be 250 min for a wave period

of 50 min and 180 min for the wave period of 20 min. The minimum duration of wave packets was observed to be 50 min.

The frequency - window procedure was applied to observations of midlatitude TIDs at several heights. This procedure gave an opportunity to reveal some new properties of TIDs. Generally, TIDs are composed of temporal intervals with quasi-stochastic oscillations of the electron density and intervals having packet-like structures with quasi-monochromatic oscillations. Computing cross-correlation coefficients for both types of TIDs and applying method developed at Appendix, we found the coherence to be close to 1 even for high frequencies TIDs progressed in the vertical plane up to distance 80 km. At first sight it is not consistent with YAKOVETS' et al. (1995) measurements in which the fast drop of the coherence of the high frequency component TIDs was proved. In fact, there is not a contradiction. The results of the previous paper were obtained by processing the whole records which lasted 6-8 hours and comprised both quasi-stochastic and packet-like TIDs. Values of the coherence depended on a contribution of wave packets in the total TIDs field — a ratio of amplitudes of packets to those of quasi-stochastic fluctuations and a ratio of their lengths. As a result the ''average'' coherence was estimated.

In order to explain a difference between vertical phase velocities of the wave packets and quasi-stochastic TIDs, one has to apply to the full correlation analysis (FCA) method developed to obtain parameters of turbulence from records registered by spaced receivers (BRIGGS et al. ,1950). Authors have shown that the apparent velocity computed from a lag of the cross-correlation function for records of spaced receivers exceeded the true drift velocity of turbulent structures. A number of papers were devoted to this phenomenon, but it is beyond the scope of this paper. Recent works of DEWAN (1985,1991) have developed the gravity wave power spectra model based on the turbulent-like wave field picture. This model seems to be present quasi - stochastic TIDs resulted from the multiple-waves superposition. A similitude of descriptions of turbulence and the quasi-stochastic TIDs field permits the FCA method to be used for processing of TIDs records. Although there is no full understanding of how TIDs parameters can be related with results of an application of the FCA method, a difference between vertical velocities of wave packets and quasi- stochastic TIDs appears to be explained by some peculiarities of the FCA method mentioned above.

There are two theoretical models of a behaviour of an oscillation period inside a wave packet. FRANCIS (1974), considering the auroral electrojet as a source of TIDs, has shown that after travelling through the atmosphere up to F region the earth-reflected waves gain the appearance of a wave packet. The oscillation frequency inside the packet decreases with time, approaching to an asymptotic value.

The asymptotic and average frequencies of a wave packet decrease linearly with growing of a distance between a source of TIDs and a point of observations.

An analysis of the correlation between magnetic activity and five occurrences of packets observed at Alma-Ata with the growing periods of oscillations did not show evident exceeding of Kp-index for these days compared with days when a period of oscillations inside wave packets was constant.

Sources located in the troposphere would generate direct and earth-reflected waves which, superimposing, would give a single wave packet in the F region. On the basis on the HINES' dispersion relation (1960), WALDOCK and JONES (1987) have suggested that TIDs associated with the tropospheric jet stream appear in the F region as a wave packet with quasi-monochromatic oscillations whose period is a function of the elevation angle of the wave ray path from the source to the point of observations in the F region. Absence of meteorological data did not allow us to compare them with TIDs activity. However, as BEGGS and BUTCHER (1989) pointed out that even with data available it was not possible to prove a relationship between the tropospheric jet stream and the occurrence of TIDs "since TIDs represent an imperfect tracer of the passage of gravity waves in the thermosphere".

One of the reason of phase jumps have been discussed by WATERS et al. (1991). They studied Pc 3–4 geomagnetic pulsations which were often observed as separate wave packets. Numerous records have shown that jumps of the current phase occur between close successive packets. An analysis of simulated pulsations showed that phase jumps can be explained in terms of phase variations of a resultant wave formed by superposition of two adjacent wave packets having nearby frequencies of oscillations. A value of the phase jump depends on the ratio of amplitudes of the packets superimposed. The smaller a difference of their amplitudes, the larger the value of the phase jump. If the envelopes of interfering packets have equal amplitudes, then a 180° jump occurs in the resultant wave packet. At this moment the minimum amplitude of the resultant packet occurs.

Different phase jumps observed at different heights at one series (Fig. 32 b) seem to be caused by the different ratio of amplitudes of interfering packets. The more value of the phase jump took place, the less amplitude corresponded to this moment occurred. Therefore phase jumps observed may be explained as a result of the superposition of two wave packets with nearby frequencies of oscillations. All these packets were quasi-monochromatic and hence can be associated with the tropospheric jet streams.

FRANCIS (1974) has predicted direct and earth-reflected waves from tropospheric sources. In order to explain beating of these waves, one have to suggest the motion of the jet stream which would provide a different Doppler shift for the both waves. It does not seem to be possible if the earth is plane in the vicinity of a region of the wave generation because the direct and earth-reflected waves would travel at the same angle with respect to the horizontal plane to superimpose in the F re-

gion. However, a proximity of Almaty to the large mountain region may change a condition of equality of angles and so lead to different Doppler shifts.

Different values of phase jumps changed phase lags between adjacent heights, but it took place only in short intervals of the order of a wave period after which the phase lags became the same as in the previous packets. Therefore, vertical phase velocities have to be measured in the temporal intervals with large amplitudes to obtain reliable results. It is consistent with criteria used by JACOBSON et al. (1995) in their experiment.

Travelling ionospheric disturbances observed over Almaty by the multifrequency Doppler sounder in 1988–1990 have been analysed by using complex demodulation method. The various properties of two types of TIDs called quasi-stochastic and wave packets were studied. A method of a calculation of the cross-correlation coefficient for the wave packets propagating on the background of quasi-stochastic TIDs was developed. The high coherence in the vertical plane for ''pure'' wave packets was found. Most wave packets had quasi-monochromatic structure explained on the basis of the wave propagation from the sources of TIDs located in the troposphere . A small number of wave packets had oscillations with a period increased with time. This behaviour followed the FRANCIS' (1974) prediction for earth-reflected medium gravity waves generated in the auroral region.

APPENDIX

Let us denote by $S_1(t)$ oscillations of the Doppler shift caused by coherent fluctuations of the electron density and by $n(t)$ oscillations caused by quasi-stochastic fluctuations of the electron density. A symbol 1 will define the fluctuations for the height h_1 and a symbol 2 will be used for the height h_2. Evidently that quasi-stochastic fluctuations caused by numerous sources of AGWs exist continuously, so when coherent packets are observed the total values of the Doppler shift will be the sum of the coherent and quasi-stochastic fluctuations:

$$x_1(t) = S_1(t) + n_1(t) \quad \text{and}$$
$$x_2(t) = S_2(t) + n_2(t)$$

for the heights h_1 and h_2 , respectively.

Mean values $\overline{x(t)}$, $\overline{S(t)}$, and $\overline{n(t)}$ equal to 0 because of preliminary band-pass filtering of original Doppler records and thus the cross-correlation function may be written, as:

$$R_{x_1x_2}(\tau) = \frac{\overline{[S_1(t) + n_1(t)][S_2(t+\tau) + n_2(t+\tau)]}}{\sigma_{x_1} \cdot \sigma_{x_2}}, \qquad (5)$$

where overscored bar shows the mean of the product and σ_x^2, σ_S^2 and σ_n^2 are dispersions of respective values.

Assume that maximum $R_{x_1x_2}(\tau)$ is centered at $\tau = 0$, and further we will write $R_{x_1x_2}$ instead $R_{x_1x_2}(0)$. Processes $S(t)$ and $n(t)$ are independent and so $\overline{S_1(t)n_2(t)} = \overline{S_2(t)n_1(t)} = 0$. Hence

$$R_{x_1x_2} = \frac{\overline{S_1(t)\cdot S_2(t)} + \overline{n_1(t)\cdot n_2(t)}}{\sigma_{x_1}\cdot\sigma_{x_2}} \tag{6}$$

Denote a ratio of the power of the coherent part of oscillations to the power of the noise as

$$q^2 = \frac{\sigma_S^2}{\sigma_n^2}$$

and coefficient of correlation as

$$R_{S_1S_2} = \frac{\overline{S_1(t)\cdot S_2(t)}}{\sigma_{S_1}\sigma_{S_2}} \text{ and}$$

$$R_{n_1n_2} = \frac{\overline{n_1(t)\cdot n_2(t)}}{\sigma_{n_1}\sigma_{n_2}}$$

Taking into account that

$$\sigma_x^2 = \sigma_S^2 + \sigma_n^2, \tag{7}$$

we obtain

$$R_{x_1x_2} = R_{S_1S_2}\frac{q_1q_2}{\sqrt{1+q_1^2}\sqrt{1+q_2^2}} + R_{n_1n_2}\frac{1}{\sqrt{1+q_1^2}\sqrt{1+q_2^2}} \tag{8}$$

Here all values except $R_{S_1S_2}$ are determined from the experimental records.

Note that filtered Doppler records content quasi-stochastic temporal parts which give an opportunity to obtain $R_{n_1n_2}$, $\sigma_{n_1}^2$ and $\sigma_{n_2}^2$ and temporal parts with wave packets which allow to estimate $R_{x_1x_2}$, $\sigma_{x_1}^2$ and $\sigma_{x_2}^2$. Assuming that quasi-stochastic Doppler fluctuations are stationary process, one can think that values of parameters obtained from quasi-stochastic temporal parts of records are valid for temporal parts comprising wave packets in order to compute σ_S^2 and $R_{S_1S_2}$ by using (7) and (8) respectively.

2.4 NONLINEAR WAVE - WAVE INTERACTIONS OF TRAVELLING IONOSPHERIC DISTURBENCES

Acoustic gravity waves (AGWs) propagating in the neutral atmosphere are manifistated in the ionosphere as traveling ionospheric disturbances (TIDs). It was shown (Kaliev et al., 1988) that TIDs spectra are composed of a series of spectral peaks existing on the background of continuous spectra whose density degreases toward the high frequencies edge of a spectral band. The line typed TIDs spectra give a possibility to carry out experimental studying of wave - wave interactions.

It is known (Turner, 1973) that nonlinear resonant interaction among three dispersive waves can occur when the conditions of $\vec{k}_1 + \vec{k}_2 = \vec{k}_3$ and $\omega_1(\vec{k}_1) + \omega_2(\vec{k}_2) = \omega_3(\vec{k}_3)$ are satisfied. The new wave with frequency $\omega_3(\vec{k}_3)$ originated into wave - wave interaction grows linearly. Extensive theoretical investigations of the interactions were carry out for waves in the ocean (Miller et al. 1986) and the atmosphere (Dong and Yeh, 1988). However, small experimental studies were made for TIDs propagating in the ionosphere. Ma and Schlegel (1993), analyzing data obtained by the EISCAT facility, found that nonlinear wave - wave interactions took place for TIDs spectral components in the auroral F - region.

This conclusion was made on the basis of an analysis of a single TIDs record. Therefore, to enhance a statistical reliability of this conclusion additional studying is required.

The purpose of this section is to study nonlinear wave - wave interactions of mid - latitude TIDs and to compare them with results obtained by Ma and Schlegel (1993).

Here we describe briefly bispectral analysis imployed to estimate a fact of nonlinear interactions. Suppose x(t), t = 1, 2 ....N, is a series of experimental data. The series is subdivided into p segments each of length M. The complex spectrum of the j-group:

$$X_j(\omega) = \sum_{t=1}^{M} x_j(t) \cdot W_j(t) e^{-i\omega t}, \tag{9}$$

where $W_j(t)$ - is a " time window " weighting function used for improving of reliability of spectral estimates. After that complex spectra are summed to obtain the spectral average estimate:

$$S(\omega) = \frac{1}{p} \sum_{j=1}^{p} X_j(\omega) \cdot X_j^*(\omega), \tag{10}$$

where the asterisk denotes the complex conjugate.

The segments may be overlapped or disjoint. If disjoint segments are used a noticeable fraction of the series will be lost because weighted x(t) are close to zero near the edges of segments. So segments overlapping has to be used to enlarge the percentage of the series being involved into the S(ω) estimates.

The estimate of the bispectrum is given as (Nikias and Raghuveer, 1987)

$$B(\omega_1,\omega_2) = \frac{1}{p}\sum_{j=1}^{p} X_j(\omega_1)\cdot X_j(\omega_2)\cdot X_j^*(\omega_1+\omega_2),$$

The bispectrum gives a measure of the multiplicative interaction of the three frequency component of the x(t) spectrum. The normalized bispectrum is the bicoherence:

$$b^2(\omega_1,\omega_2) = \frac{|B(\omega_1,\omega_2)|^2}{\frac{1}{p}\sum_{j=1}^{p}\left|X_j(\omega_1)\cdot X_j(\omega_2)\right|\frac{1}{p}\sum_{j=1}^{p}\left|X_j(\omega_1+\omega_2)\right|^2} \tag{11}$$

If the component at $f_3 = f_1 + f_2$ is generated by nonlinear interaction and additional unwanted noise is significantly less of the interactive components then the bicoherence is close to 1. The necessary condition for $b^2(\omega_1,\omega_2)$ to be close to 1 is $\Psi_3=\Psi_1+\Psi_2$, where Ψ_i - is a phase of the correspondent frequency. We realized a program of bispectral analysis at PC " Pentium". In order to check up its running an artificial time series was generated as:

$$x(t) = \cos(2\pi f_1 + \Psi_1) + \cos(2\pi f_2 + \Psi_2) + \cos(2\pi f_3 + \Psi_3) + n(t), \tag{12}$$

with frequencies chosen nearby real frequencies of Doppler shift fluctuations: f_1=0.025 min^{-1}, f_2=0.043 min^{-1} and f_3=0.068 min^{-1}. The initial phases were satisfied to $\Psi_3=\Psi_1+\Psi_2$. n(t) - is an additive white noise.

The series consisted of 600 data points at 1 - min intervals, giving a total record length of 10 hour. The Hemming window were used:

$$W(t) = 0.54 + 0.46\cdot\cos(\frac{2\pi}{M}\tau), \tau = -\frac{M}{2}\ldots -1,0,1\ldots\frac{M}{2}$$

To provide a good spectral resolution the window width was chosen to be M=120. Segment overlapping was equal to 50%. So, there were 10 segments for the estimation of Fourier coefficient according to (9). Artificial series were processed by the bispectral analysis. The spectrum calculated was composed of three peaks at frequencies f_1, f_2, f_3. Fig.33 a, b show the bispectrum and bicoherence of series considered. The bispectrum and bicoherence levels are plotted as counters.

The bispectrum and bicoherence reveal the peak at frequencies $f_1 \approx 0.025$ min^{-1}, $f_2 \approx 0.043$ min^{-1}. The value of this peak for the bicoherence is close to 1.

Others maxima of $b^2(\omega_1,\omega_2)$ scattered in the $f_1 \div f_2$ domain are caused by additive noise n(t). The series (12) is an idealized model of interacting TIDs components. Measurements show (section 2.3) that TIDs exist as packets of oscillations taken places during a fraction of total records. Of course, this fact have to decrease a value of the bicoherence.

The bispectral analysis was applied to Doppler shift records used in the section 2.3 in connection with the study of packet like TID structures. Fig. 34 a, b show the bispectrum and bicoherence of a typical experimental record obtained in Feb. 23, 1989 between 10.40 and 18.40 LT at the operating frequency of 6.7 MHz. One can see a chain of spectral maxima along the line of F = 0.02 min^{-1}. Tables comprised frequencies participated into nonlinear interactions and values of correspondent bicoherences.

Table 9

N	f_1	f_2	f_1+f_2	$b^2(f_1,f_2)$
1	0.02	0.04	0.06	0.6
2	0.02	0.06	0.08	0.6
3	0.02	0.11	0.13	0.4
4	0.02	0.13	0.15	0.6
5	0.045	0.055	0.11	0.6
6	0.08	0.12	0.2	0.5

It is seen from Table 9 that many interacting frequencies are a sum of other interacting pairs. There seem to be the first order interactions (triplets number 1, 5) and the high order interaction (triplets number 2, 3, 4, 6).

Fig. 31 a, b show the bispectrum and bicoherence of an experimental record obtained in Feb. 12, 1989 between 10.00 and 17.00 LT at the operating frequency of 6.3 MHz . From a picture it can be seen a series of interacting triplets listed in the Table 10.

Table 10

N	f_1	f_2	f_1+f_2	$b^2(f_1,f_2)$
1	0.04	0.065	0.105	0.6
2	0.035	0.105	0.140	0.5
3	0.04	0.135	0.175	0.7
4	0.075	0.135	0.21	0.7

Similarly the record obtained in Feb. 23, 1989 this one demonstrates the first and high order interactions. The total number of records processed was 13. All records revealed wave - wave interaction between spectral components of TIDs.

Following Ma and Schlegel (1993) we can conclude that existing of high order interaction in our records shows an energy cascading from long periods to shorter ones. However, comparing Ma and Schlegel and our results we found one discrepancy deserving to be considered. Values of bicoherences under our consideration did not exceed 0.8 and their median value was 0.6. At the same time Ma and Schlegel (1993) estimated bicoherences to be 0.996, 0.98 and 0.98 for different interacting pairs. Such high values of bicoherences for experimental records are unusual and could be only expected for artificially generated data with a low level of the additional noise, where the conditions ($\omega_1+\omega_2=\omega_2$, $\psi_1+\psi_2=\psi_3$) of a resonant interaction between the full time existing frequencies are valid.

These high values of bicoherences seem to be caused by a relatively short length (5 hours) of the record processed by Ma and Schlegel (1993). In spite of discrepancy considered above following conclusions seem to be evident:

1. Nonlinear wave - wave interactions are common feature of TIDs propagation in the F - region of the ionosphere.

2. Existing of the high order nonlinear interactions appears to prove an energy cascading from long periods to shorter ones.

Acknowlegements

We are pleased to express our gratitude to leadership of EOARD Foundation and Air Force Laboratory for financial support of this project. Also we thank leadership of Institute of Ionosphere whose help we felt permanently.

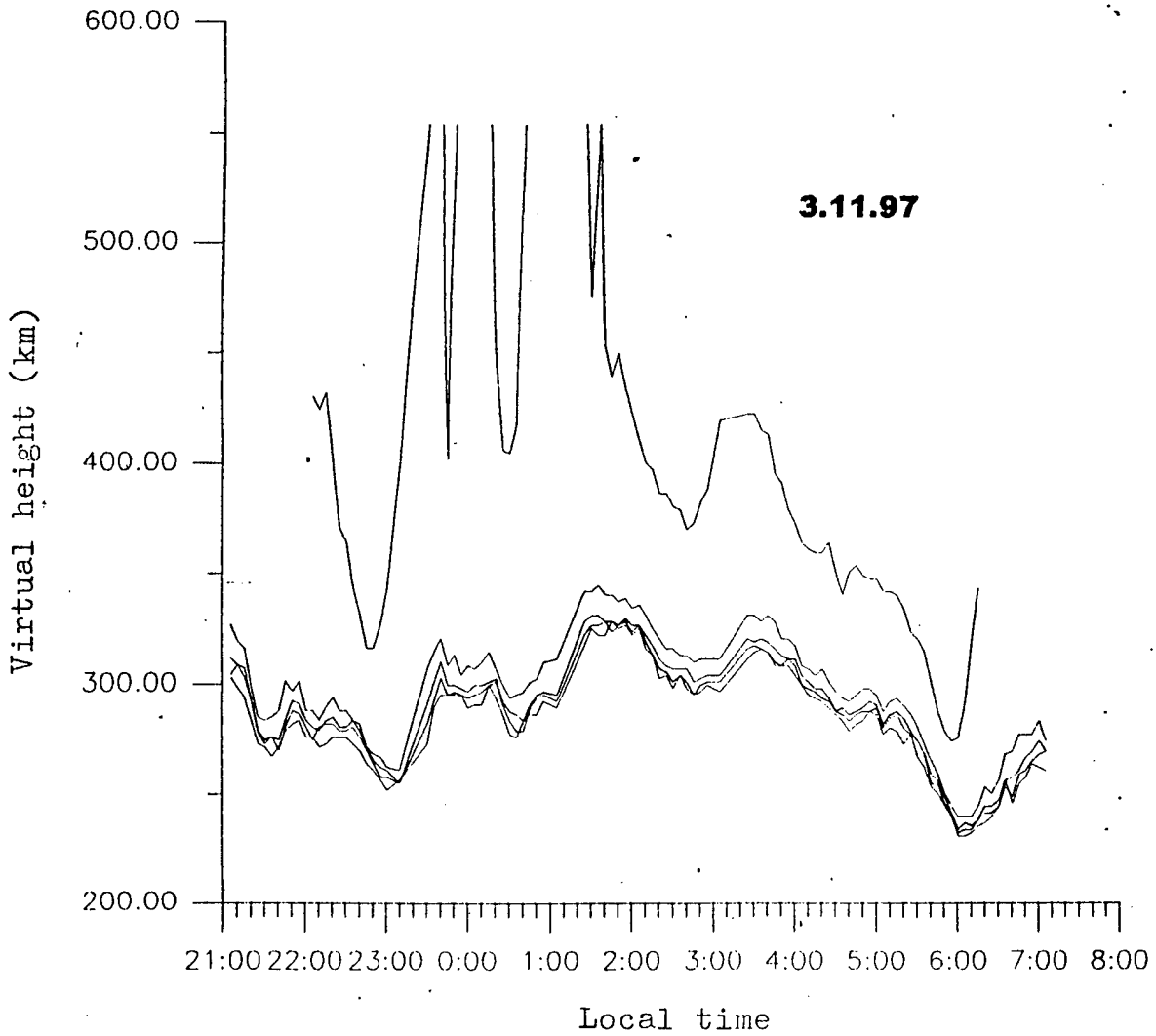

Fig.13. Plots of virtual height variations at set of operating frequencies in the night 3-4.11.1997.

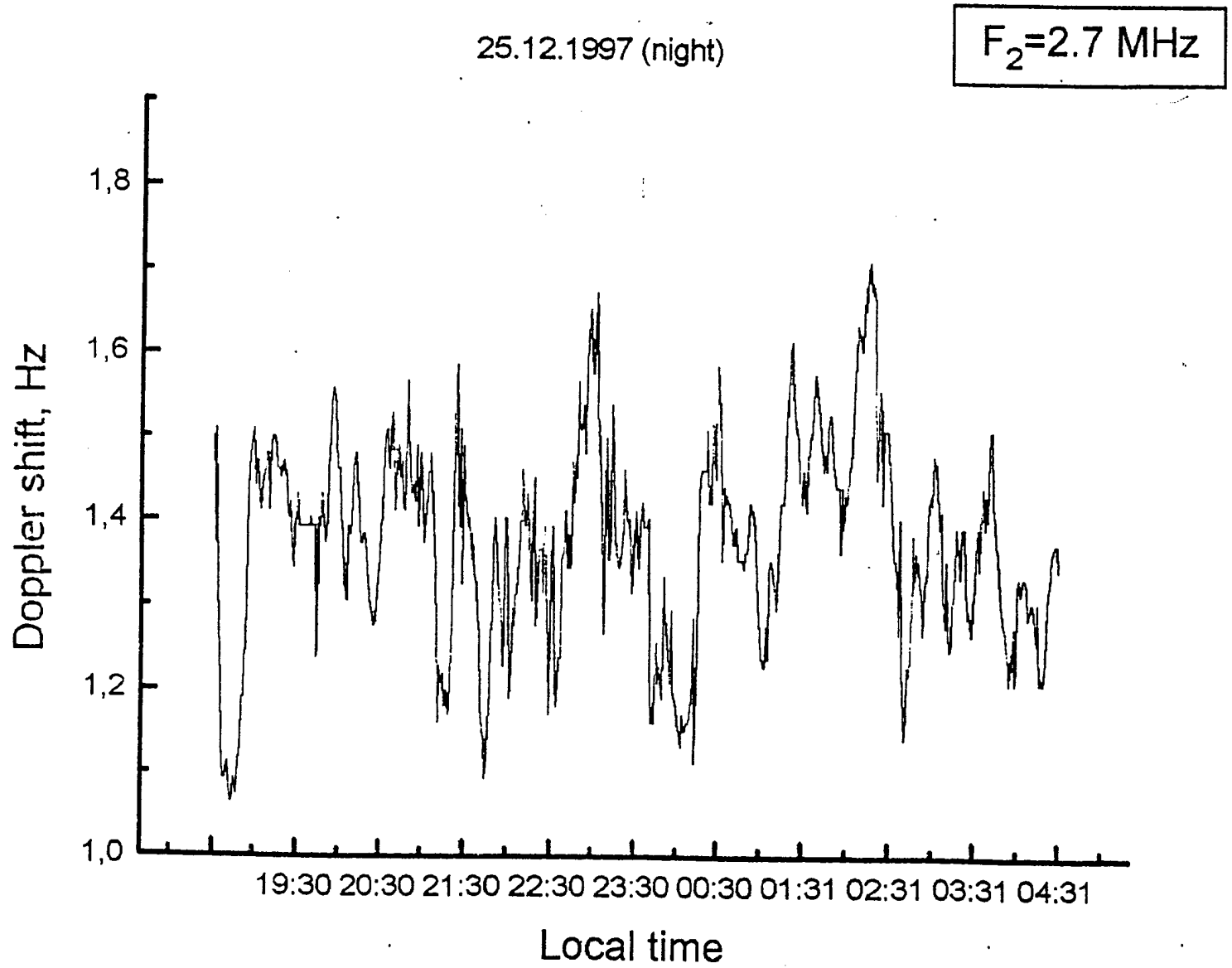

Fig.14. Example of Doppler shift variations.

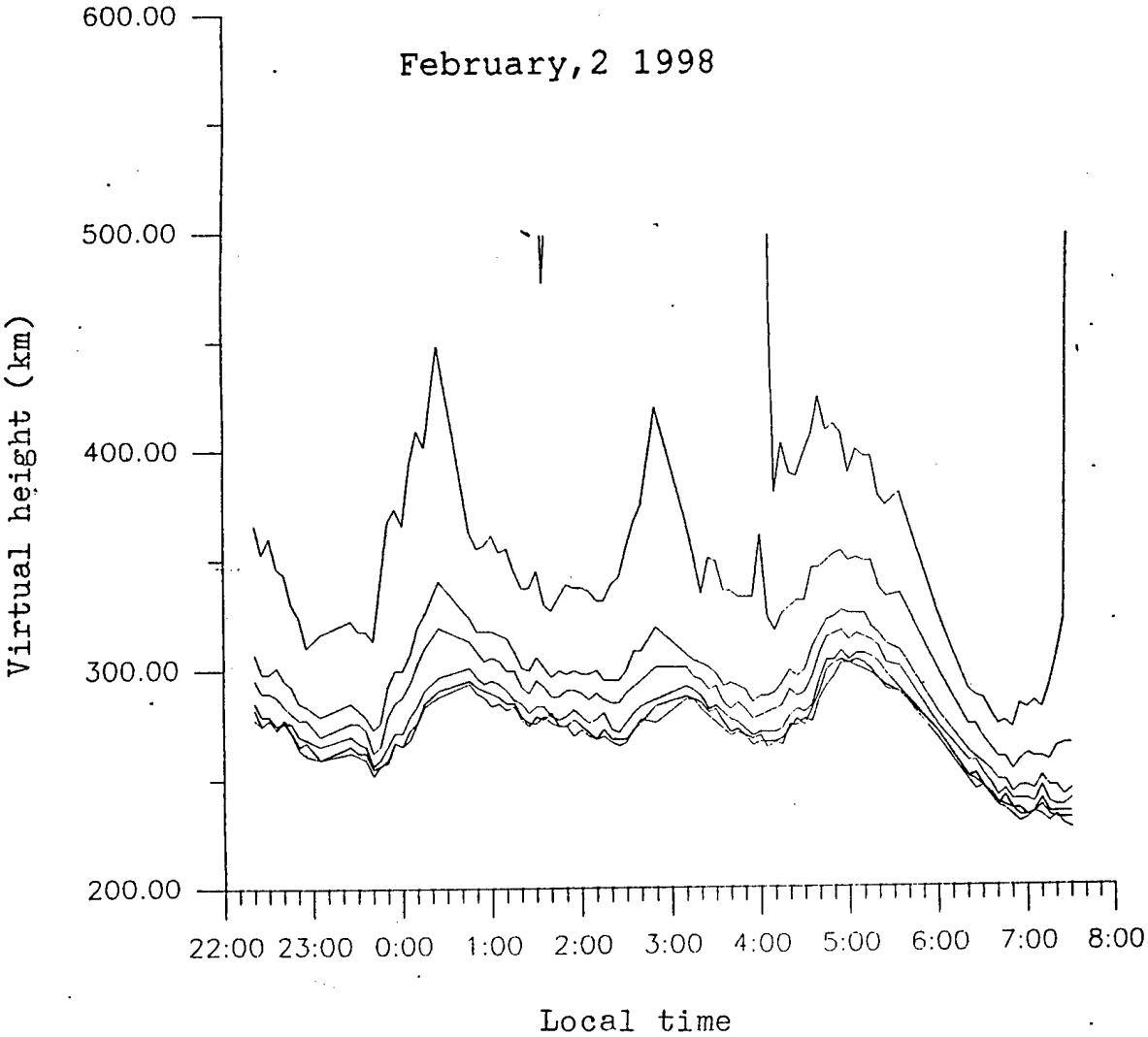

Fig.15 a. Plots of virtual height variations in the night 2-3.02.1998.

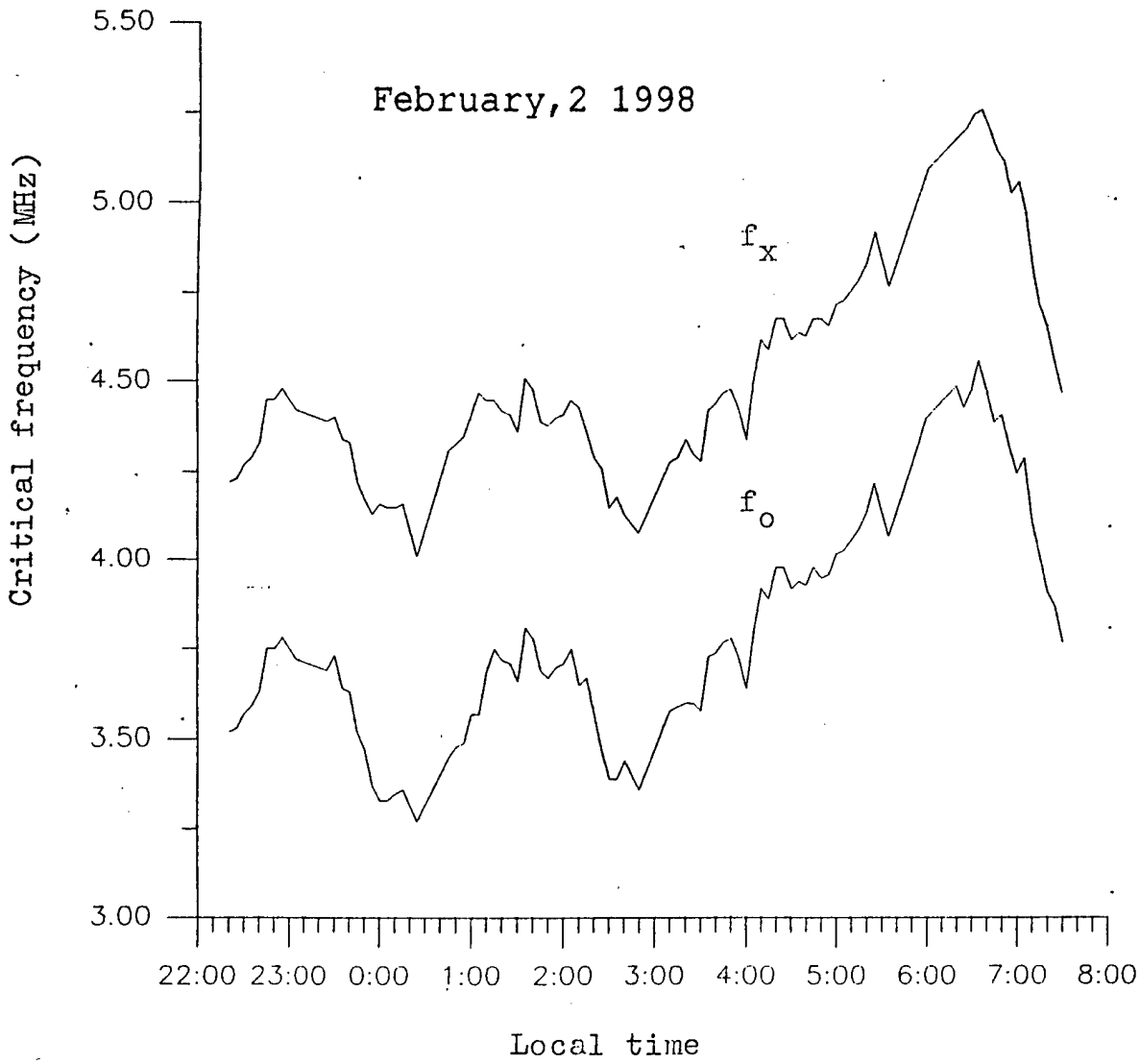

Fig.15b. Plots of critical frequency variations in the night 2-3.02.1998.

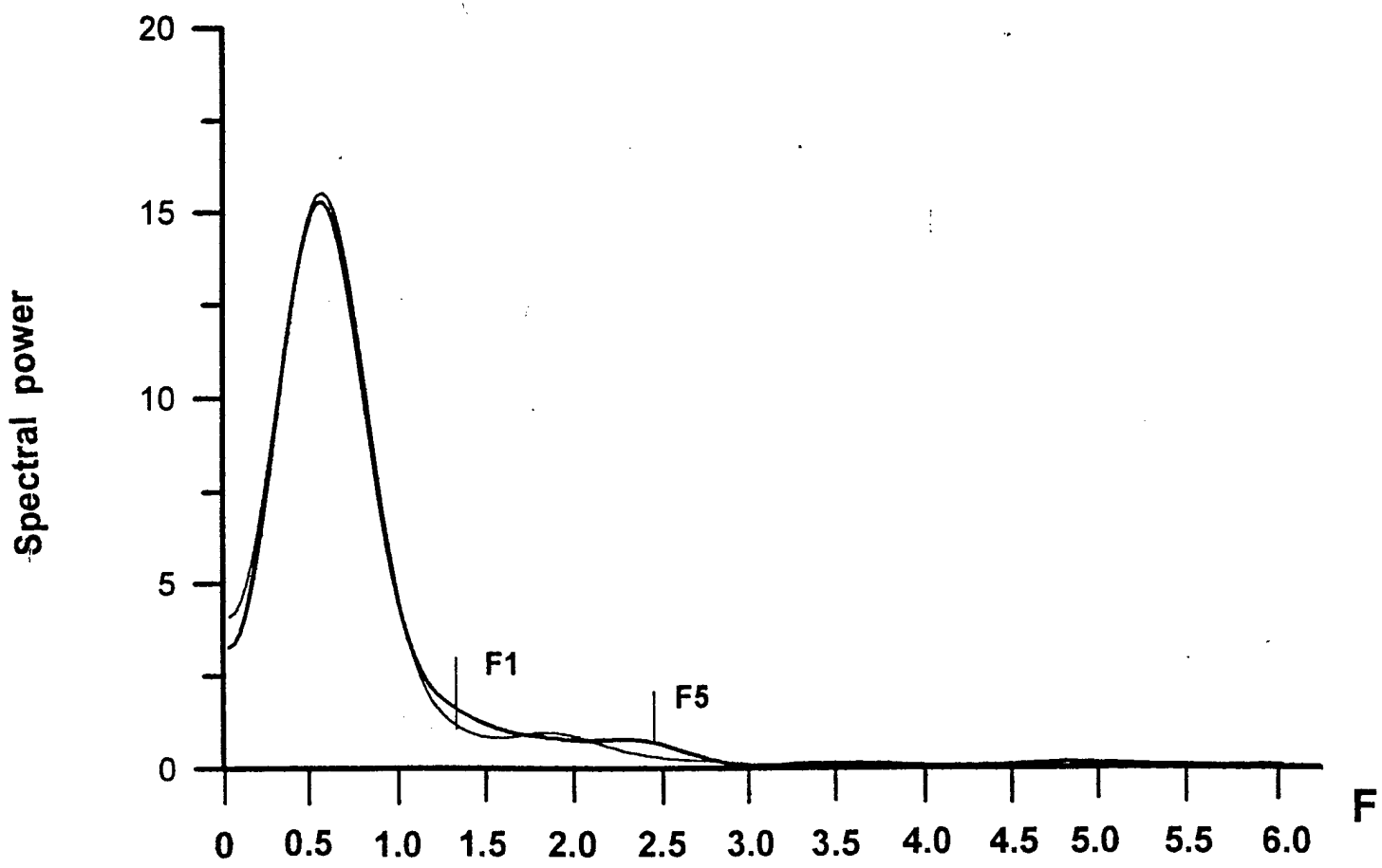

Fig.16 Spectra of virtual heights variations for operating frequences F1=2.5 MHz and F5=3.5 MHz (Feb.2,98)

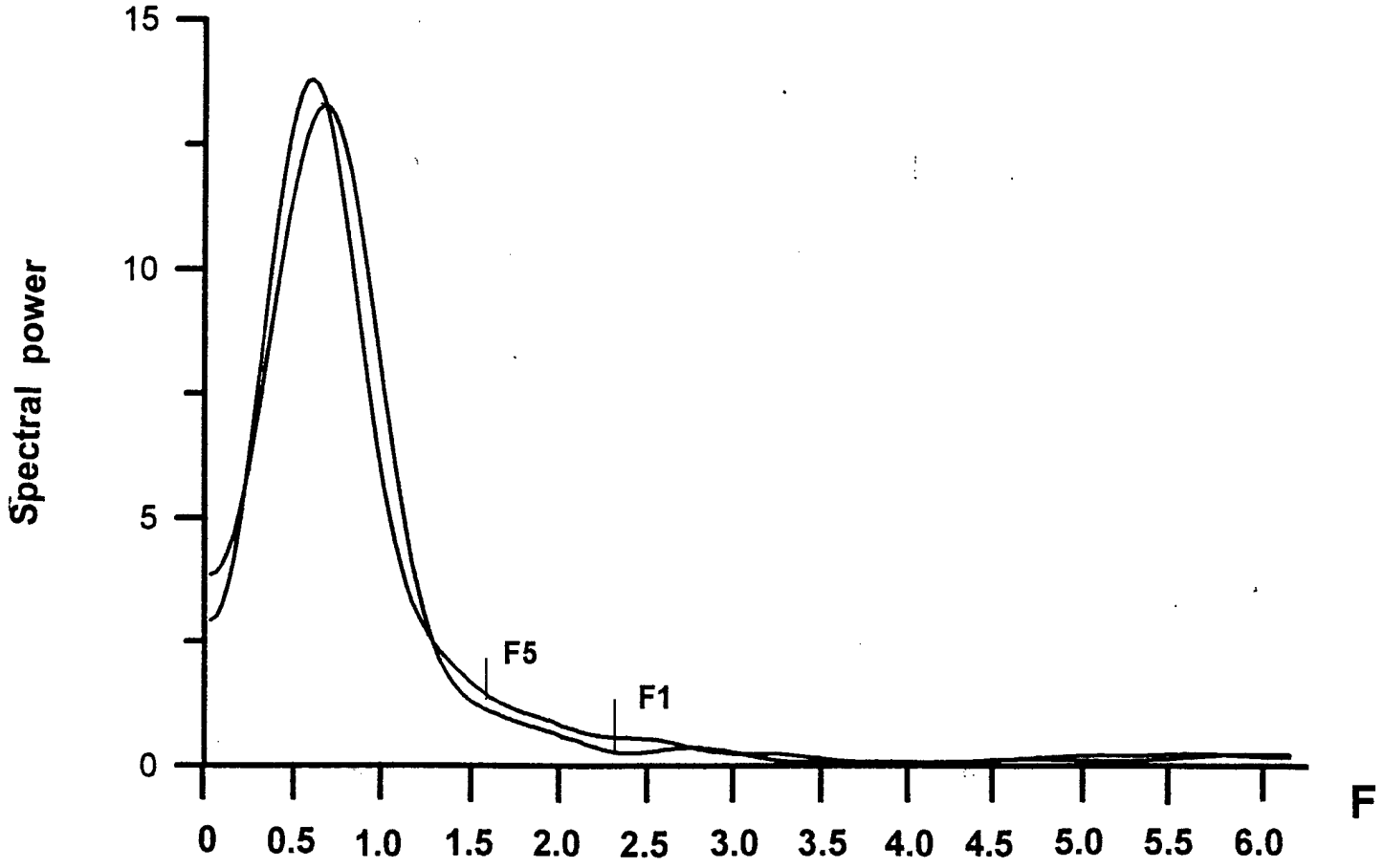

Fig.17 Spectra of virtual heights variations for operating frequences F1=2.5 MHz and F5=3.5 MHz (Dec.25,97)

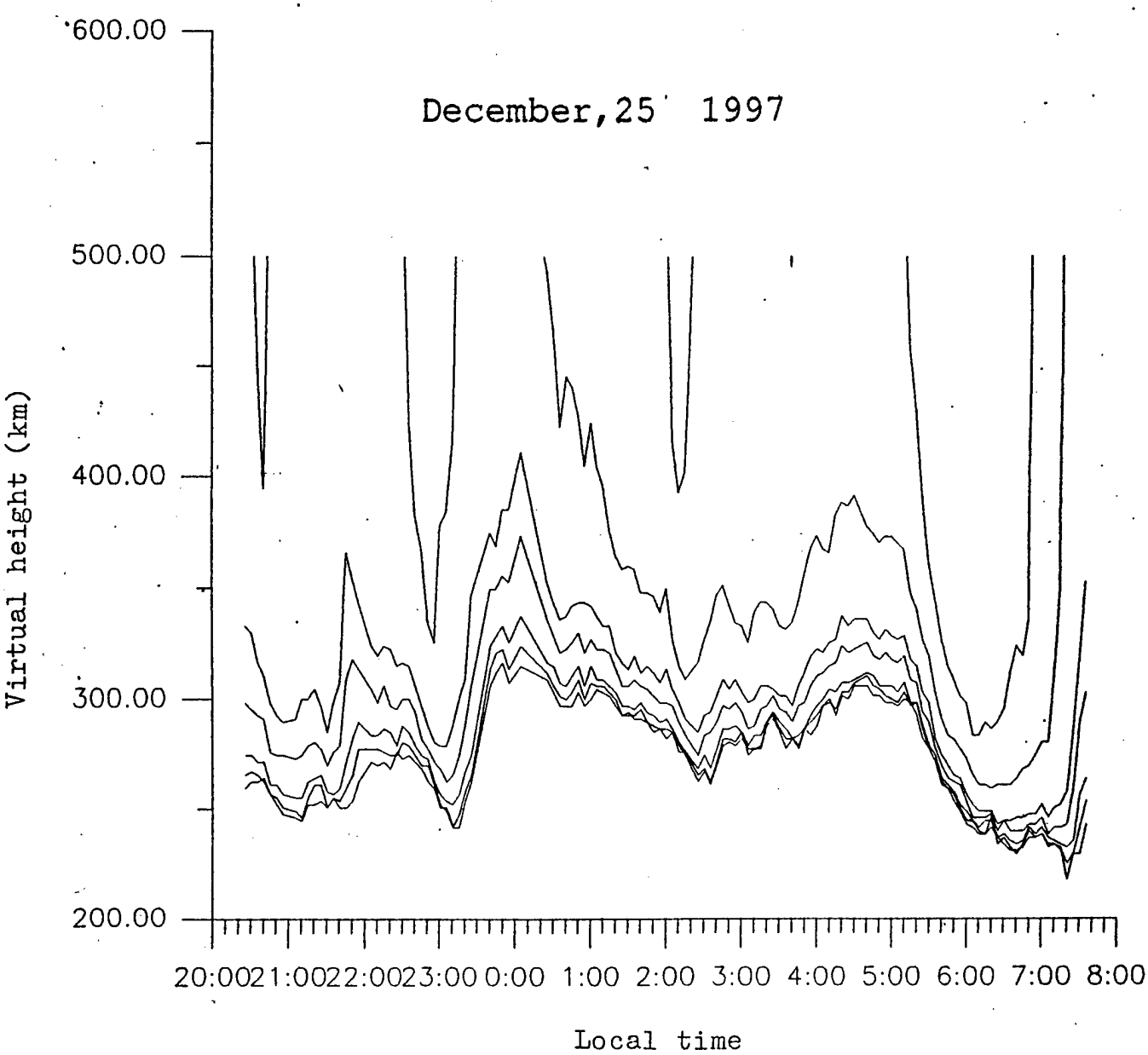

Fig.18. Plots of virtual height variations in the night 25-26.12.1997.

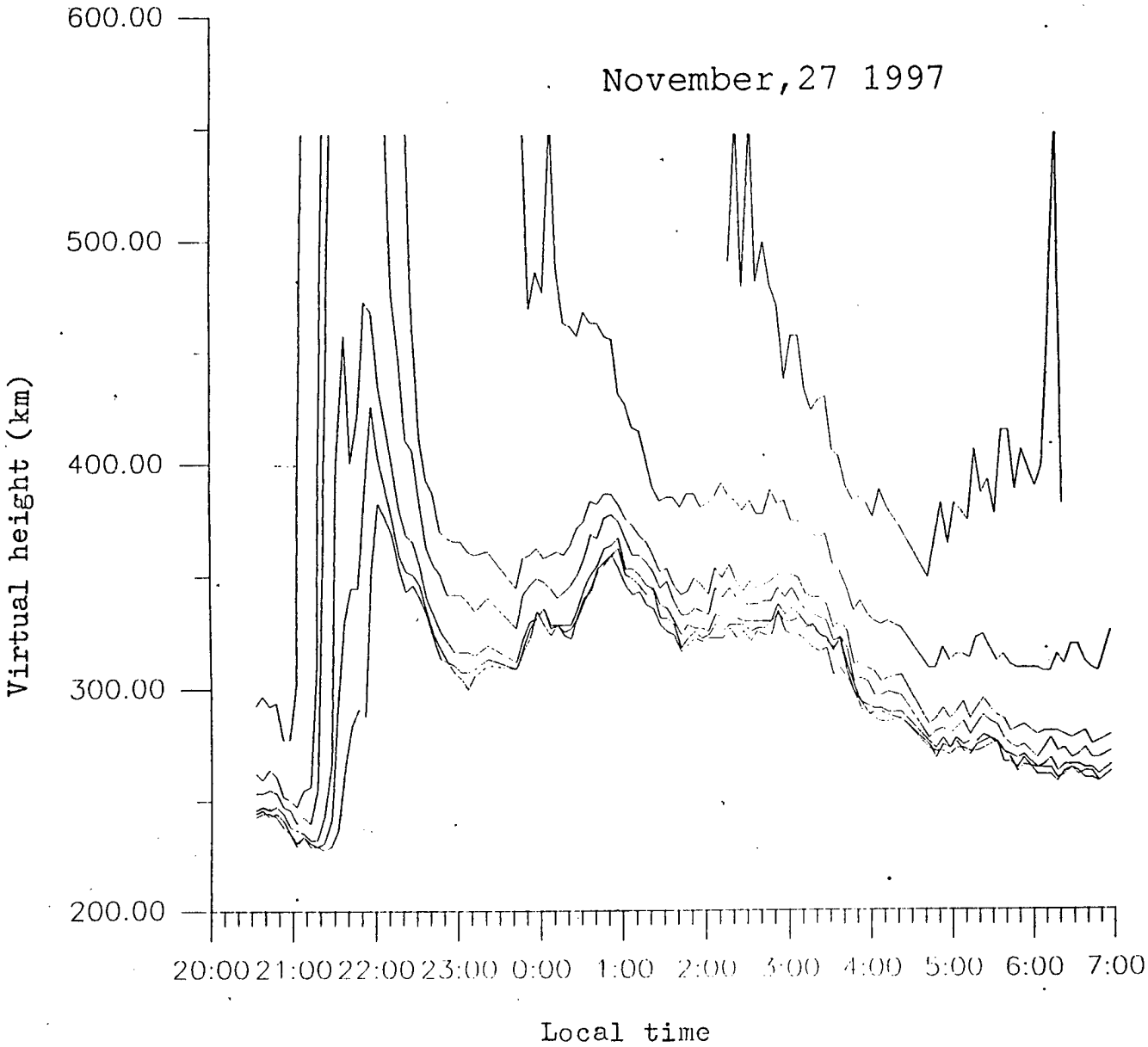

Fig.19. Plots of virtual height variations in the night 27-28.11.1997.

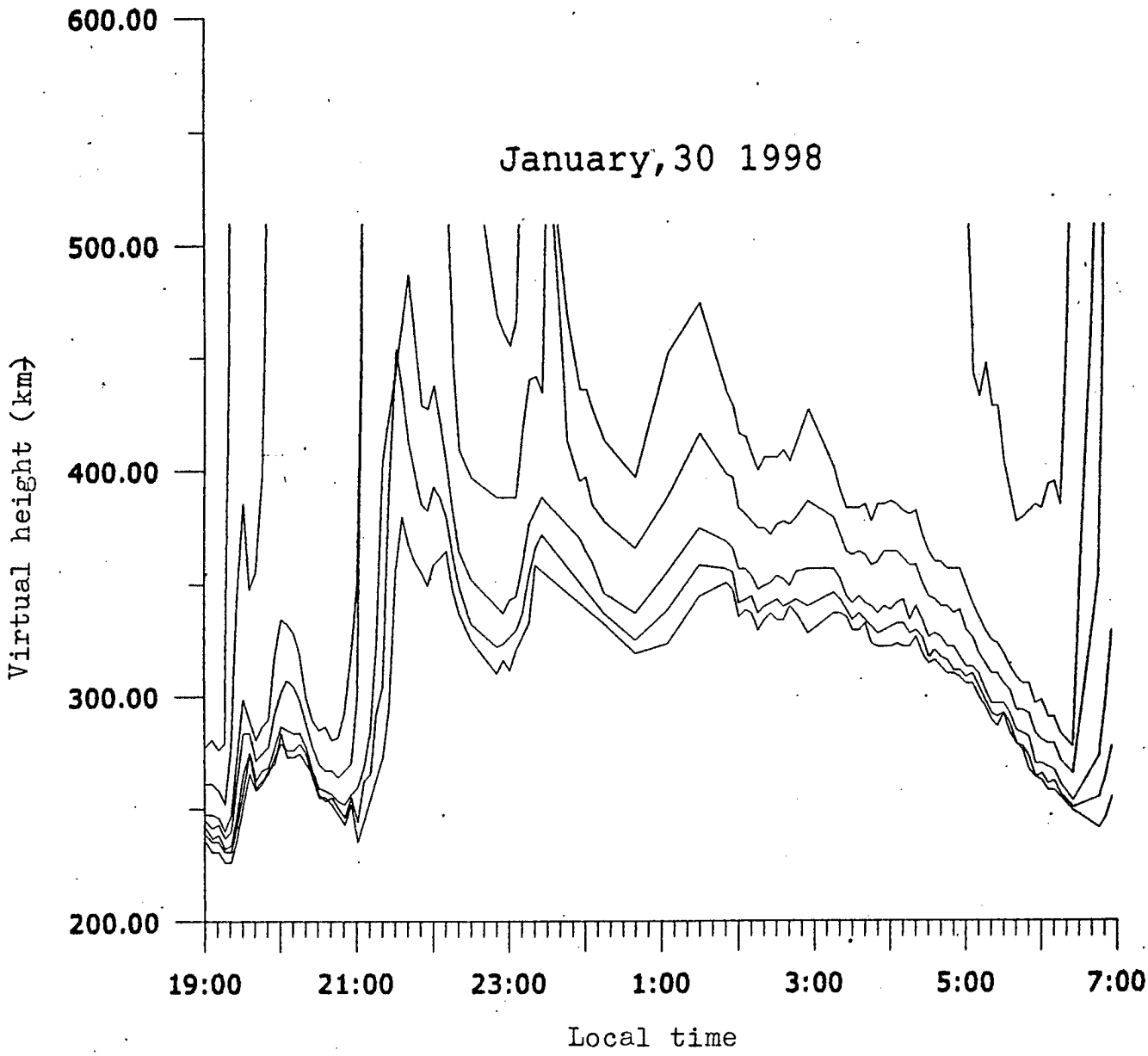

Fig.20. Plots of virtual height variations in the night 30-31.01.1998.

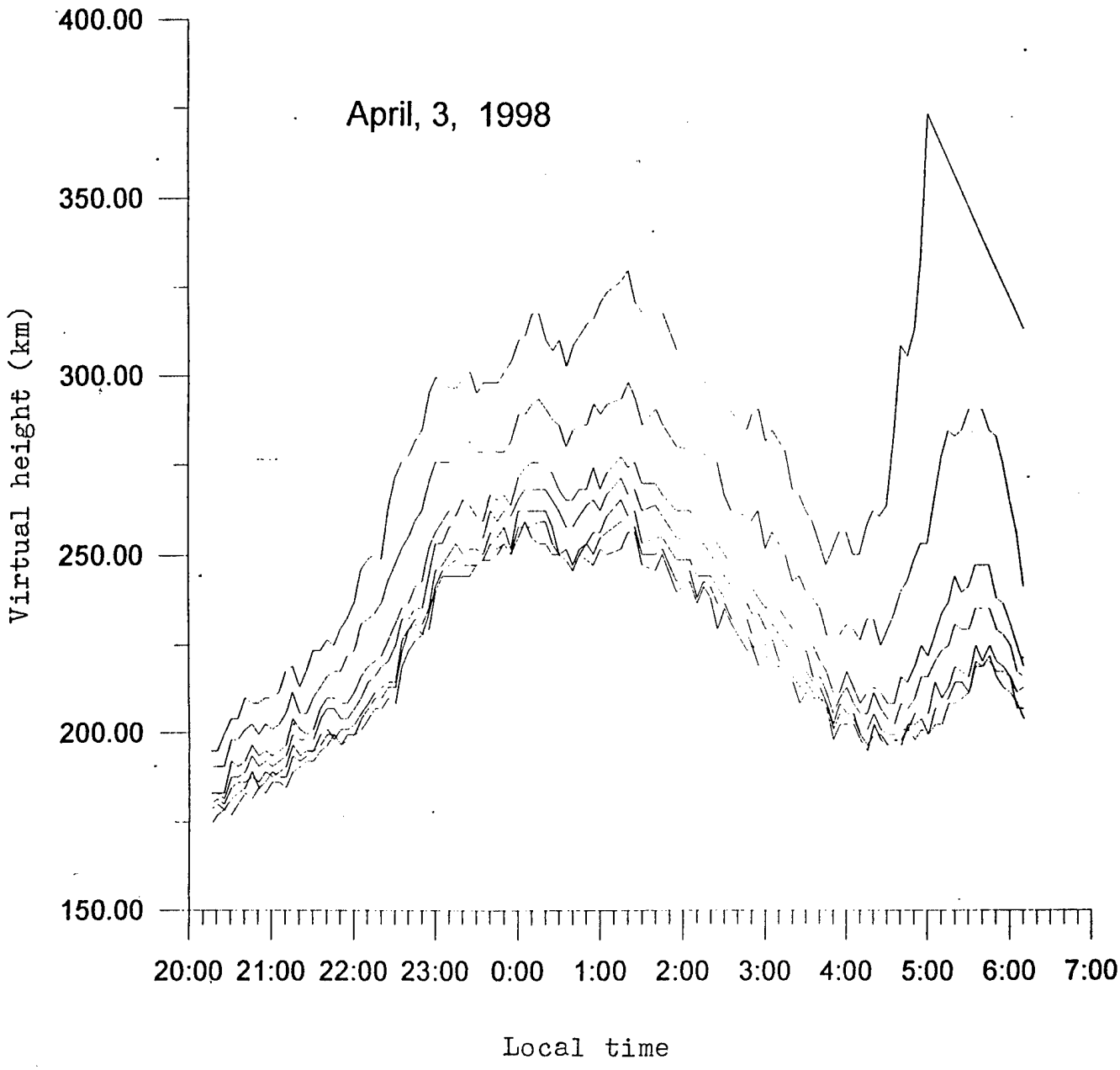

Fig.21. Plots of virtual height variations in the night 3-4.04.1998.

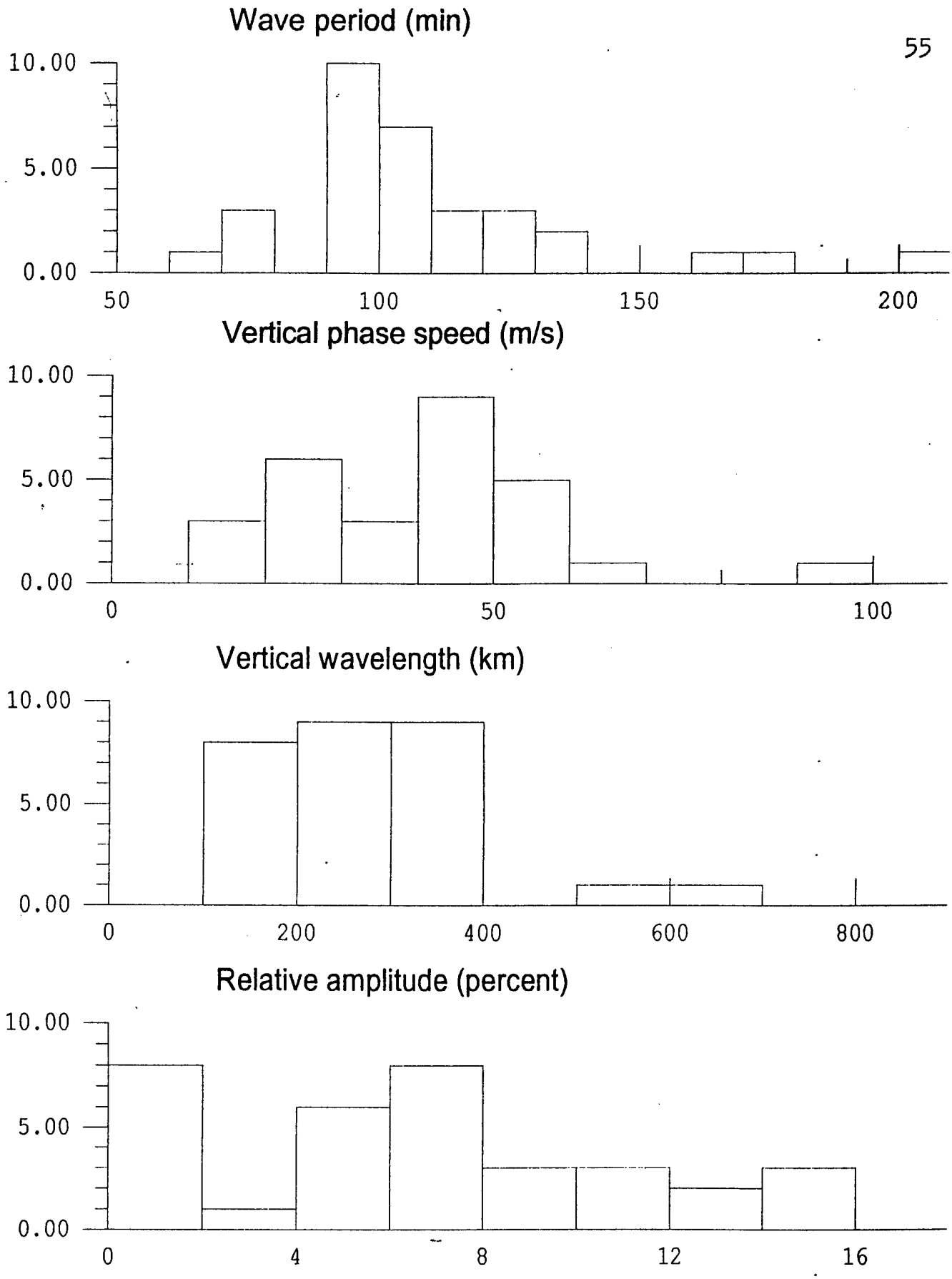

Fig.22. Distributions of wave periods, vertical phase speeds, wavelength and relative amplitudes for waves analyzed.

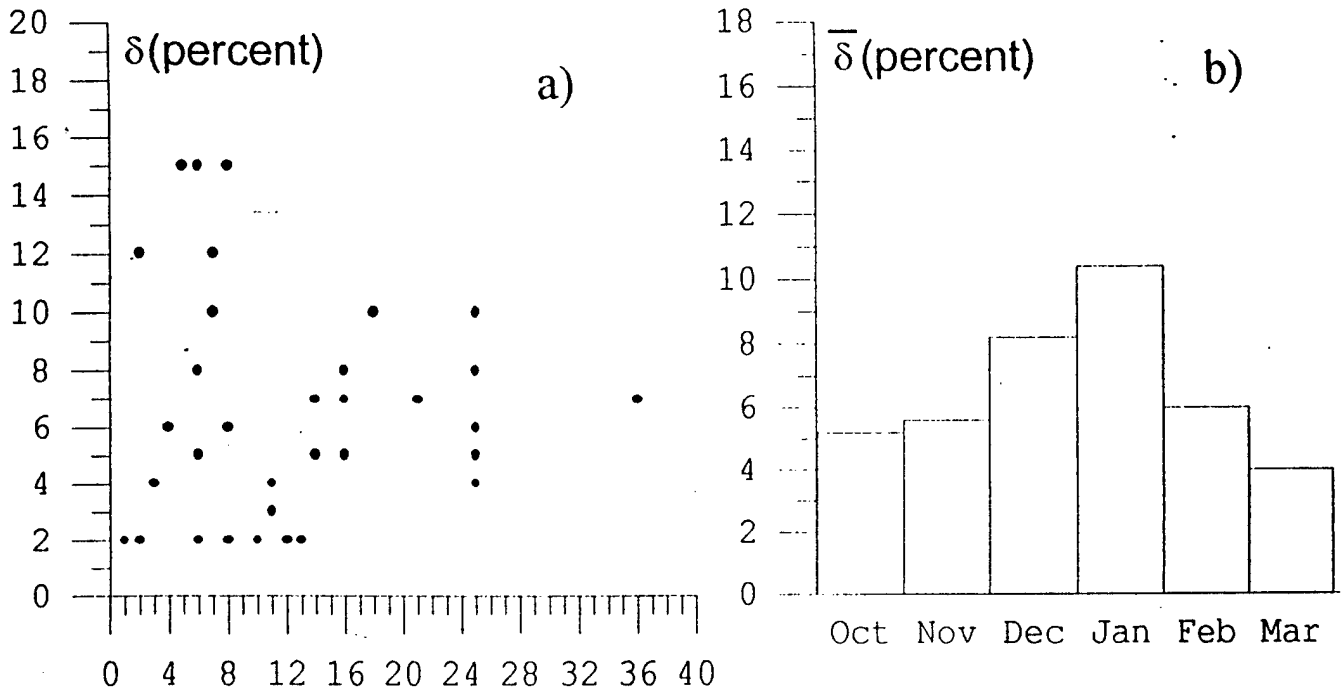

Fig. 23. Relative amplitude versus K_p-index (a), averaged relative amplitude versus month of observations (b).

27 November, 1997

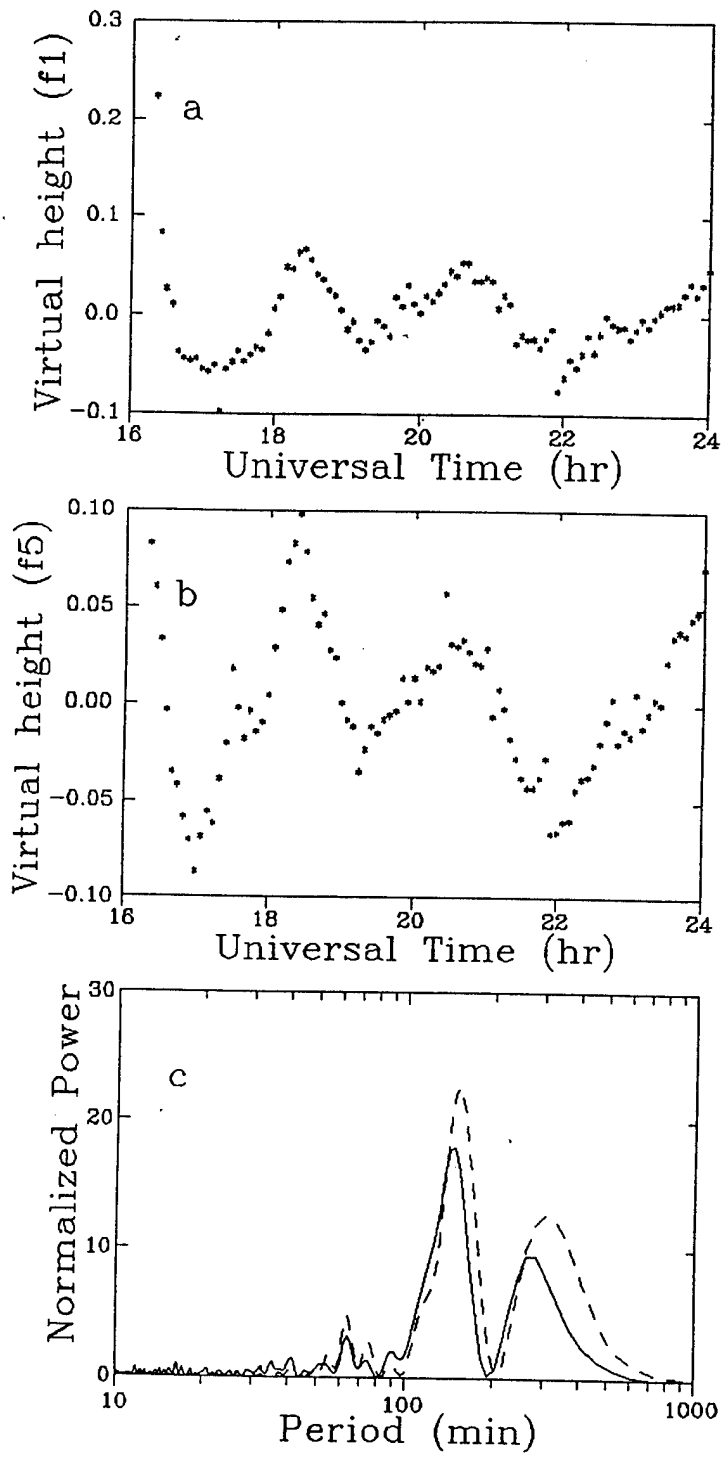

Fig.24. Detrended variatios of normalized virtual heights at the frequency f_1 (a), the frequency f_5 (b) and their normalized power for Nov.27,1997.

2 February, 1998

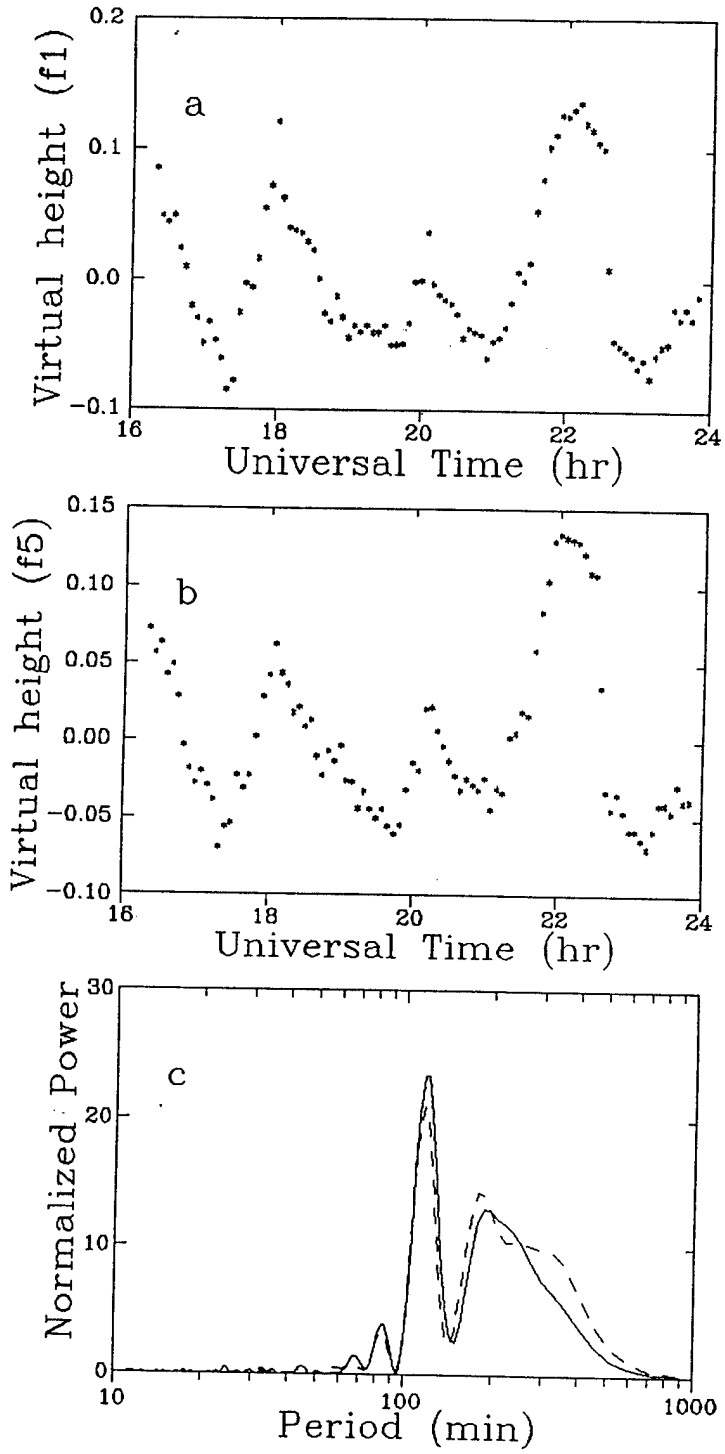

Fig.25. The same as in Fig.24 for Feb.2, 1998.

23 March, 1998

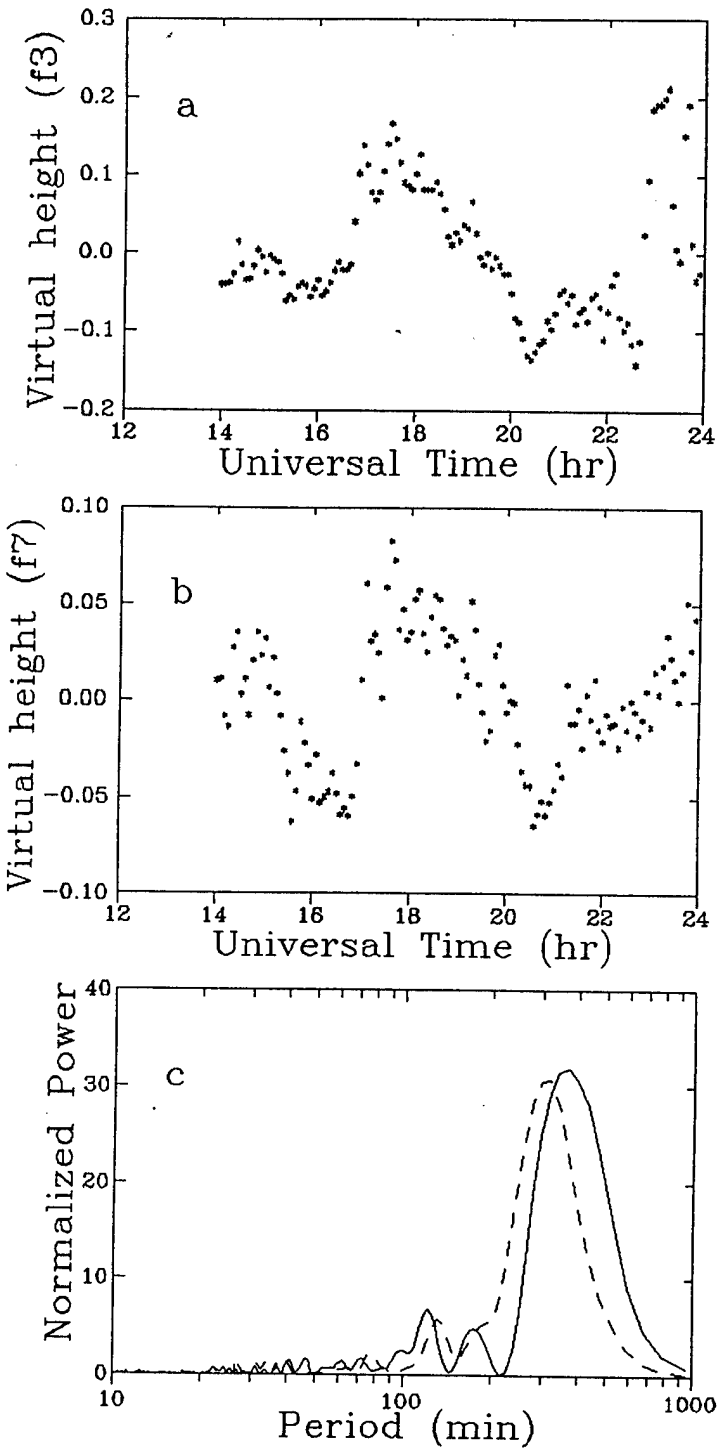

Fig.26. The same as in Fig.24 for 23 March,1998.

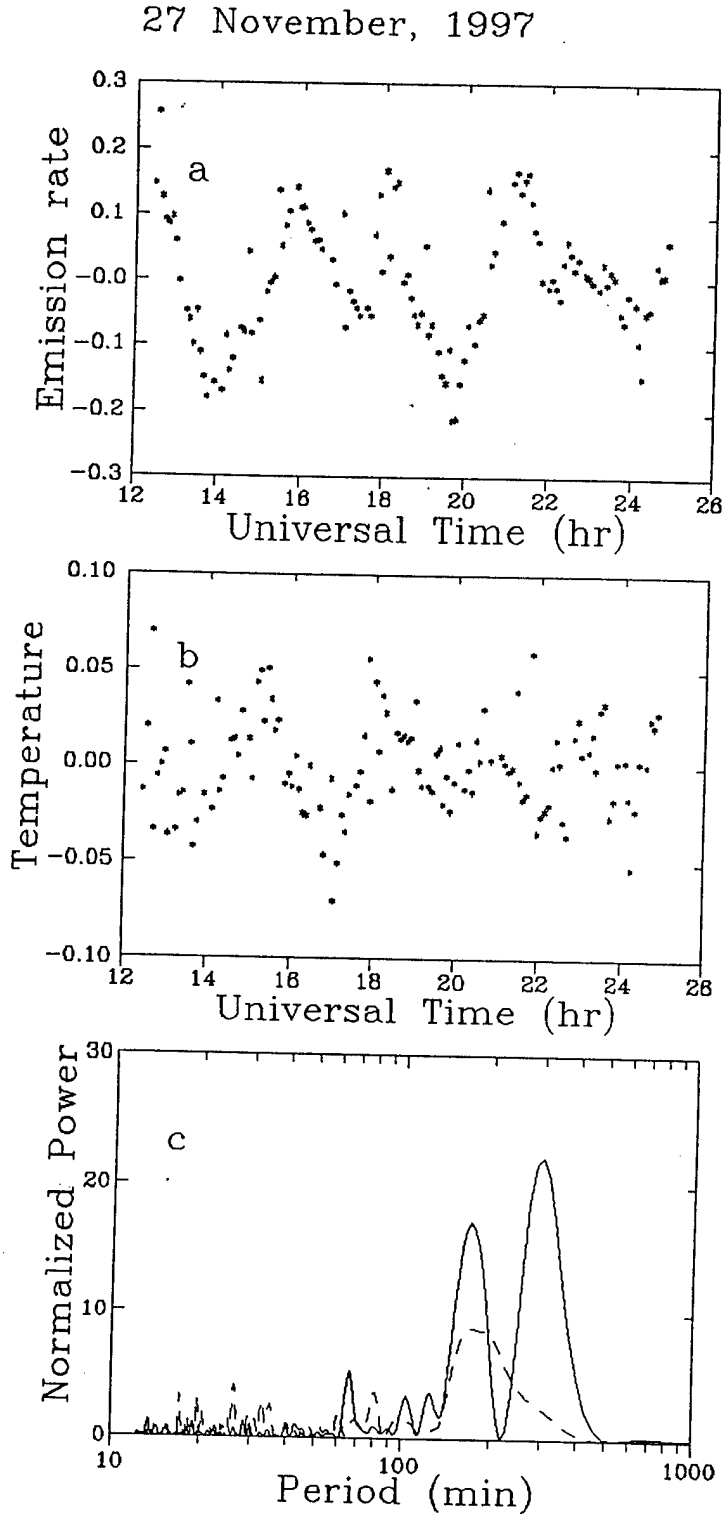

Fig.27. The same as in Fig.2 with removed the 500min component.

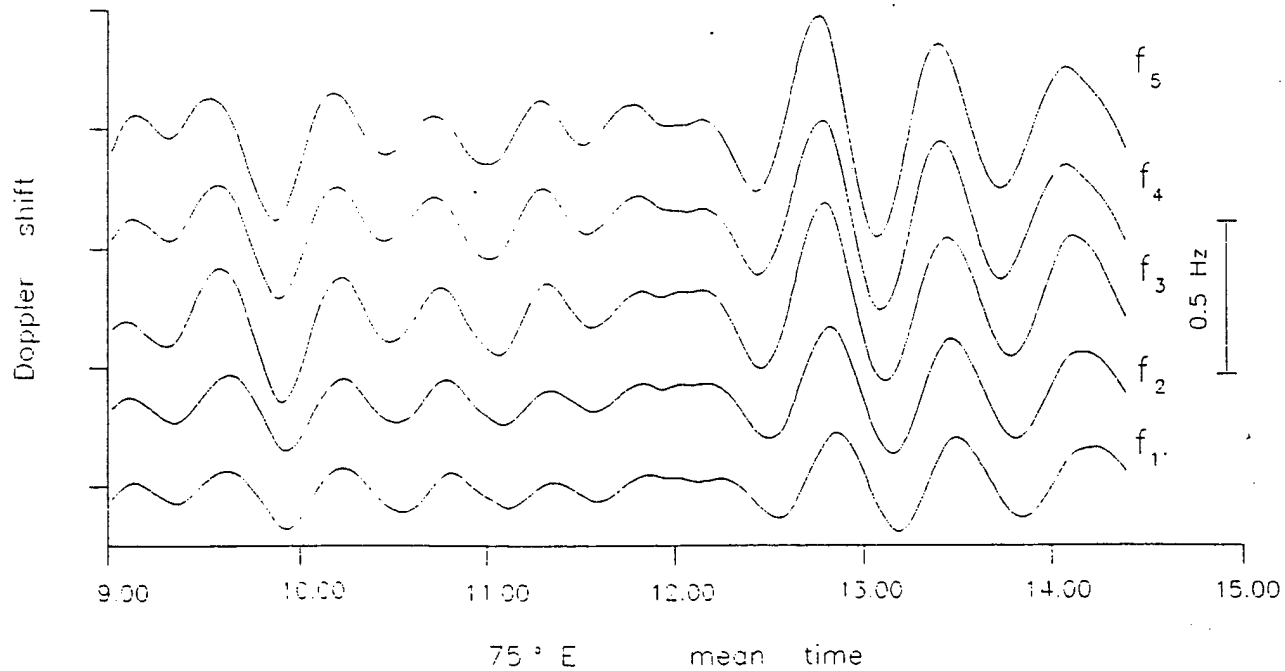

Fig.28. Examples of Doppler shift variations recorded in March 17, 1988 at operating frequencies f_1=5.4 MHz, f_2+5.7 MHz, f_3=6.3 MHz, f_4=6.7 MHz, f_5= 7.4 MHz and passed through the filter with the central frequency F=1.5 cph. The vertical bar denotes the 0.5 Hz scale of the Doppler shift variations.

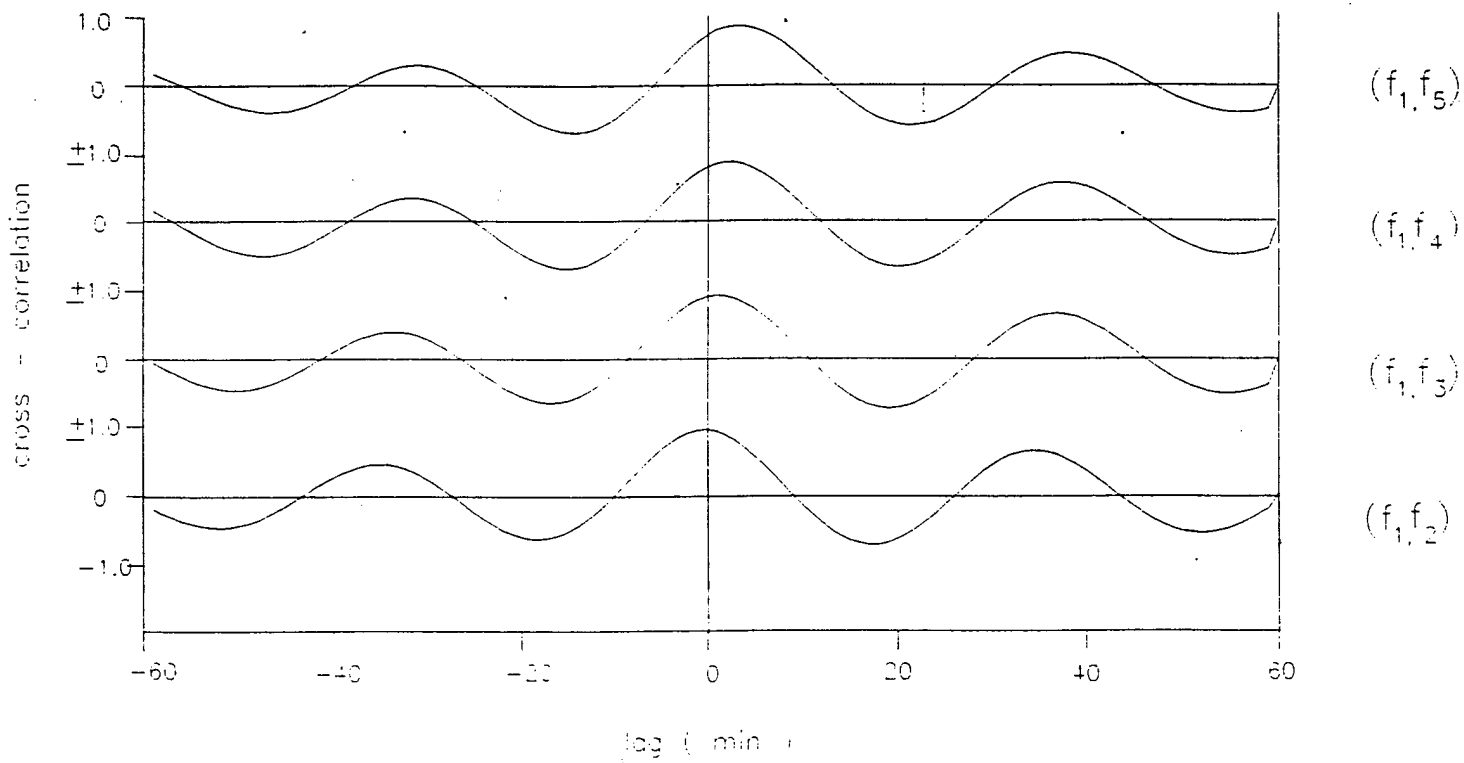

Fig.29. Cross-correlation functions between quasi-stochastic parts of Doppler shift variations plotted in Fig. 24.

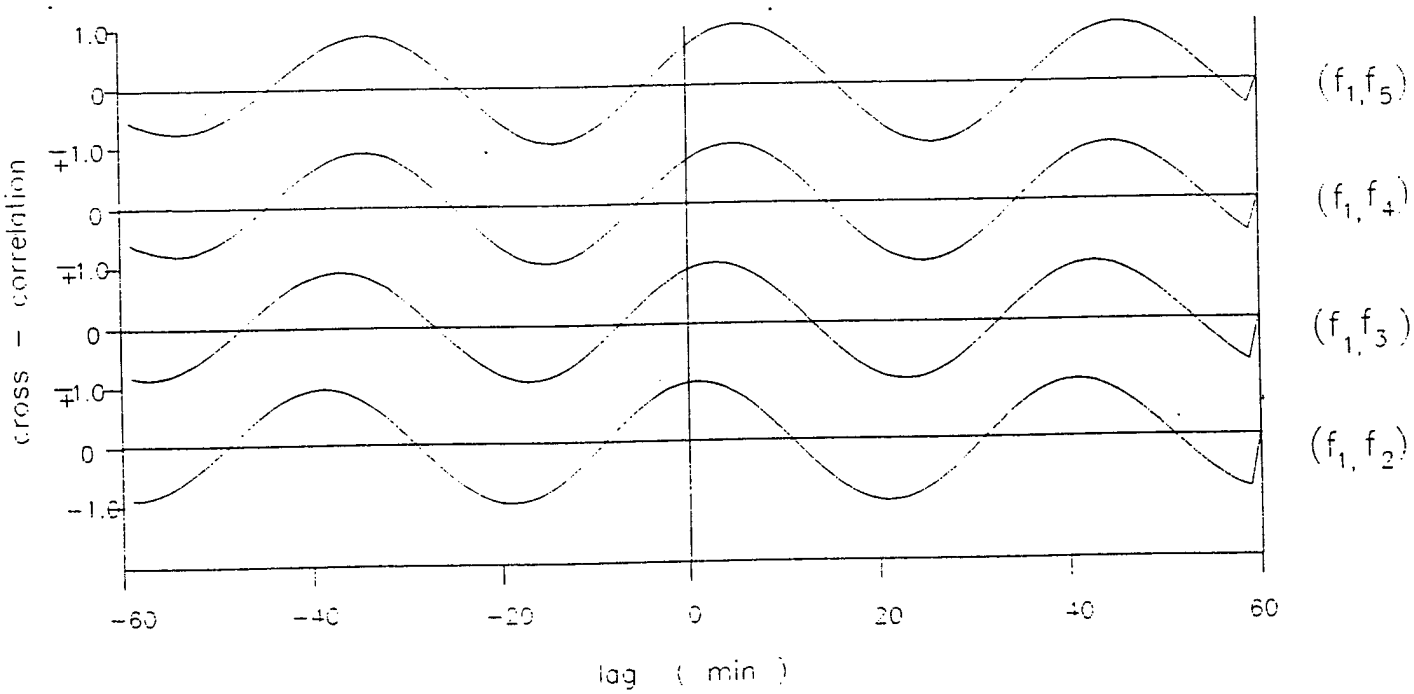

Fig.30. Cross-correlation functions between packet-like parts of Doppler shift variations plotted in Fig.24.

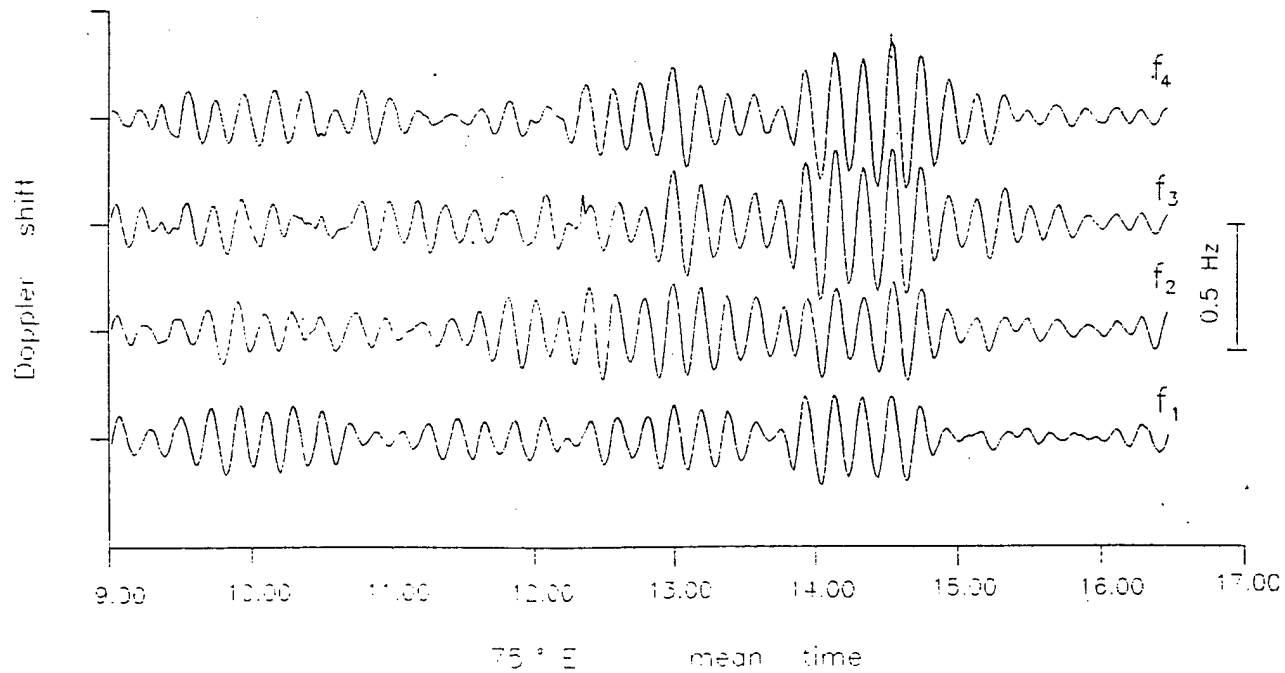

Fig.31 a. Examples of Doppler shift variations recorded in Feb.14,1990 at operating frequencies f_1=6.6 MHz, f_2=8.7 MHz, f_3=10.1 MHz, f_4=10.7 MHz and passed through the filter with the central frequency F=5.0 cph. The vertical bar denotes the 0.5 Hz scale of the Doppler shift variations.

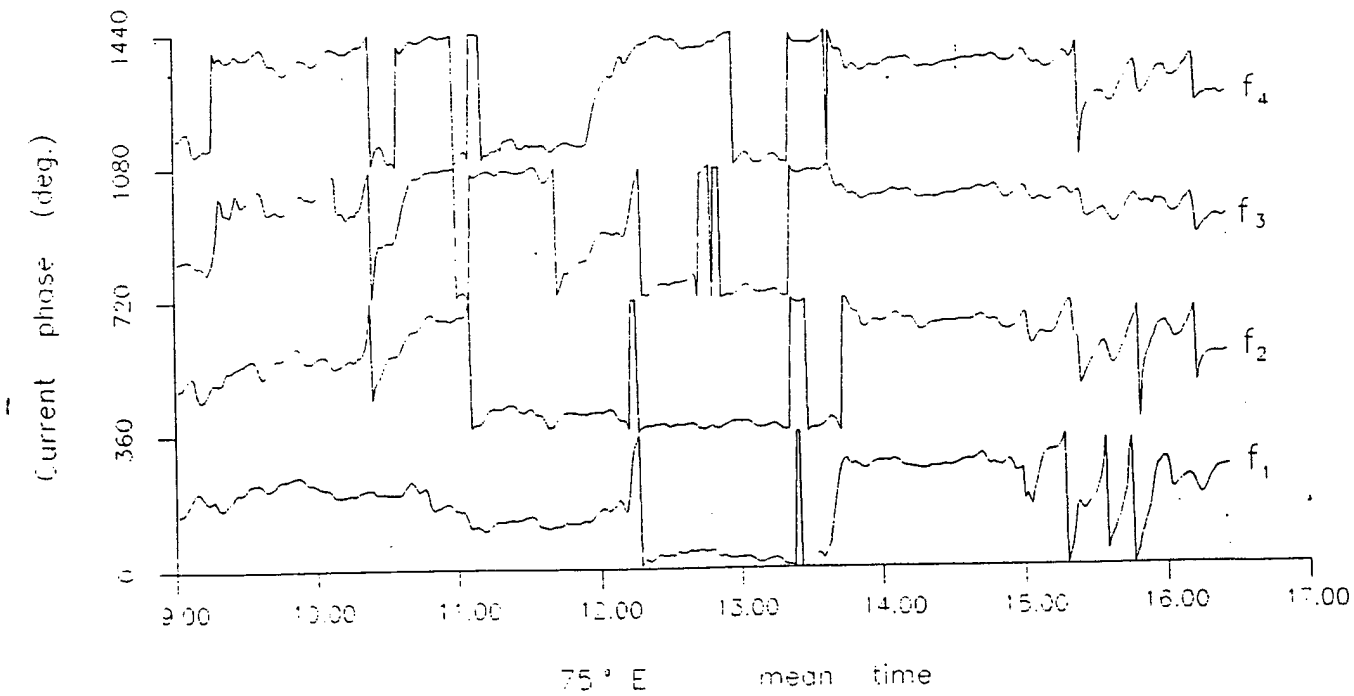

Fig.31b. Examples of the current phase behaviour of the filtered Doppler shift variations plotted in Fig.27a.

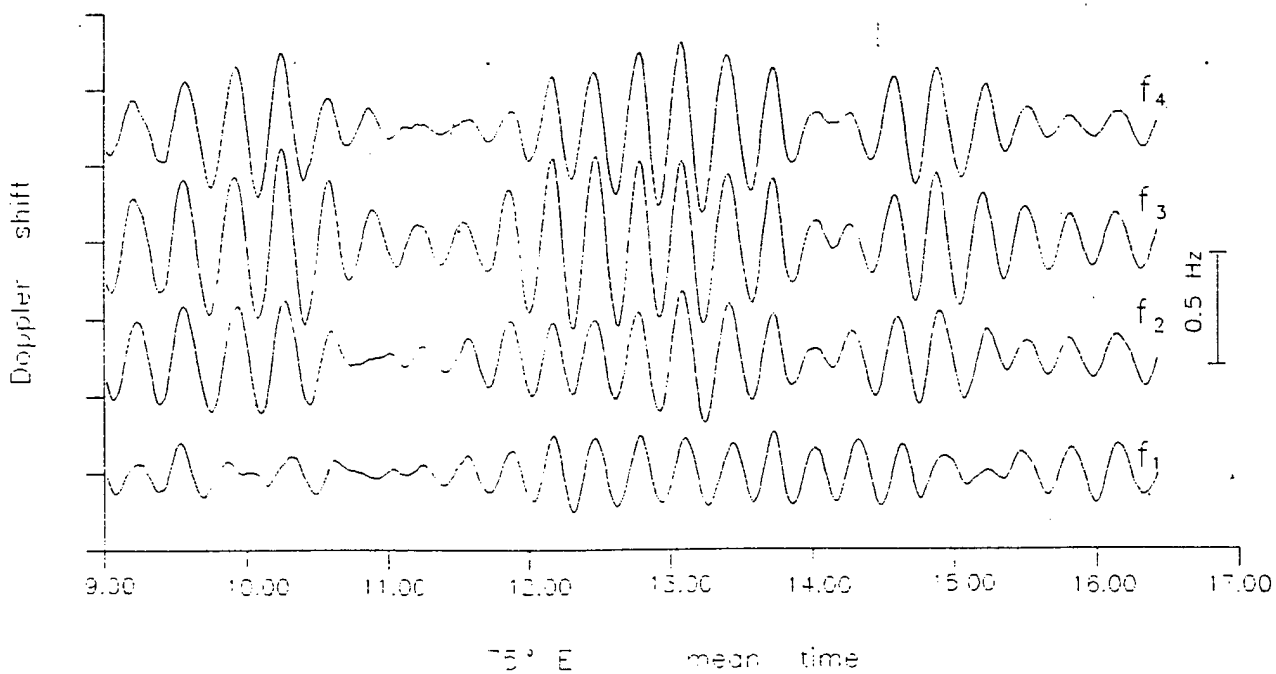

Fig. 32a. Examples of Doppler shift variations recorded in Feb.14,1990 at operating frequencies f_1=6.6 MHz, f_2=8.7 MHz, f_3=10.1 MHz, f_4=10.7 MHz and passed through the filter with the central frequency F=3.0 cph. The vertical bar denotes the 0.5 Hz scale of the Doppler shift variations.

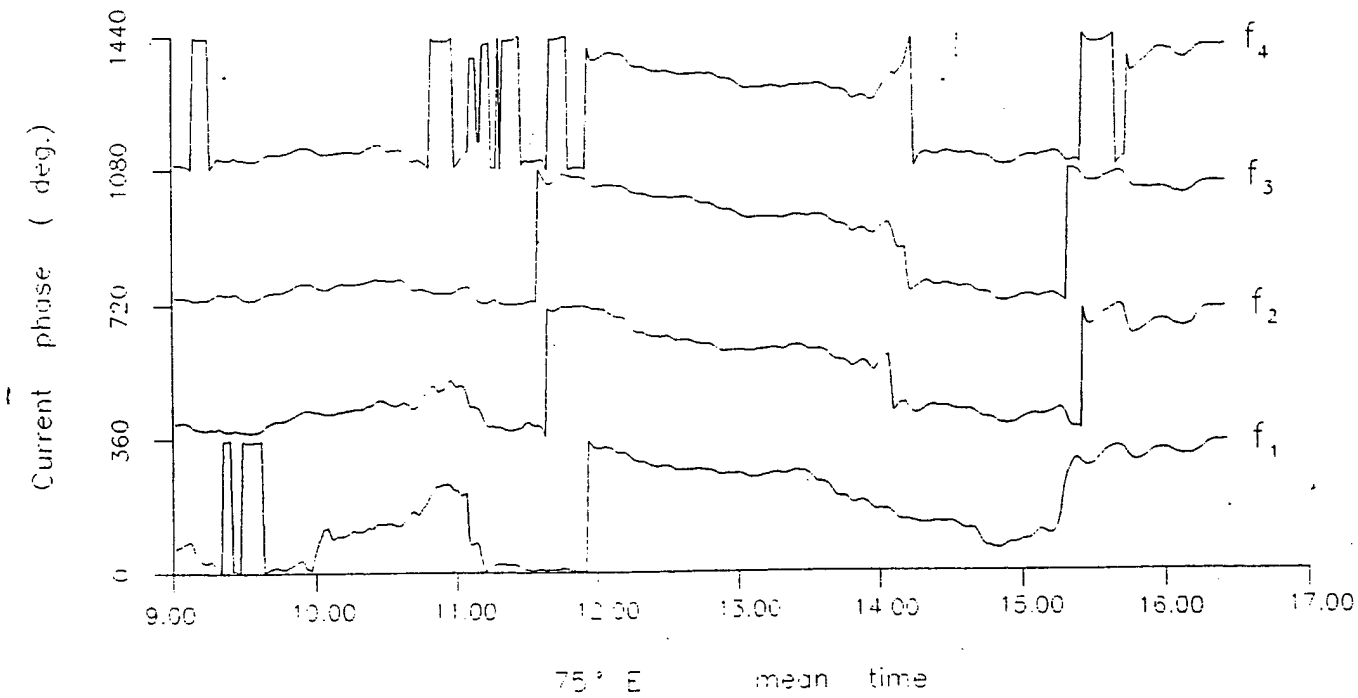

Fig.32 b. Examples of the current phase behaviour of the filtered Doppler shift variations plotted in Fig.28a.

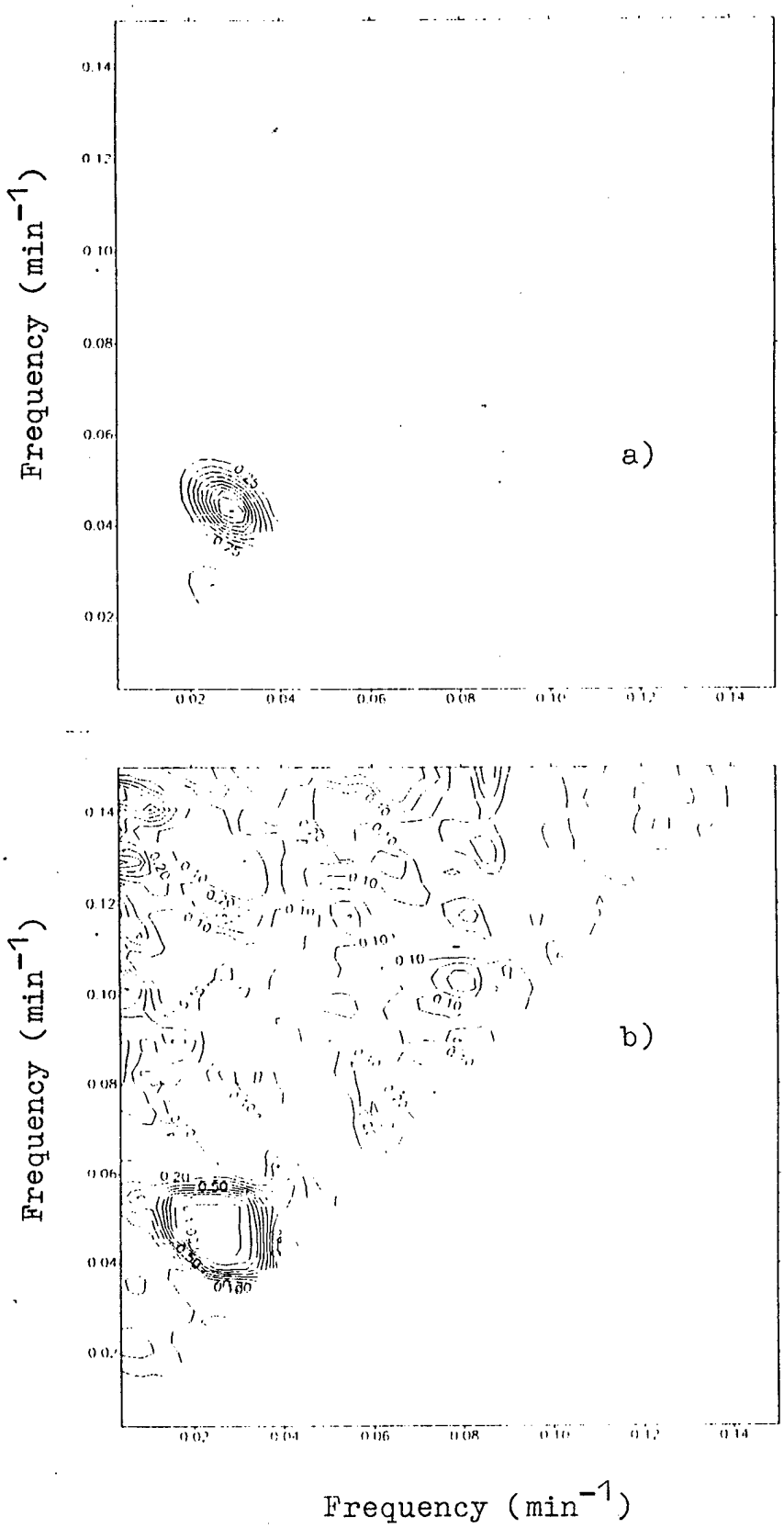

Fig.33. Bispectrum (a) and bicoherence (b) for artificial series.

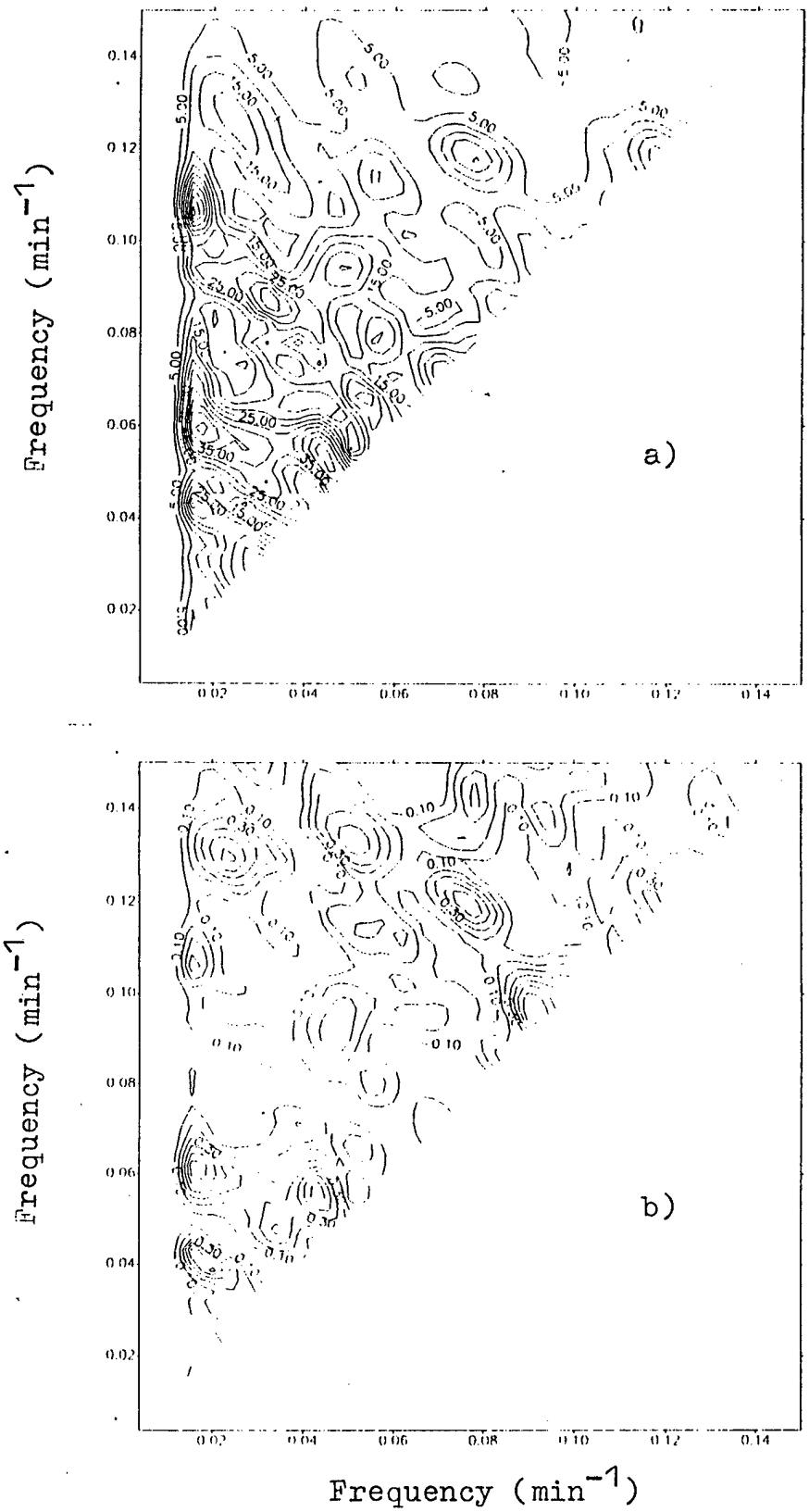

Fig.34 .Bispectrum (a) and bicogerence (b) for the experimental record obtained in Feb.23,1989.

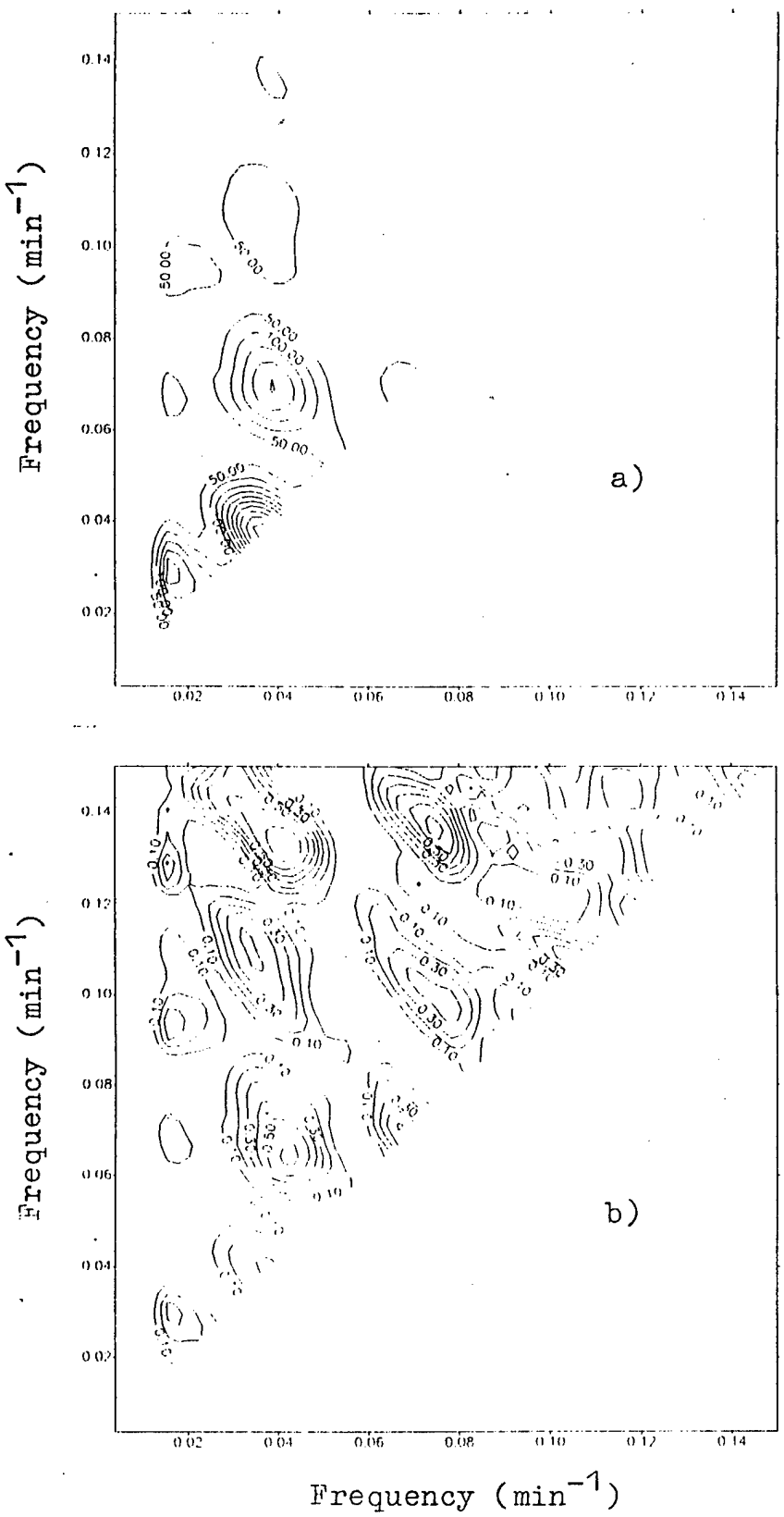

Fig. 35. Bispectrum (a) and bicogerence (b) for the experimental record obtained in Feb.12,1989.

References.

Beggs H.M. and Butcheer E.C. A study of travelling ionospheric disturbances over Macquare Island using an oblique CW sounder.- *Plan. Space Sci.*,1989, v..37 p.967-978.

Bidlingmayer E.R. and Pogoreltsev A.I. Numerical modelling of the transformation of acoustic-gravity waves into thermal conduction and viscous waves in the thermosphere.- *Izv. Russian Acad. Sci., Atmos. Oceanic Phys.*, 1992, Vol. 28, No 1, p. 64-74, in Russian (English Edition: *Izv. Russian Acad. Sci., Atmos. Oceanic Phys.*, 1992, Vol. 28, No 1, p. 48-55).

Bonsanto M.J. Observed and calculated F2 peak heights and derived meridional wind at mid-latitudes over a full solar cycle.- *J. Atmos. Terr. Phys.*, 1990, v. 52, 223.

Briggs B.H., Phillps G.Y. and Shinn D.H. The analisis of observation on spaced recievers of the fading of radio signals.- *Proc. Phys. Soc.*, 1951, v. 63, p. 106-121.

Budden K.G. Radio waves in the ionosphere.- *Cambridge University Press*, 1961, p. 542.

Davies K. and Jones S.E. Three dimentional observation of travelling ionospheric disturbances.- *J. atmos. terr. Phys.*, 1971, v. 33, p. 39-47.

Devan E.M. On the nature of atmospheric waves and turbulence.- *Radio Sci.*, 1985, v. 20, p. 1301-1307.

Devan E.M. Similitude modelling of internal gravity wave spectra.- *Geoph. Res. Let.*, 1991, v. 18, p. 1473-1476.

Dong B. and Yeh K.C. Resonant and nonresonant wave-wave interraction in an isotermal atmosphere.- *J. Geophys. Res.*, 1988, v. 93, p. 3729-3744.

Frances S.H. A theory of medium-scale travelling ionospheric disturbances.- *J. Geophis. Res.*, 1974, v. 79, p. 5245-5259.

Hajkowicz L.A. Global onset and propagation of large-scale travelling ionospheric disturbances as a result of the great storm of 13 March 1989,- *Planet. Space Sci.*, 1991, v. 39, p. 583-593.

Hajkowicz L.A. Median ionospheric height variation over a sunspot cycle in the Australian-Japanese Longitudinal sector.- *Planet Space Sci.*, 1991, v. 39, No. 12, p. 1607-1615.

Hajkowicz L.A. and Hunsucker R.D. A simultaneous observation of large-scale periodic TID in both hemispheres following an onset of auroral disturbances.- *Planet. Space Sci.*, 1987, v. 35, p. 785-791.

Hedin A.E. et al. Empirical wind model for the upper, middle and lower atmosphere.- *J. Atmos. Terr. Phys.*, 1996, Vol. 58, No 13, p. 1421-1447.

Herron T.J. Phase veloscity dispersion of F-region waves.- *J. Atmos. Terr. Phys.*, 1973, v. 35, p. 101-124.

Hines C.O. Internal atmospheric gravity waves of ionospheric heights.- *Can. J. Phys.*, 1960, v. 38, p. 1441-1481.

Hocke K. Phase estimation with the Lomb-Scargle periodogram method.- *Ann. Geophys.*, 1998, Vol. 16, No. 3, p. 356-358.

Horne J.H. and Baliunas S.L. A prescription for period analysis of unevently sampled time series.- *Astrophys. J.*, 1986, Vol. 302, No. 2, Part 1, p. 757-763.

Jacobson A.R. and Carlos R.C. A study of apparent ionospheric motion associated with multiple travelling ionospheric disturbances. *J.Atmos. terr. Phys.*, 1991, v. 53, p. 53-62.

Jacobson A.R., Carlos R.C., Massey R.S. and Wu G. Observation of travelling inospheric disturbances with a satellite -beacon radio interferometer: Seasonal and Local time behavior.- *J. Geoph. Res.*, v. 100, p. 1653-1665.

Jenkis G.M. and Watts D.G. Spectral Analysis and Application, 1968, Holden-Day, San Francisco, p. 525.

Kaliev M.Z., Krasnikov I.M., Litvinov Yu.G., Chakenov B.D., Yakovets A.F. Temporal properties of travelling ionospheric disturbances.- *Geomagn. Aeron.*, 1989, No. 29, p. 776-781.

Kaliev M.Z., Krasnikov I.M, Litvinov Yu.G., Chakenov B.D., Yakovets A.F. A fine structure of a spectrum of middle-scale travelling ionospheric disturbances.- *Geomagn. Aeron.*, 1998, v. 28, p. 316-318.

Krassovsky V.I. Infrasonic variations of OH emission in the upper atmosphere.- *Ann. Geophys.*, 1972, Vol. 28, No. 4, p. 739-746.

Kelley M.C. and Fukao S. Turbulent upwelling of the mid-latitude ionosphere, 2,Teoretical framework.- *J. Geoph. Res.*, 1991, v. 96, p. 3747.

Lindzen R.S. Gravity waves in the mesosphere.- In "Dynamics of the Middle Atmosphere" (J.R.Holton and T.Matsuno, eds.), Terra Scientific Publishing Co., Tokyo, 1984, p. 3-18.

Lomb N.R. Least squares frequency analysis of unequally spaced data.- *Astrophys. Space Sci.*, 1976, Vol. 39, No. 2, p. 447-462.

Ma S.Y. and Schlegel K. Nonlinear wave-wave interaction related to gravity wave reflection in the auroral upper F-region observed with the EISCAT radar.- J. Atm. Terr. Phys., 1993, v. 55, p. 739-749.

Marple S.L. jr. Digital spectral analysis with applications. Prentice-Hall Inc., Englewood Cliffs, 1988, New Jersey, p. 582.

Montes H.A. and Posmentier E.S. Co-phase analysis of atmospheric wave data.- *Geophys. J. R. astr. Soc.*, 1971, Vol. 26, p. 271-278.

Miller K.L., Torr D.G. and Richards P.G. Meridinal winds in the thermosphere derived from measurement of F2 layer.*J. Geoph. Res.*, 1986, v. 91, p. 4531.

Muller P.,Holloway G., Heney F. and Pomphrey N. Nonlinear interactions among internal gravity waves.- *Rev. Geophys.*, 1986, v. 24, p. 495-536.

Nikias L. and Raghuveer M.R. Sispectrum estimation: A digital signal processing framework.- *Proc. IEEE*, 1987, v. 75, p. 5-30.

Ozonovich I., Walterscheid R.L., Sivjee G.G., and McEwen D.J. On Krassovsky's ratio for ter-diurnal hydroxyl oscillations in the winter polar mesopause.- *Planet. Space Sci.*, 1997, Vol. 45, No. 3, p. 385-394.

Perkins F., Spread F. and ionospheric currents.- *J. Geoph. Res.*, 1973, v. 73, p. 218.

Pogoreltsev A.I. and Pertsev N.N. The influence of background wind on the formation of the acoustic-gravity wave structure in the thermosphere.- *Izv. Russian Acad. Sci., Atmos. Oceanic Phys.*, 1995, Vol. 31, No 6, p. 755-760, in Russian (English Edition: *Izv. Russian Acad. Sci., Atmos. Oceanic Phys.*, 1996, Vol. 31, No 6, p. 723-728).

Posmentier E.S. and Herrman R.W. Cophase: An ad hoc array processor.- *J. Geophys. Res.*, 1971, Vol. 76, No. 9,p. 2194-2201.

Press W.H. and Teukolsky S.A. Search algorithm for weak periodic signals in unevently spaced data.-*Computers in Phys.*, 1988, Vol. 2, No. 6, p.77-82.

Scargle J.D. Studies in astronomical time series analysis. II. Statistical aspects of spectral analysis of unevently spaced data.- *Astrophys. J.*, 1982, Vol. 263, No. 2, Part 1, p. 835-853.

Shibata T. and Okuzawa T. Horizontal velocity dispersion of medium-scale travelling ionospheric disturbances in the F-region.- *J. Atmos. Terr. Phys.*, 1983, v. 45, p. 149-159.

Shibata T. and Schlepel K. Vertical structure of AGW associated ionospheric fluctuations in the E and lower F-region observed with EISCAT-a case study.- *J. Atmos. Terr. Phys*, 1993, v. 55, No. 4/5, p. 739-749.

Tsusui M., Horikawa T. and Ogawa T. Determination of velocity vectors of thermospheric wind from dispersion relations of TID's observed by an HF Doppler array.- *J.Atmos. Terr. Phys.*, 1984, v. 46, p. 447-462.

Turner J.S. Buoyancy effects in fluids. Cambridge at the University Press 1973, p. 431.

Waldock J.A. and Jones T.B. Source region of medium scale travelling ionospheric disturbances observed at mid-latitudes.- *J. Atmos. Terr. Phys.*, 1987, v. 49, p. 195-214.

Waters C.L., Menk F.W., Fraser B.J. and Ostwald P.M. Phase structure of low-latitude Pc 3-4 pulsations.- *Planet. Space Sci.*, 1991, p. 569-582.

Wiens R.H., Zhang S.-P., Peterson R.N., Shepherd G.G. MORTI: A Mesopause Oxigen Rotational Temperature Imager.- *Planet. Space Sci.*, 1991, Vol. 39, No. 10, p. 1363-1375.

Wiens R.H., Zhang S.P., Peterson R.N., and Shepherd G.G. Tides in emission rate and temperature from O_2 nightglow over Bear Lake Observatory.- *Geophys. Res. Lett.*, 1995, Vol. 22, No. 19, p. 2637-2640.

Yakovets A.F., Drobjev V.I. and Litvinov Yu.G. The spatial coherence of travelling ionospheric disturbances at mid-latitudes.- *J. Atmos. Terr. Phys.*, 1995, v. 57, p. 25-33.

Yeh K., Ma S.Y. and K.H.Lin. Global ionospheric effects of the October 1989 geomagnetic storm.- *J. Geoph. Res.*, 1994, v. 99, p. 6201-6218.

Zhang S.P., Peterson R.N., Wiens R.H., Shepherd G.G. Gravity waves from O_2 nightglow during the AIDA'89 compaign. I: emission rate/temperature observations.- *J. Atmos. Terr. Phys.*, 1993a, Vol. 55, No. 3, p. 355-375.

Zhang S.P., Wiens R.H., and Shepherd G.G. Gravity waves from O_2 nightglow during the AIDA'89 campaign II: numerical modeling of the emission rate/temperature ratio, η.- *J. Atmos. Terr. Phys.*, 1993b, Vol. 55, No. 3, p. 377-395.

III. Simulation of Planetary Waves and Their Influence on the Zonally Averaged Circulation in the Middle Atmosphere

Paper was presented by A.I.Pogoreltsev as an invited report at the International Symposium on Dynamics and Structure of the Mesopause Region (March 16-20, 1998, Kyoto, Japan) and will be submitted for publication in Special Issue of **Earth, Planets and Space** in June 1998.

3.1. Introduction.

Analysis of the results obtained by the Wind Imaging Interferometer (WINDII) and High Resolution Doppler Imager (HRDI) on the Upper Atmosphere Research Satellite (UARS) shows a presence of the strong large-scale variations of the emission rates and winds in the mesosphere and lower thermosphere (Shepherd et al., 1993; Smith, 1995), which were interpreted as manifestation of the planetary waves (PWs). Besides, the main purpose of the PSMOS project is the establishment of a ground-based mesopause observing system for the investigation of planetary scale disturbances, and the purpose of present report is to show some results of the simulation of PWs in the middle atmosphere and to discuss a possibility of the observation of these waves by satellite and ground-based equipment. The comparison of numerical results with the experimental data will be made and the contribution of PWs to the zonally averaged dynamics of mesopause region will be considered.

3.2. Model Formulation.

The initial set of the equations describing the disturbances and zonally averaged state can be written as follows (Boyd, 1976; Andrews, 1985)

$$(\bar{u}-c)u'_\lambda/(a\cos\varphi) - f_1 v' + \bar{u}_z w' + \phi'_\lambda/(a\cos\varphi) = X', \tag{1}$$

$$(\bar{u}-c)v'_\lambda/(a\cos\varphi) + f_2 u' + \phi'_\varphi/a = Y', \tag{2}$$

$$\phi'_z = R\theta'\exp(-\kappa z/H)/H, \tag{3}$$

$$u'_\lambda/(a\cos\varphi) + (\cos\varphi v')_\varphi/(a\cos\varphi) + (\rho_0 w')_z/\rho_0 = 0, \tag{4}$$

$$(\bar{u}-c)\theta'_\lambda/(a\cos\varphi) + \bar{\theta}_\varphi v'/a + \bar{\theta}_z w' = Q', \tag{5}$$

$$\bar{u}_t - f_1\bar{v}^* + \bar{u}_z\bar{w}^* = \bar{X} + \nabla\cdot\mathbf{F}/(\rho_0 a\cos\varphi), \tag{6}$$

$$(f + \bar{u}\tan\varphi/a)\bar{u} + \bar{\phi}_\varphi/a = \bar{G}, \tag{7}$$

$$\bar{\phi}_z = R\bar{\theta}\exp(-\kappa z/H)/H, \tag{8}$$

$$(\cos\varphi\bar{v}^*)_\varphi/(a\cos\varphi) + (\rho_0\bar{w}^*)_z/\rho_0 = 0, \tag{9}$$

$$\bar{\theta}_t + \bar{\theta}_\varphi\bar{v}^*/a + \bar{\theta}_z\bar{w}^* = \bar{Q} - (\rho_0\nabla\bar{\theta}\cdot\overline{\mathbf{v}'\theta'}/\bar{\theta}_z)_z/\rho_0. \tag{10}$$

Here λ is longitude, φ is latitude, $z = -H\ln(p/p_s)$ is the vertical coordinate, where p is pressure, $p_s = const$ is a standard reference pressure, $H = const$ is the scale height; u, v, and w are the corresponding velocities, ϕ denotes the geopotential, and θ the potential temperature; R is the gas constant for dry air, $\kappa = R/c_p$, c_p is the specific heat at constant pressure; X, Y are the unspecified horizontal components of friction or other nonconservative mechanical forcing, Q is the diabatic heating term; $\rho_0(z) = \rho_s \exp(-z/H)$ is a reference density profile, $\rho_s = const$; $f_1 = f + \bar{u}\tan\varphi/a - \bar{u}_\varphi/a$, $f_2 = f + 2\bar{u}\tan\varphi/a$, $f = 2\Omega\sin\varphi$ is the Coriolis parameter; Ω and a are the Earth's rotation rate and radius; $\mathbf{F} = (0,\ F^{(\varphi)},\ F^{(z)})$ is the EP flux vector, the components of which being given by the following relations

$$F^{(\varphi)} = \rho_0 a\cos\varphi(\bar{u}_z\ \overline{v'\theta'}\ /\bar{\theta}_z - \overline{u'v'}), \tag{11}$$

$$F^{(z)} = \rho a\cos\varphi(f_1\ \overline{v'\theta'}\ /\bar{\theta}_z - \overline{u'w'}), \tag{12}$$

$\bar{G}$ represents all the terms that lead to departures from the gradient wind balance between $\bar{\phi}_\varphi$ and $\bar{u}$; $\bar{v}^*$ and $\bar{w}^*$ define the residual meridional circulation velocities, which are related with Eulerian-mean ones as follows

$$\bar{v}^* = \bar{v} - (\rho_0\ \overline{v'\theta'}\ /\bar{\theta}_z)_z/\rho_0, \tag{13}$$

$$\bar{w}^* = \bar{w} + (\cos\varphi\ \overline{v'\theta'}\ /\bar{\theta}_z)_\varphi/(a\cos\varphi). \tag{14}$$

In equations (1)-(10) an overbar denotes the zonally averaged values, the disturbance is denoted by a prime; the subscripts λ, φ, z, t denote corresponding derivatives.
We assume the disturbances in equations (1)-(10) to be a sum of zonal harmonics , i.e., $q'(\lambda,\varphi,z,t) = Re\sum_m q'_m(\varphi,z)\exp[i(m\lambda - \omega t)]$, where q'_m is the complex amplitude and m is the zonal wavenumber. It is necessary to note that equations (1)-(5) are the linearized set of equations for disturbances, and that they apply for a single zonal harmonic with phase speed c.
The formulation of the boundary-value problem for simulation the latitude height structure of the planetary scale disturbances and the numerical method of the solution were described in the paper Pogoreltsev and Sukhanova (1993), and here we will only present and discuss the results of the simulations with this model. However, it is necessary to note here that the simplification of the initial set of equations for disturbances based on the scale analysis [by assuming a large Richardson and a small Rossby numbers (Pogoreltsev and Sukhanova, 1993)] are not justified in the case of inertia-gravity PWs [for instance, 2- and 5-day travelling PW], and in present paper we will consider the solution of exact primitive set of equations (10-(5).

3.3. The Background State.

The numerical simulations of the global structure of planetary waves were carried out for the climatic conditions of the Northern Hemisphere winter. The background temperature was taken from the MSIS-90 model (Hedin, 1991). The vertical profile of $T_0(z)$ is shown in Fig. 1.

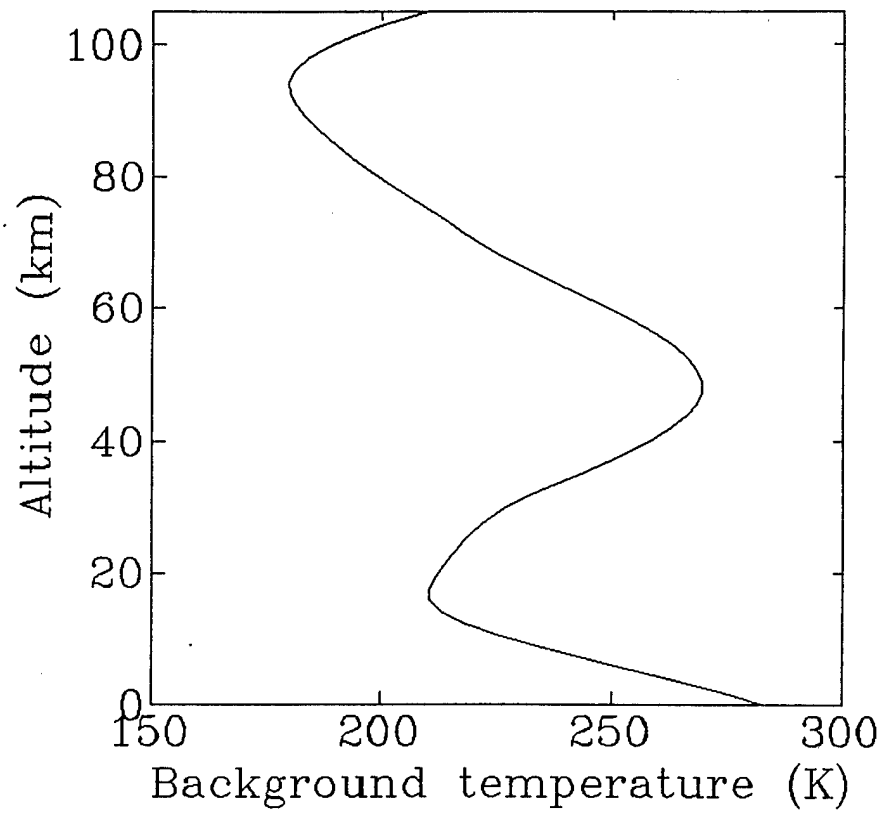

Figure 1: The vertical profile of the background temperature.

The simulations that we discuss were performed for the atmosphere with scale height H=7 km using the vertical step $\Delta z = H/4$.

We used two models of the background wind for January conditions

I. HWM-93 model (Hedin et al., 1996);

II. In altitude region between 90 and 120 km we used an empirical model of zonal wind based on the WINDII data (Wang et al., 1997).

The background wind distributions in the HWM-93 and WINDII models are shown in Fig. 2,3. One can see that in these models the westerlies over equator in the mesosphere are absent. However, the direct measurements by the HRDI for January 1992 through June 1993 show the westerlies over equator up to the 90 km in winter (Lieberman et al., 1993). To investigate the effect of the mesospheric westerlies over equator on the propagation of the PWs, we used the MODIFIED WINDII model, which was defined as follows

$$\bar{u} = \bar{u}(\mathrm{WINDII}) + 30\exp[-(\frac{z-75}{15})^2]\exp[-(\frac{\varphi}{30})^2]. \tag{15}$$

The distribution of the background wind for the MODIFIED WINDII model is shown in Fig. 4.

3.4. Dissipation Parameters.

The dissipative processes were parameterized in the form of Rayleigh friction and Newtonian cooling with coefficients $\beta_R(z,\varphi)$ and $\alpha_N(z)$. To avoid the numerical instability of the solution near the critical surfaces, we introduce a localized effective Rayleigh friction coefficient in these regions

$$\beta_R(z,\varphi) = \beta_{R0} + (m\beta_{Rm} - \beta_{R0})\exp[-(\frac{\bar{u}-c}{a\cos\varphi\beta_{Rm}})^2], \tag{16}$$

where $\beta_{R0} = 10^{-6}\mathrm{s}^{-1}$, $\beta_{Rm} = 3\cdot 10^{-6}\mathrm{s}^{-1}$. For Newtonian cooling we used the parameterization of damping rate in the cool-to-space limit given by Zhu (1993). Above 120 km the infrared radiation resulting from 5.3 μm nitric oxide band plays the main role in the lower thermosphere heat balance, and we used the formula given by Koskarts (1980) to calculate the damping rate in the thermosphere. The resulting Newtonian cooling coefficient is presented in Fig. 5.

3.5. Boundary Conditions.

The amplitudes and phases of geopotential height perturbations in stationary PW with m=1 at the level 18.55 mb (z=28 km) taken for January from CIRA-86 climatic model (Barnett and Corney, 1985) were set as a low boundary condition. The perturbation of the geopotential at the upper boundary which is set at 140 km was taken to be equal zero.

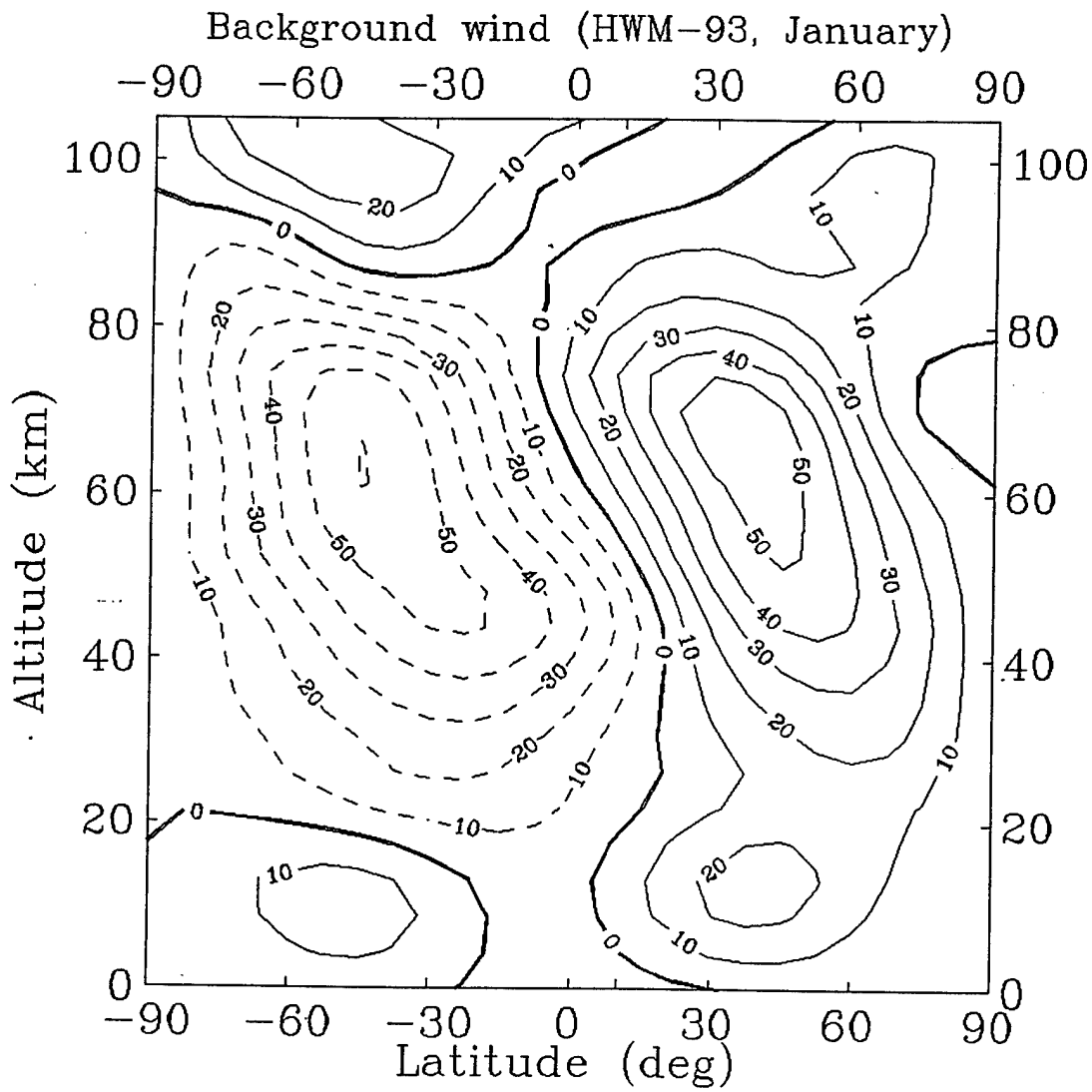

Figure 2: Meridional contours of background zonal wind (m/s) for HWM-93 model, solid – westerlies, dashed – easterlies. January conditions.

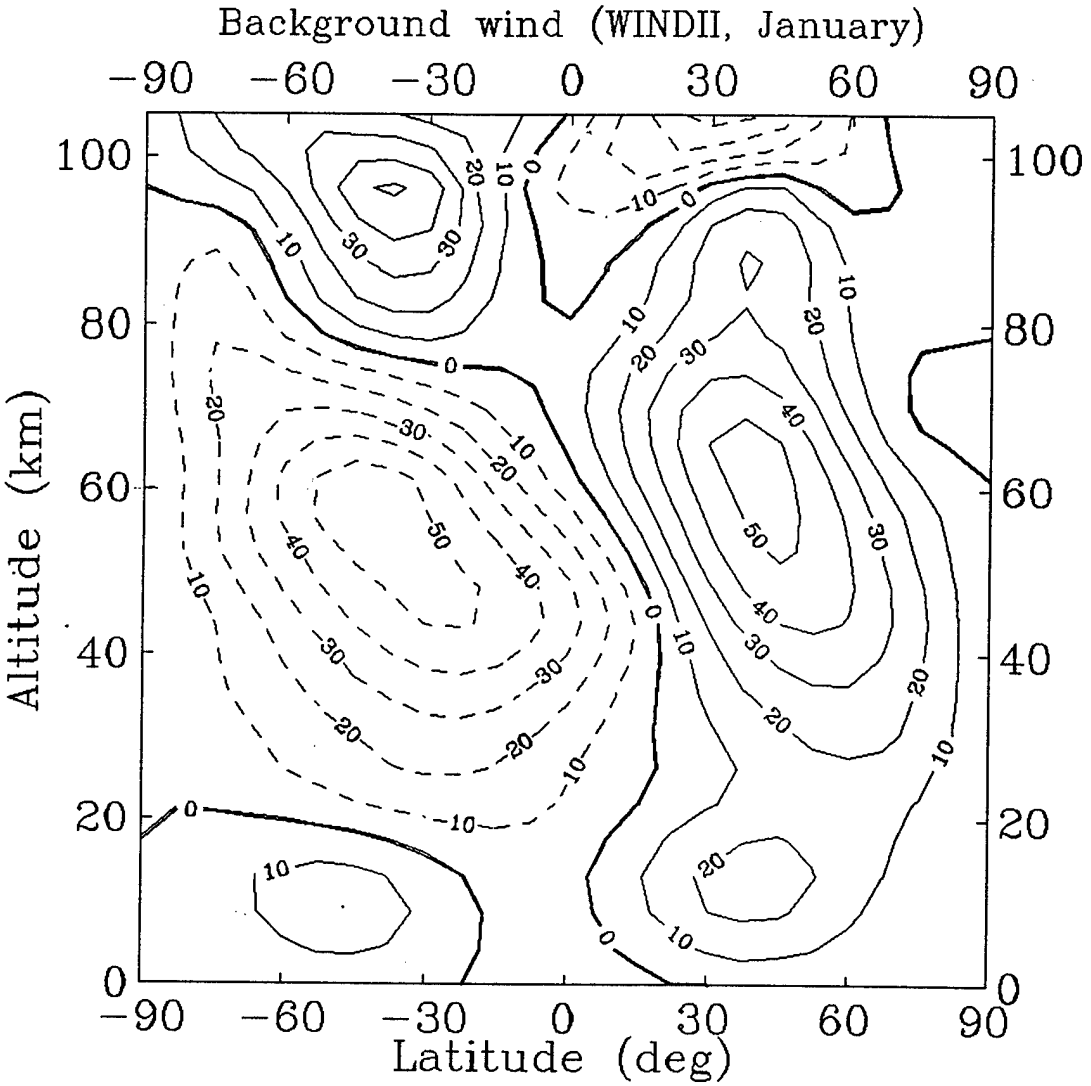

Figure 3: As in Fig. 2, but for WINDII model.

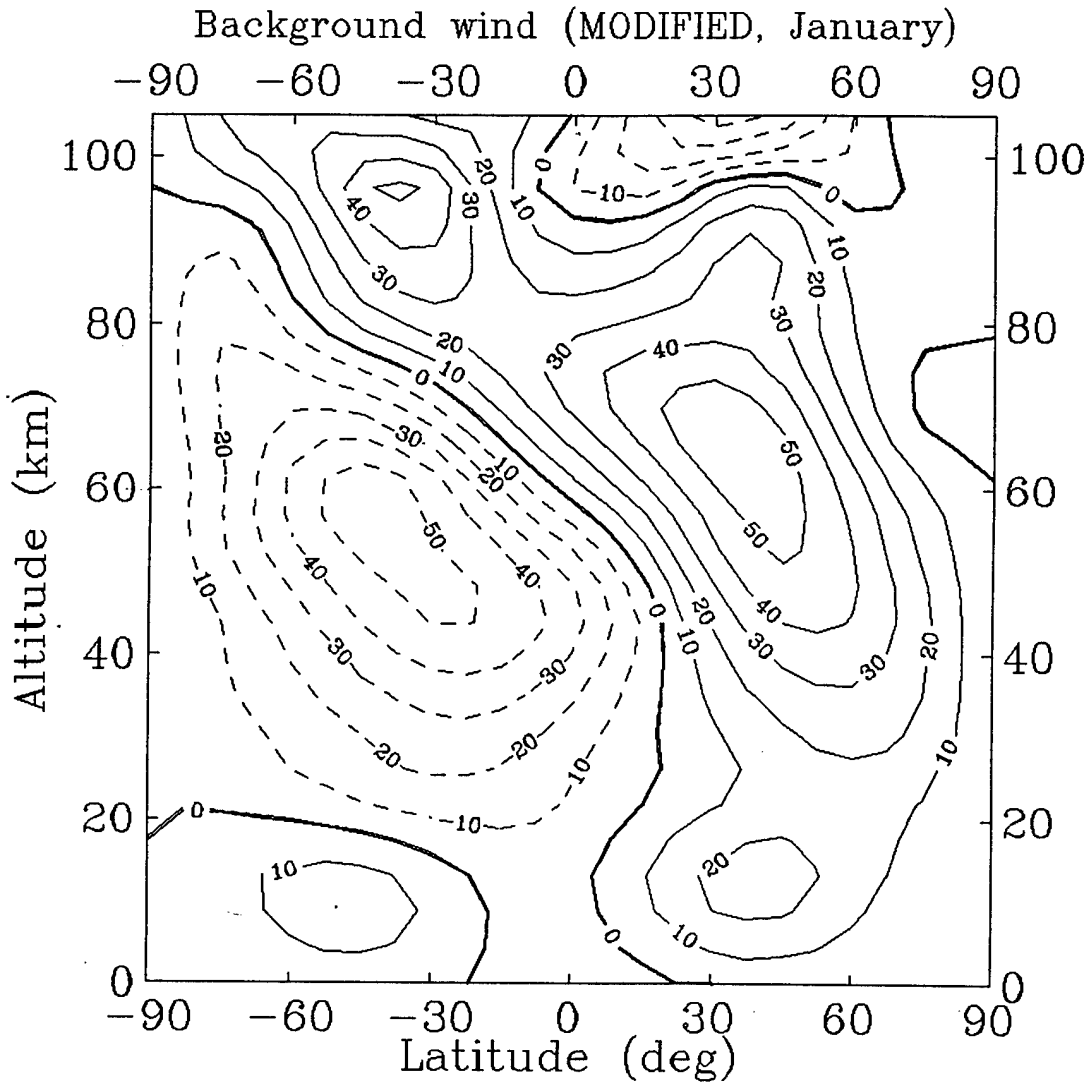

Figure 4: As in Fig. 2, but for MODIFIED model.

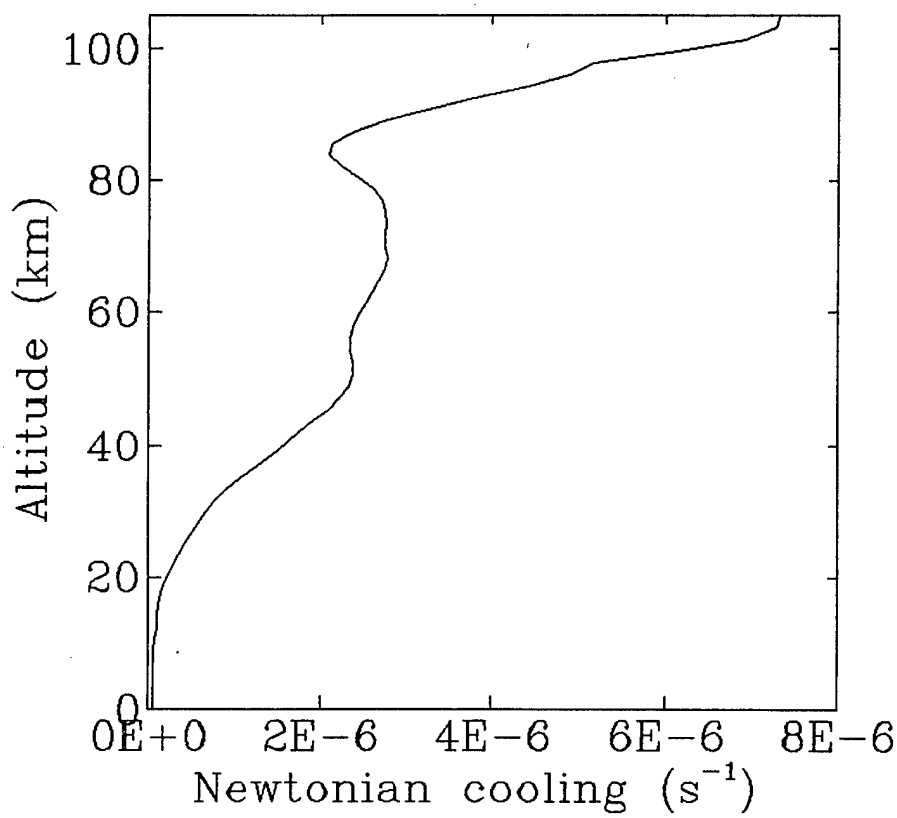

Figure 5: The vertical profile of the radiative damping rate.

3.6. The Influence of Background Wind Distribution on SPW.

The results of simulation of the stationary planetary wave (SPW) with zonal wave number m=1 in a form of isolines of amplitude of the geopotential height perturbation are shown in Fig. 6-8 for HWM-93, WINDII, and MODIFIED models of the background wind. One can see that in the cases of the HWM-93 and WINDII models SPW propagates mainly into the high latitude region of the Northern Hemisphere and then dissipates at the heights of the lower thermosphere (see Fig. 6,7). In the case of MODIFIED model there is a penetration of SPW into the Southern Hemisphere across the equator through the mesospheric westerlies. In result the amplitudes of the geopotential height perturbations in the SPW with m=1 are comparable in the lower thermosphere of the winter and summer Hemispheres.

3.7. Comparison of Computations and Observations.

The vertical structure of the geopotential height perturbation in SPW with m=1 at the latitude 60^0N is shown in Fig. 9. Dotted lines show the vertical profiles of the amplitude and phase taken from empirical model of SPW (Barnett and Cornney, 1985). The comparison of the results of simulation (solid lines) with observations shows good agreement.

The latitudinal dependencies of the amplitude and phase of the meridional wind perturbation in SPW with zonal wave number m=1 at the altitude z=90 km are shown in Fig. 10. Dotted lines show the results obtained from WINDII data averaged over period 1992-1996 (Wang D.Y., private communication). Solid lines show the results of simulation with the MODIFIED background wind model. One can see that the latitudinal structure of the amplitude does not show good agreement between WINDII observations and solution. Perhaps the reason for this discrepancy is the strong latitudinal smoothing of the background wind due to including only limited set of the vector spherical harmonics in the analytical empirical horizontal wind models (Hedin et al., 1991; Wang et al., 1997). However, the latitudinal structure of the phase show good agreement between WINDII observations and solution. It is necessary to note that westward slope of the phase, when we move from the Northern to Southern Hemisphere, indicates the cross equatorial SPW propagation, and this result supports our assumption that in winter there are the westerlies over the equator in the mesosphere.

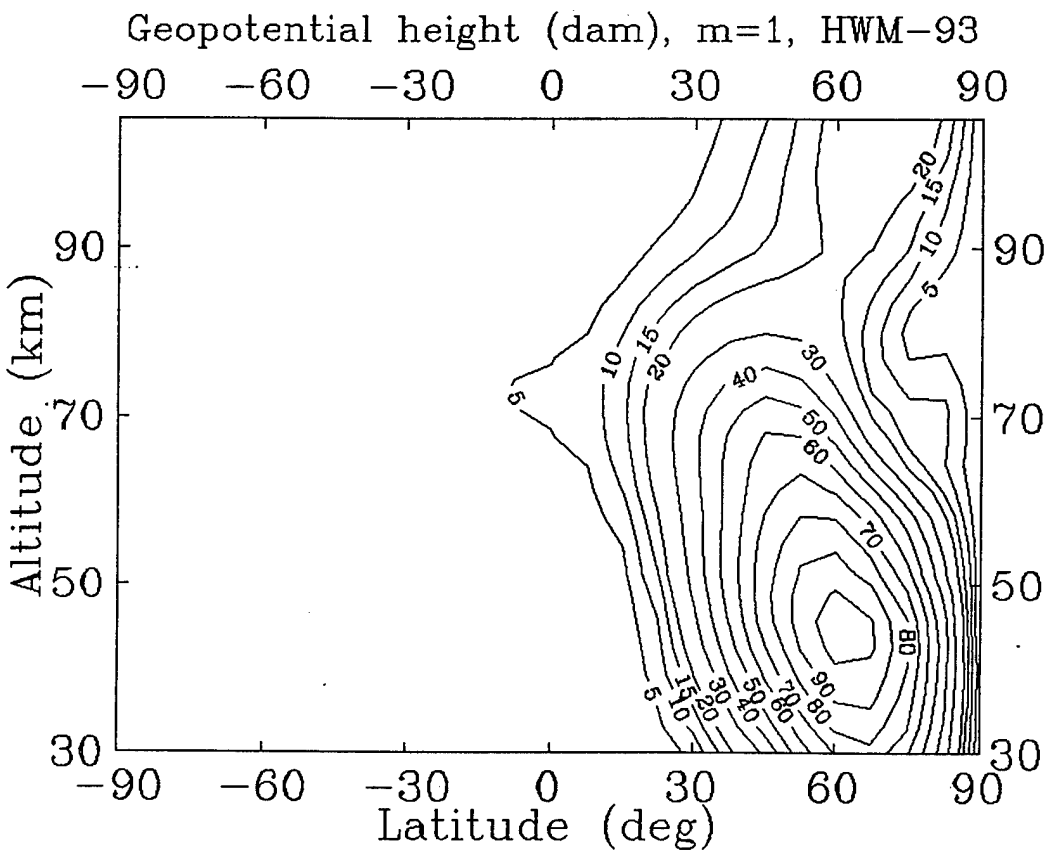

Figure 6: Latitude-height section of amplitude (dam) for the perturbation of the geopotential height in SPW with m=1 and background wind from HWM-93 model.

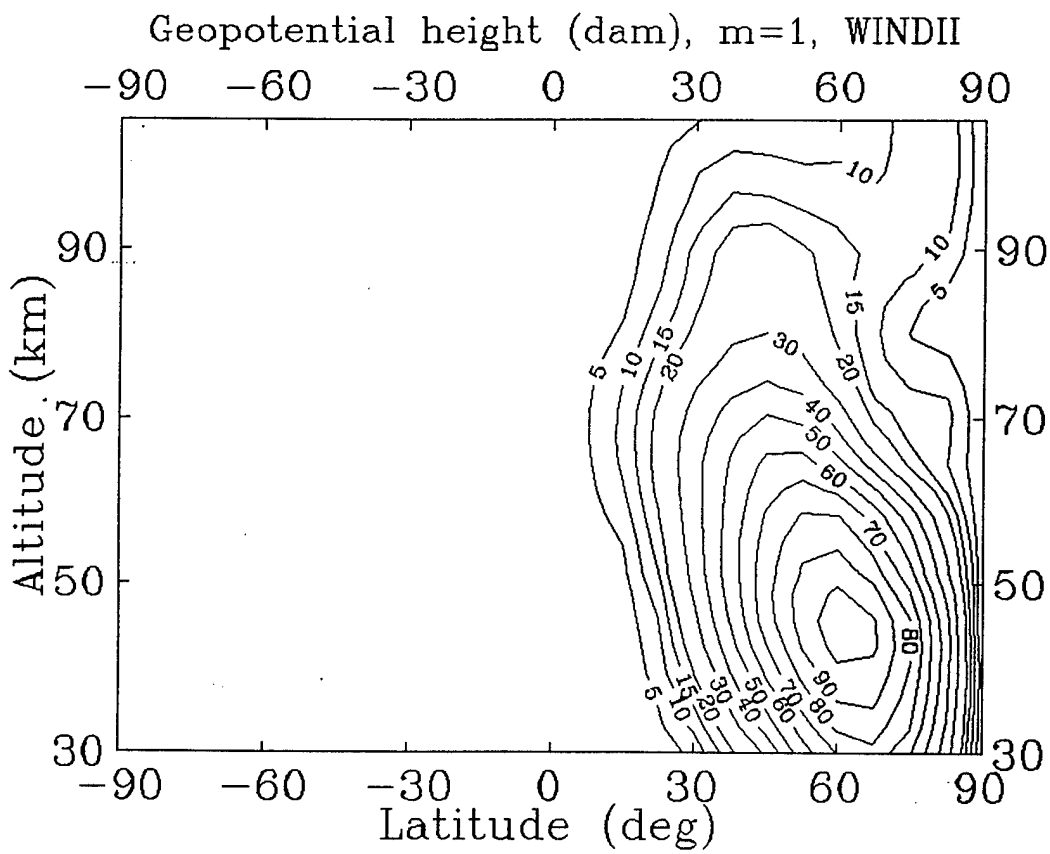

Figure 7: As in Fig. 6, but for WINDII model.

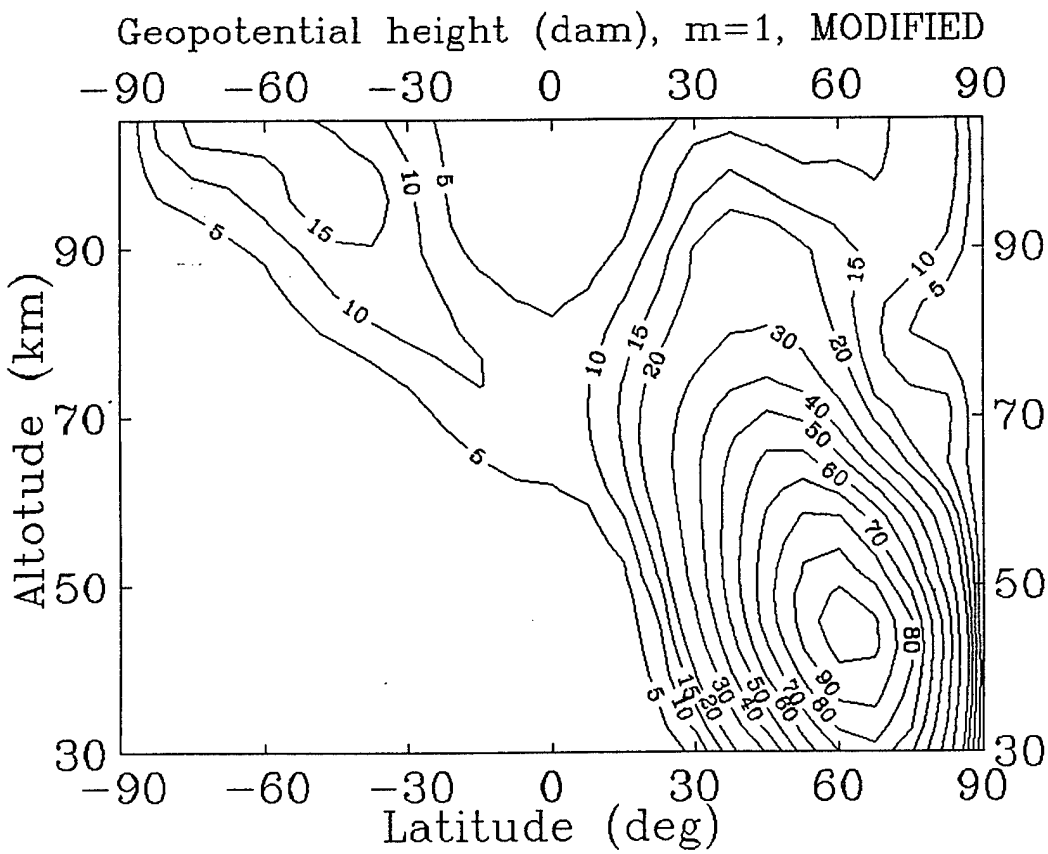

Figure 8: As in Fig. 6, but for MODIFIED model.

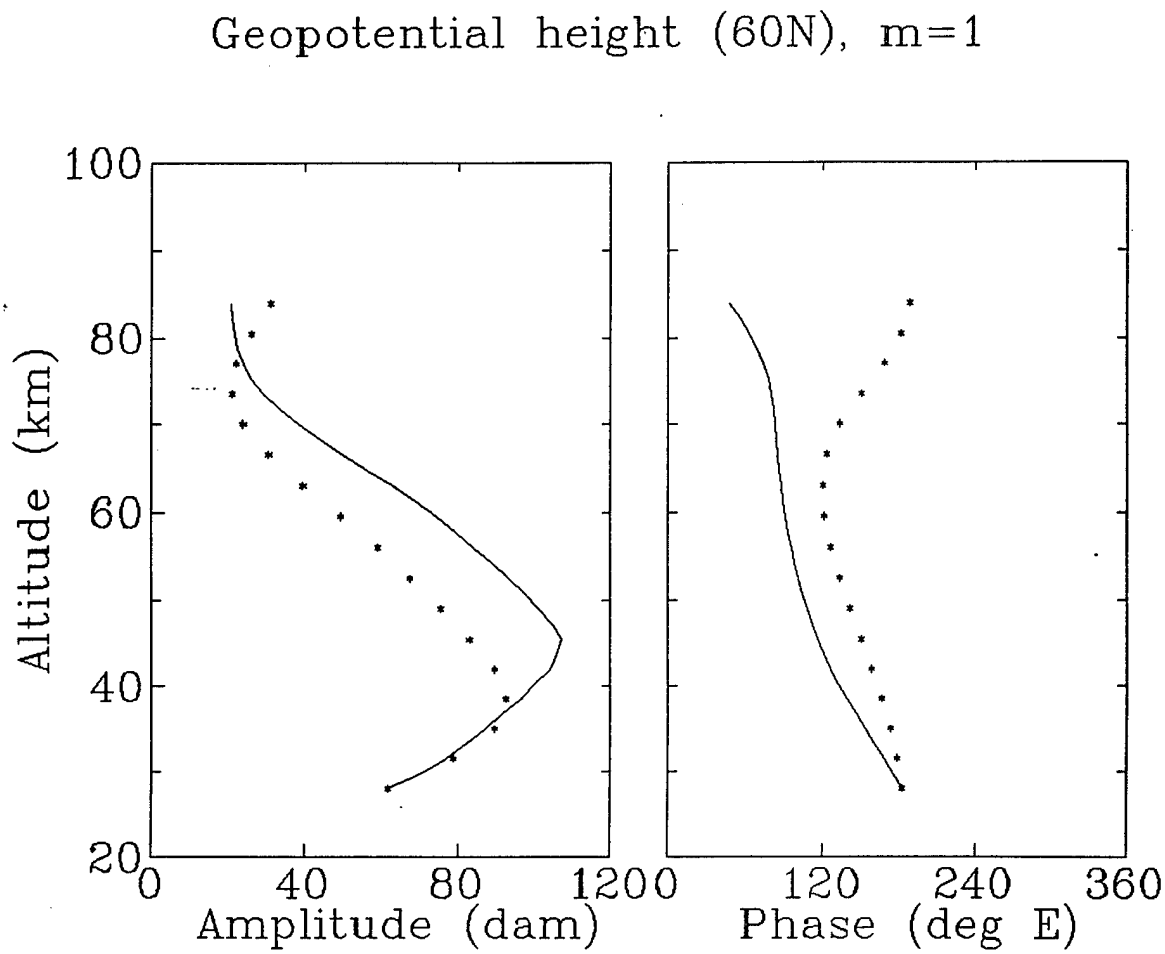

Figure 9: The vertical profiles of the amplitude and phase (the position of ridges) of the geopotential height perturbation in SPW with m=1 at the latitude 60^0N. Dotted lines show the results from empirical model CIRA-85.

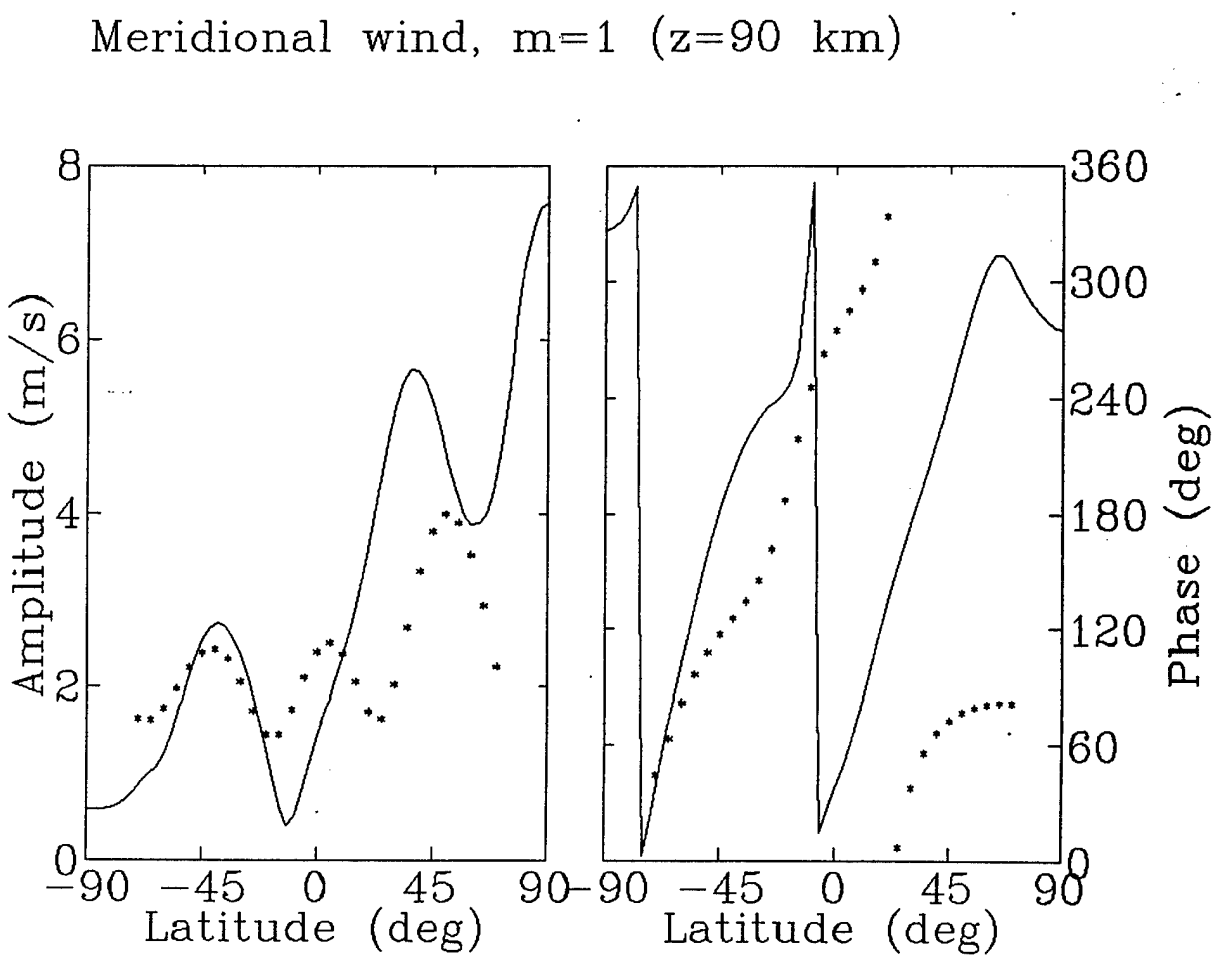

Figure 10: Latitudinal dependencies of the amplitude and phase of the meridional wind perturbation in SPW with m=1 at the altitude z=90 km. Dotted lines show the results obtained from WINDII data averaged over period 1992-1996 (Wang D.Y., private communication).

3.8. Responses of the Atmosphere to Lower Boundary Forcing.

The model of the global structure of SPW (Pogorltsev and Sukhanova, 1993) was modified to simulate the spectral atmospheric response to the symmetric and asymmetric forcing by the perturbation of the vertical velocity at the lower boundary. This problem is similar to the problem which was considered by Schoeberl and Clark (1980). However, there are some reasons to reconsider this question once more. Schoeberl and Clark (1980) used the quasi-geostrophic vorticity equation for the simulation of the structure of PW. Kirushov (1988) investigated the eigenvalues and eigenfunctions of the latitudinal structure operator of PW under quasi-geostrophic approximation, and it has been shown that the spectrum becomes quasi-confluent and symmetric modes coincide with asymmetric ones with the exception of the sign in another Hemisphere when the Rayleigh friction coefficient tends to zero. In other words, we have the complete set of the eigenfunctions in each Hemisphere separately, and the Northern and Southern Hemispheres do not interact in this case. In result low frequency responses of the atmosphere to the symmetric and asymmetric forcing are very similar (see Fig. 2 in Schoeberl and Clark, 1980). In the case of primitive set of equations the responses become noticeably different. This problem was investigated by Salby (1981), and it has been shown that the background wind shears cause the spectral broadening and shifting of the resonant responses. However, it seems that strong spectral broadening obtained by Salby (1981) is the consequence of the low latitudinal resolution and small dissipation. Lindzen and Blake (1972) showed that realistic dissipation mechanisms suppress the atmospheric response, and that the effect increases with the period of the wave.

To investigate the sensitivity of the atmospheric response to lower boundary forcing we specified the following boundary conditions. For the symmetric forcing we used $\tilde{w}^*(z=0) = \tilde{w}_0^* \cos 2\vartheta$, and for asymmetric forcing we used $\tilde{w}^*(z=0) = \tilde{w}_0^* \cos\vartheta$, where $\tilde{w}^* = w^* 2\Omega a/gH \cos^m \varphi$, $w^* = w' - \frac{i\omega}{g}\Phi'$ is the analog of the vertical velocity in the geometric coordinates, $\vartheta = \pi/2 - \varphi$ is co-latitude, and $\tilde{w}_0 = 10^{-5}$. It is necessary to note here that all calculations connected with traveling PWs were made with the HWM-93 model of the background wind for January conditions.

The amplitude response of the model to the lower boundary forcing for westward PWs with m=1 as function of the period are shown in Fig. 11. Here we define the response as follows

$$\text{Response} = \frac{1}{N}\sum_{i,j}^{\text{All}} |\Phi'_{ij}| \exp(-z_i/2H), \tag{17}$$

where N is a number of grid points. One can see from this figure that there are well defined resonant responses at the periods about 5 and 16 days for symmetric, and at the period about 10 days for asymmetric forcing. The latitudinal structures of the geopotential height perturbations in the 10 and 16 days PWs at the altitude z=7 km are shown in Fig. 12. This figure shows that these waves can be identified with first asymmetric (1,2) and second symmetric

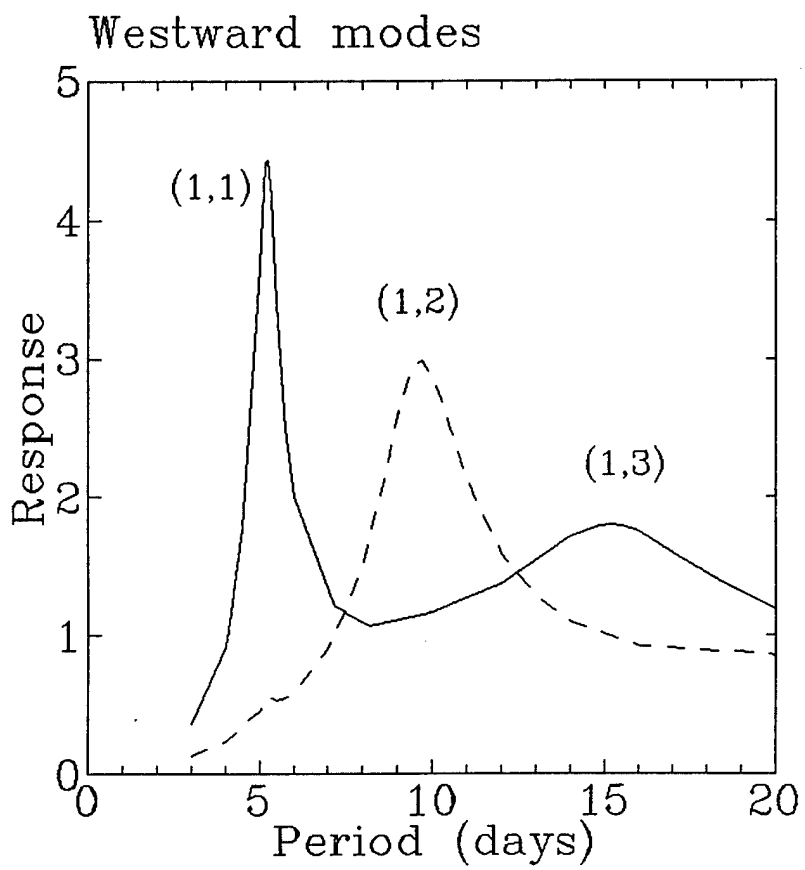

Figure 11: Response to the symmetric (solid) and asymmetric (dashed) forcing for the westward PWs with m=1.

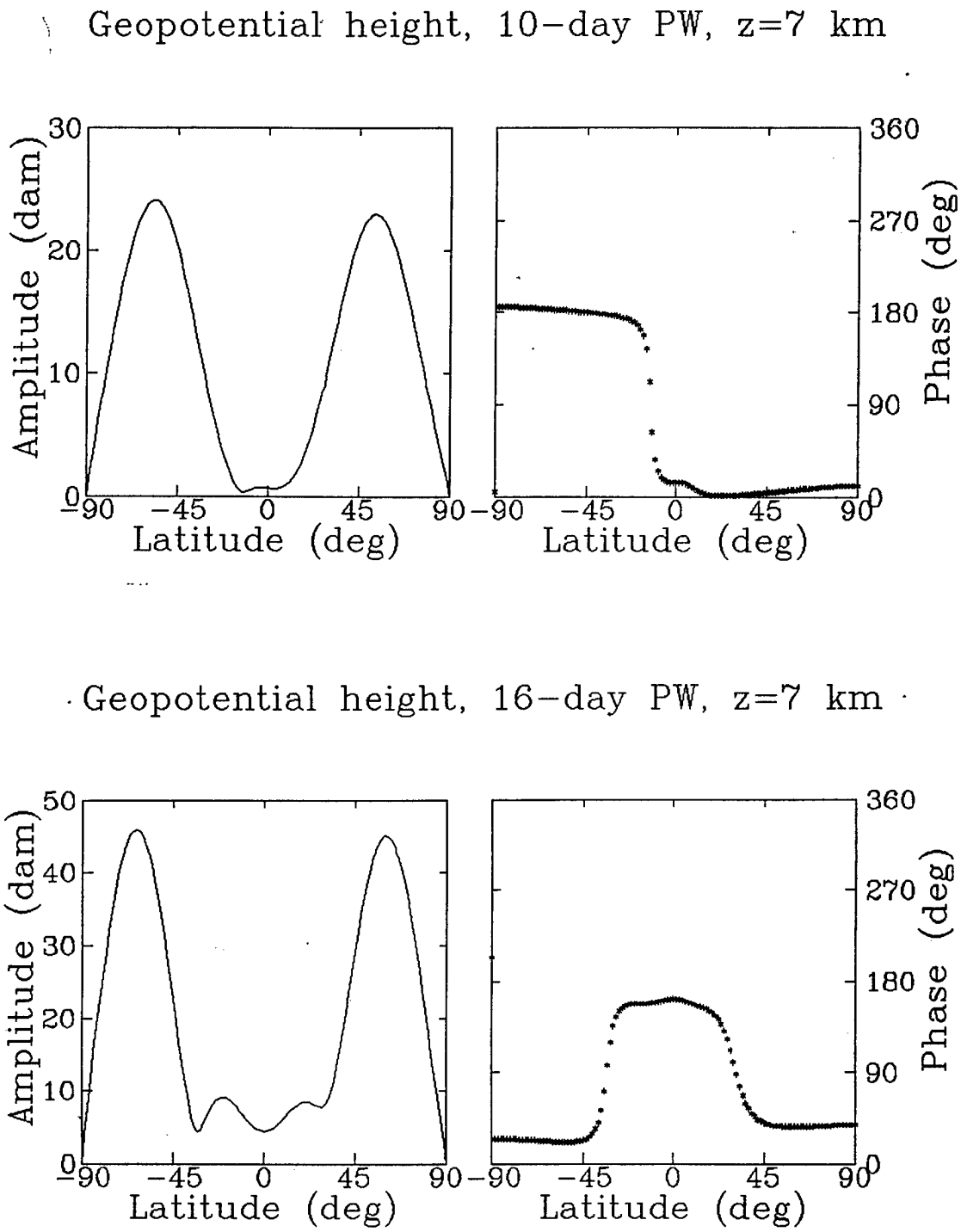

Figure 12: The latitudinal structure of the geopotential height perturbations in the 10- and 16-days PWs at altitude 7 km.

(1,3) normal atmospheric modes in the nomenclature of Longuet-Higgins (1968). By analogy the 5-days PW can be identified with first symmetric mode (1,1). The amplitude response of the model to the lower boundary forcing for the westward PW with m=2 is shown in Fig. 13. It is easy to identify the maxima in this figure with first symmetric (2,1) and first asymmetric (2,2) normal modes with the periods about 4 and 7 days, respectively. The second symmetric mode for PW with m=2 does not develop due to strong dissipation.

To reproduce the realistic conditions, we calibrate the solution in our model using the measured geopotential height amplitude of 16-days PW in stratosphere averaged over January 10-22, 1979 – the maximum is about 100 dam (Smith, 1985). The latitude-altitude structure of the geopotential height amplitude for 16-days PW is shown in Fig. 14. One can see that this wave propagates from winter stratosphere into the summer lower thermosphere across the equator. We calibrate 10 days PW solution by similar way, assuming that in the mesopause region this wave has the amplitude comparable with the amplitude of 16-days PW, and the latutude-altitude structure of 10-days PW is shown in Fig. 15. The latitudinal structures of the geopotential height perturbations in 10 and 16 days PWs at the altitude z=96 km are shown in Fig. 16. One can see from this figure that the latitudinal changes in these waves are very similar, and there are westward slopes of phases from Northern to Southern Hemisphere for both of waves. These slopes indicate the propagation of PW from winter into summer Hemisphere across the equator. We cannot identify 10 and 16 days PWs in the mesopause region with the normal atmospheric modes as, for instance, in the troposphere (see Fig. 12), and it is possible to make a conclusion that the latitudinal structure of these waves in the middle and upper atmosphere depends mainly on the distribution of the background wind, and does not depend on the latitudinal structure of the lower boundary source. The structures of the amplitude of zonal wind, meridional wind, and temperature perturbations due to 16 days PW are shown in Fig. 17-19. These figures show that there exist substantial ($\pm$15 m/s) variations of the zonal wind in the mesopause region conditioned by 16 days wave. The variations of the meridional wind are smaller by a factor of 2. The variations of the temperature at the middle latitudes of both Hemispheres can reach $\pm$ 5 K.

The response of the model to asymmetric forcing for westward PWs with m=3 is shown in Fig. 20. The maximum in this figure is situated at the period 52.5 hours, and this PW can be identified with well known third Rossby-gravity normal atmospheric mode (3,0), the so-called 2-days wave. To reproduce the realistic conditions, we calibrate the solution using the observed by WINDII during January 1993 magnitudes of the horizontal wind variations due to 2 days wave (Ward et al., 1996). The latitudinal structures of the amplitude of zonal and meridional wind perturbations in 2 days PW at the altitude z= 96 km are shown in Fig. 21,22. Dashed lines show the results obtained from the analysis of WINDII data, solid lines show the numerical solution. One can see that latitudinal structure of the amplitude of the zonal wind does not show good agreement between WINDII results and solution. The latitudinal structure of the PW, and especially the perturbation of the zonal wind, is strongly sensitive to the latitudinal changes in the background wind, and one of the possible reasons of the discrepancy between

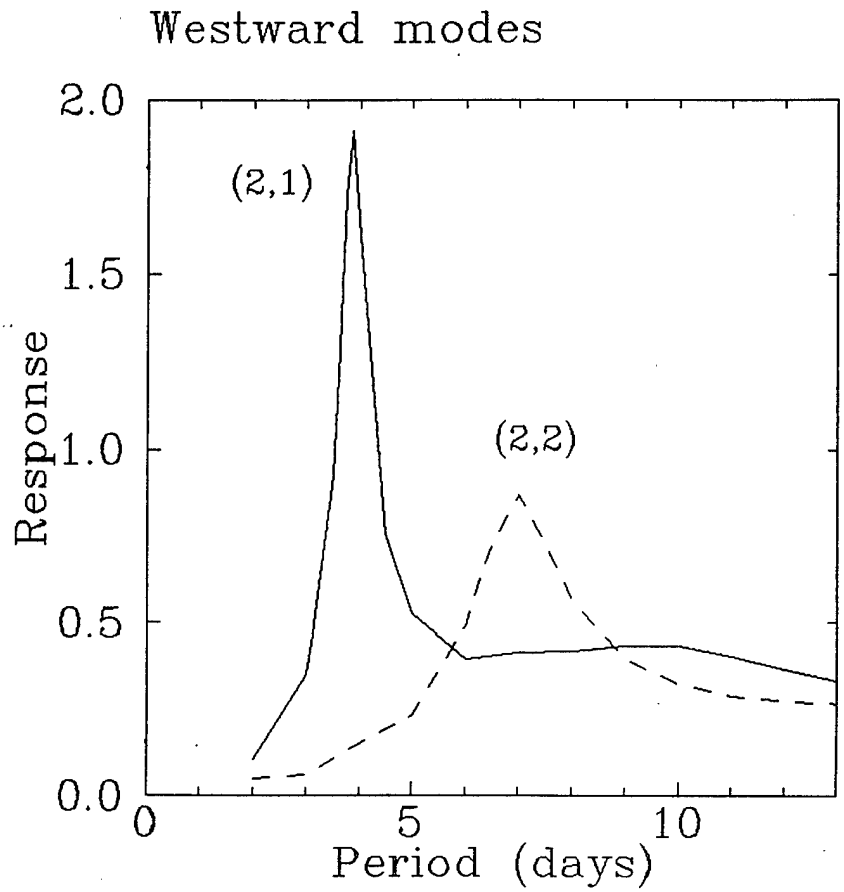

Figure 13: Response to the symmetric (solid) and asymmetric (dashed) forcing for the westward PWs with m=2.

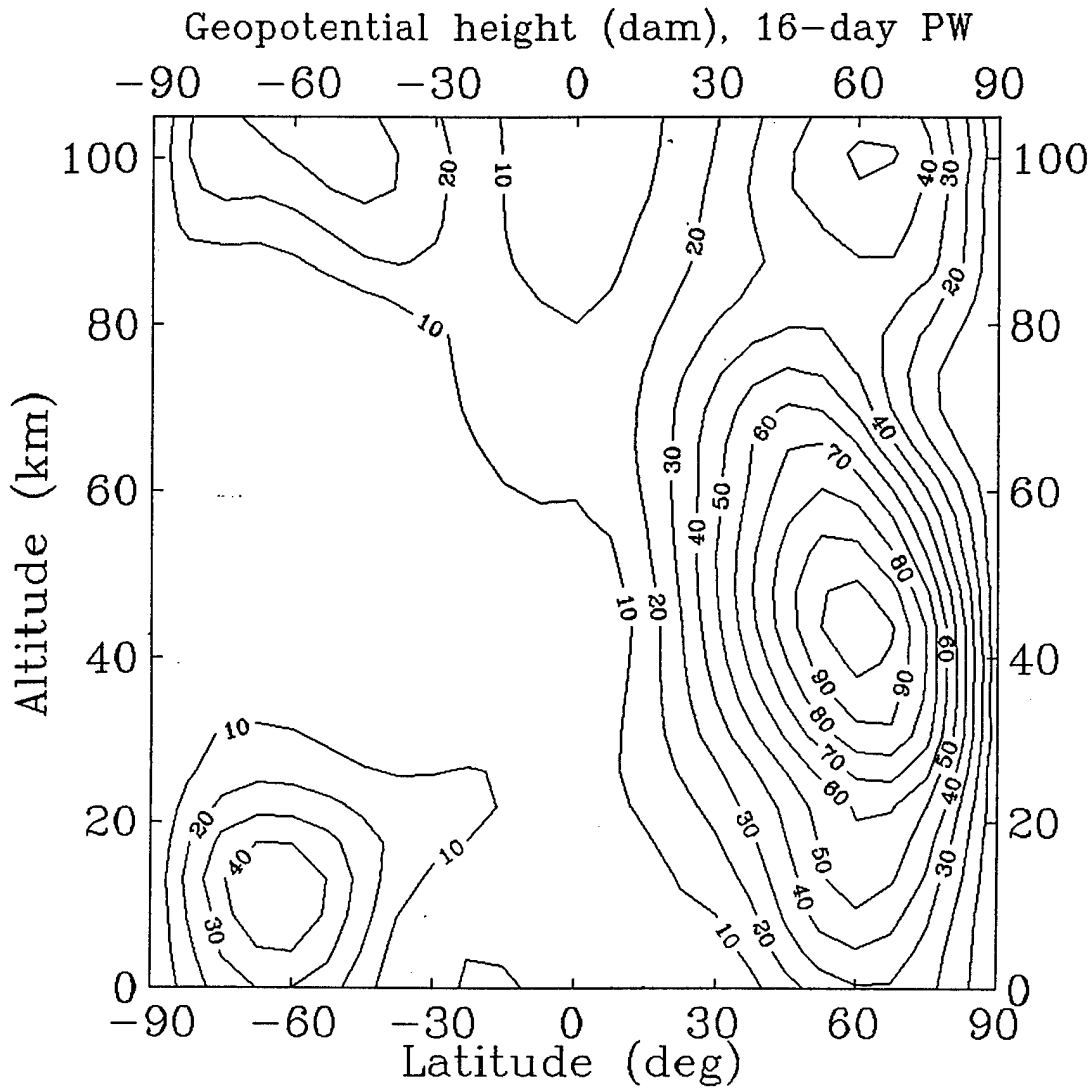

Figure 14: Latitude-height section of amplitude (dam) for the perturbation of the geopotential height in 16-days PW.

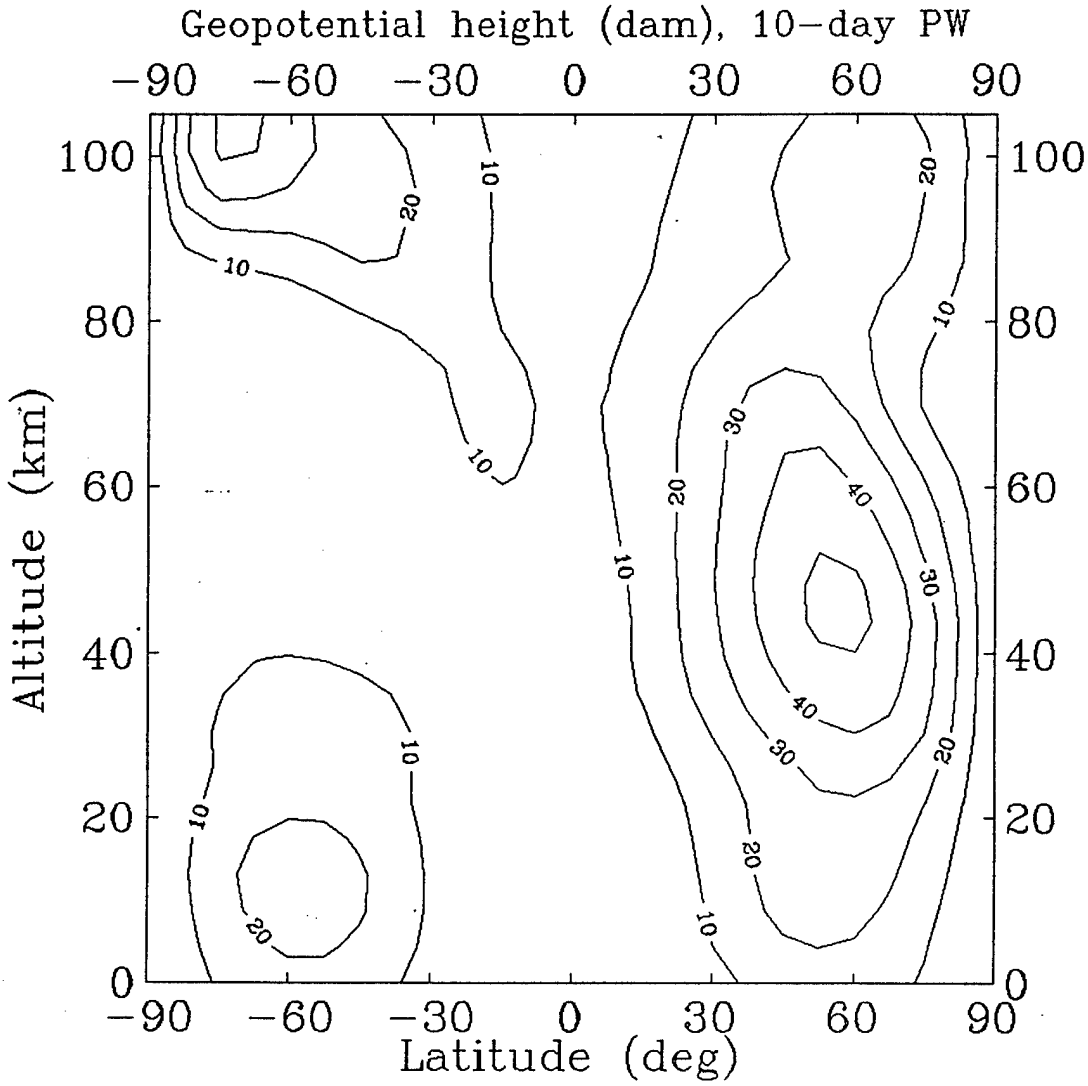

Figure 15: As in Fig. 14, but for 10-days PW.

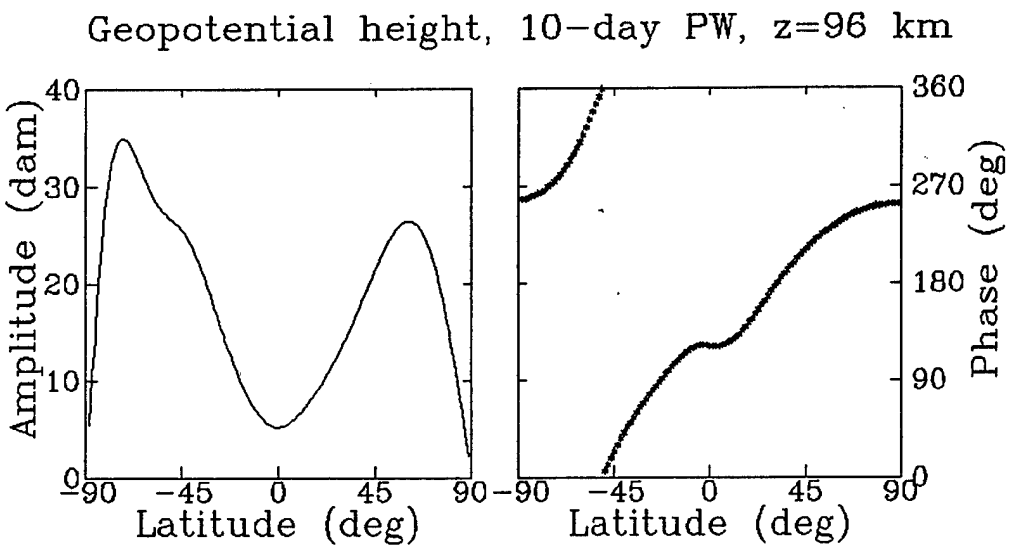

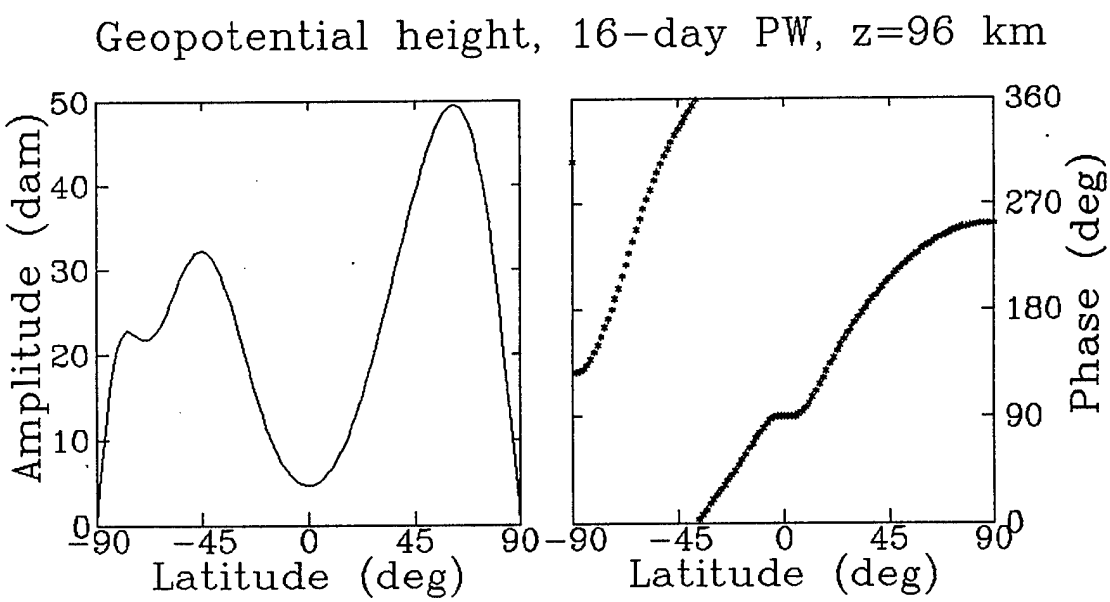

Figure 16: The latitudinal structure of the geopotential height perturbations in the 10- and 16-days PWs at altitude 96 km.

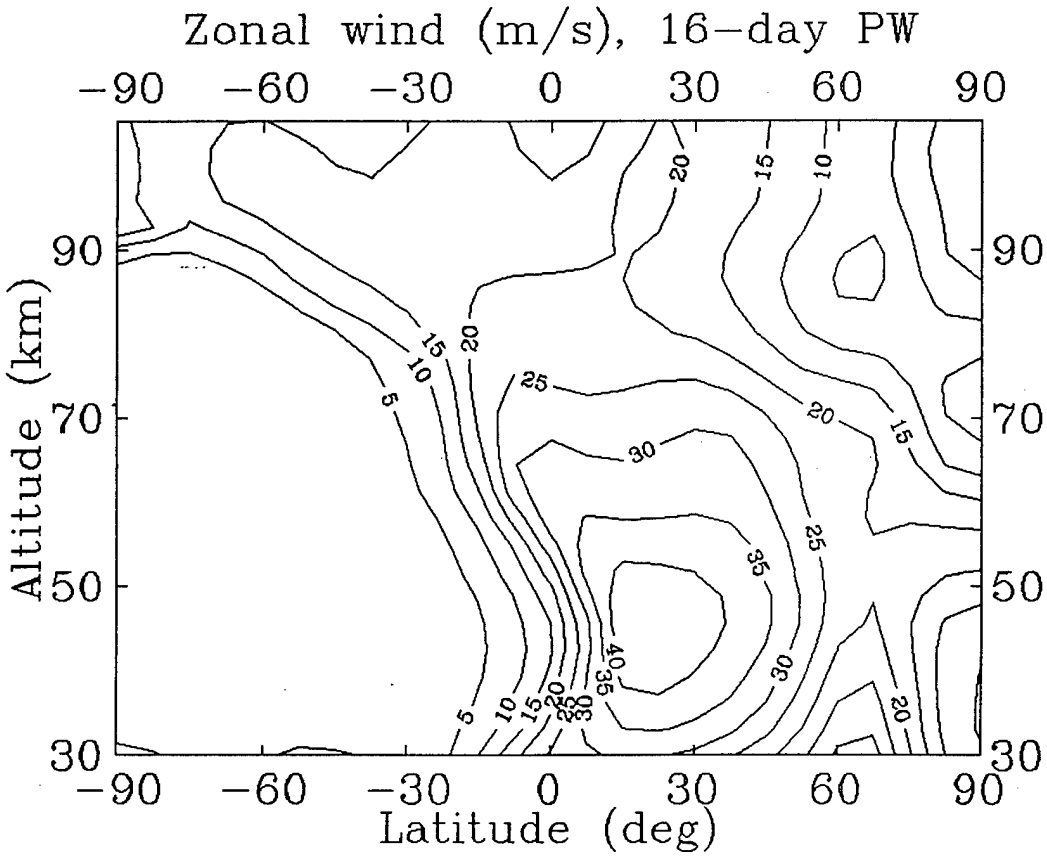

Figure 17: Latitude-height section of amplitude (m/s) for the perturbation of zonal wind in 16-days PW.

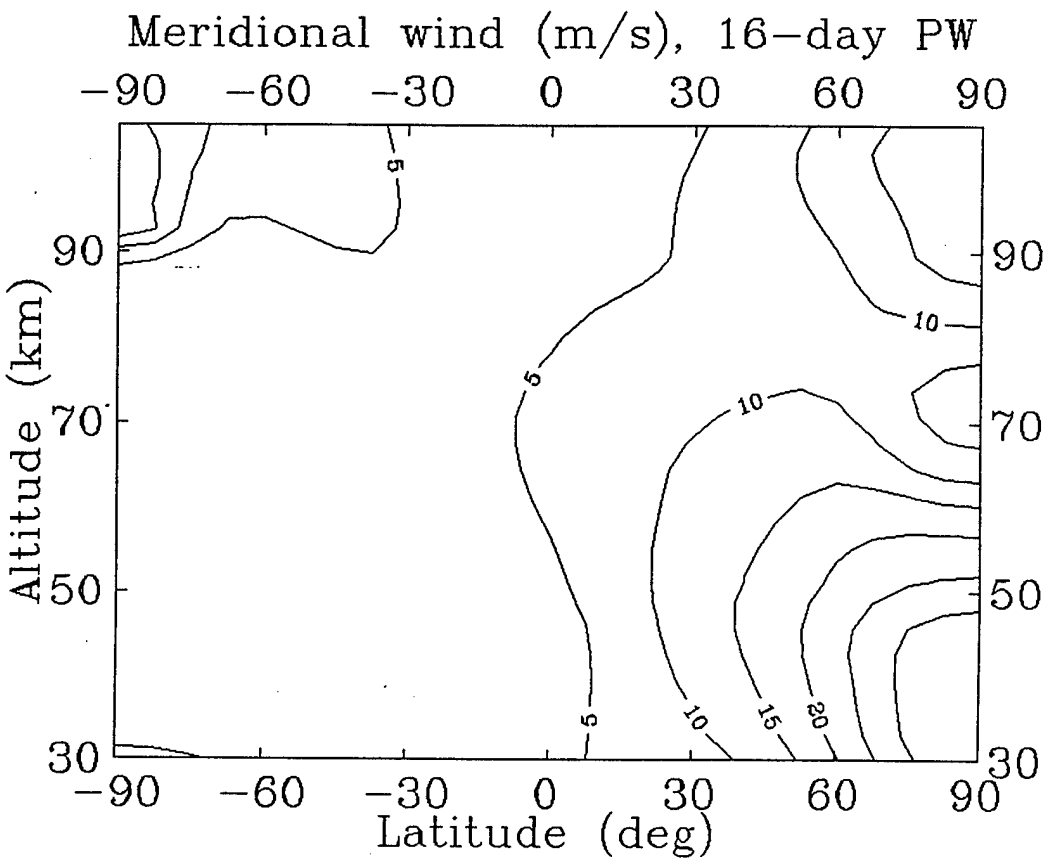

Figure 18: As in Fig. 17, but for the perturbation of meridional wind.

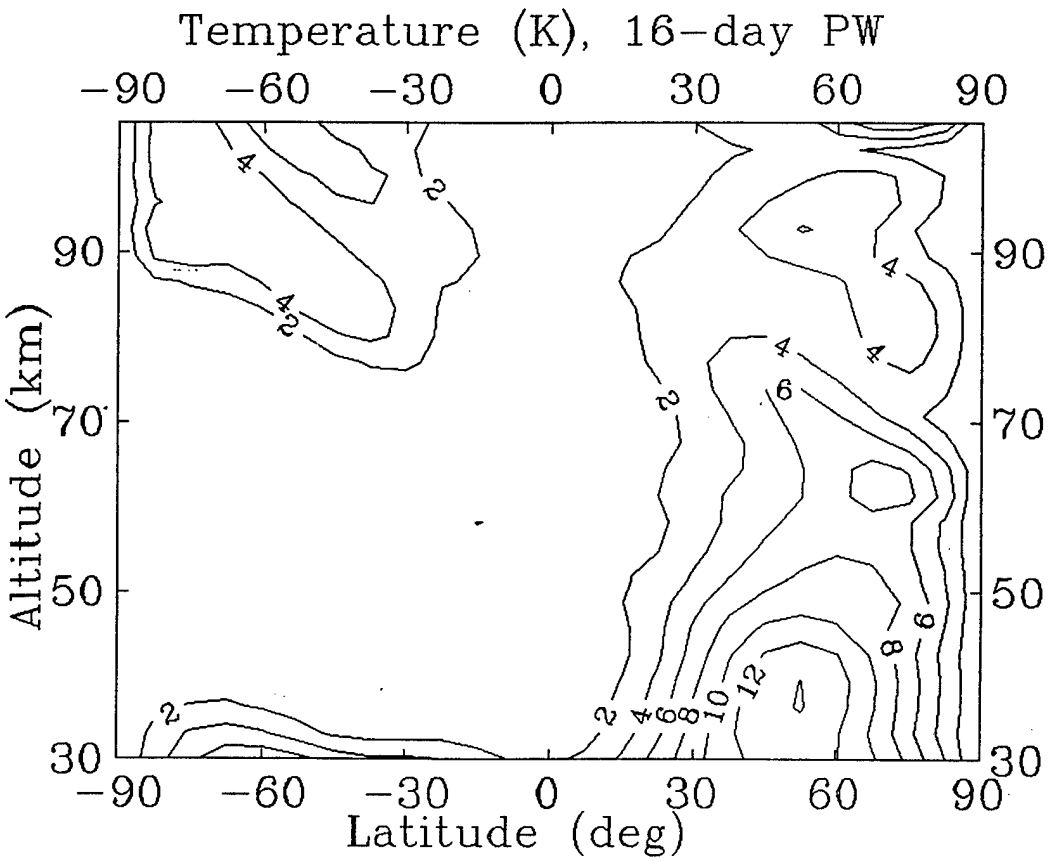

Figure 19: As in Fig. 17, but for the perturbation of temperature.

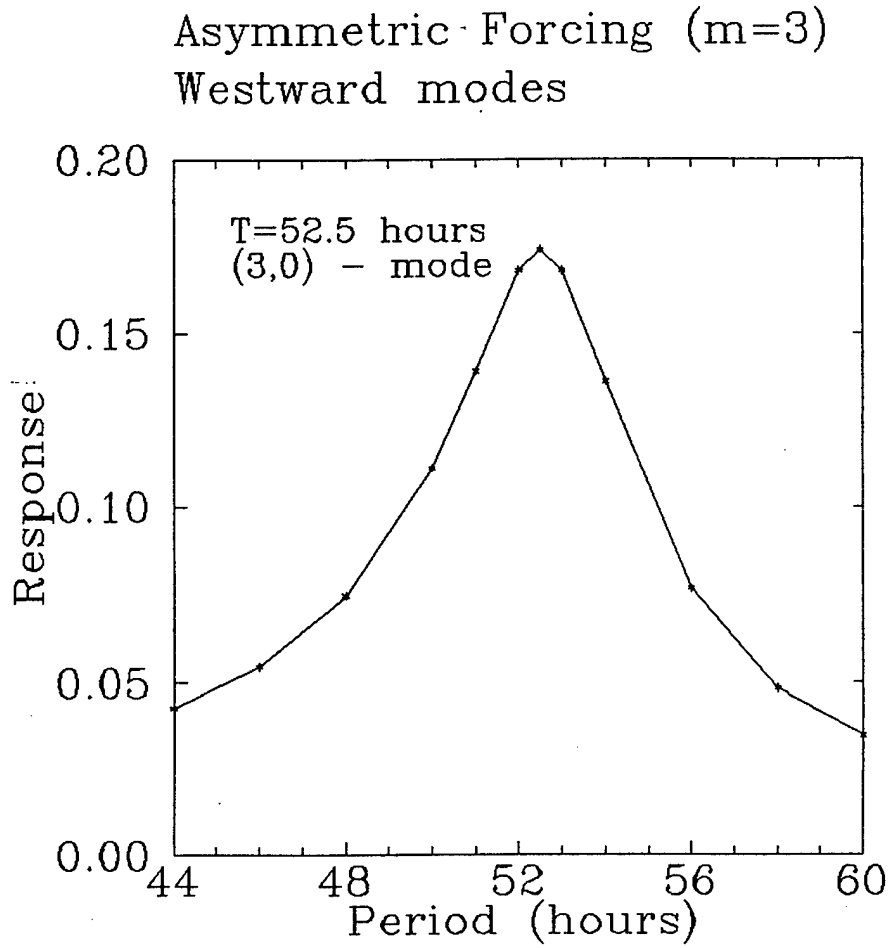

Figure 20: Response to the asymmetric forcing for the westward PWs with m=3.

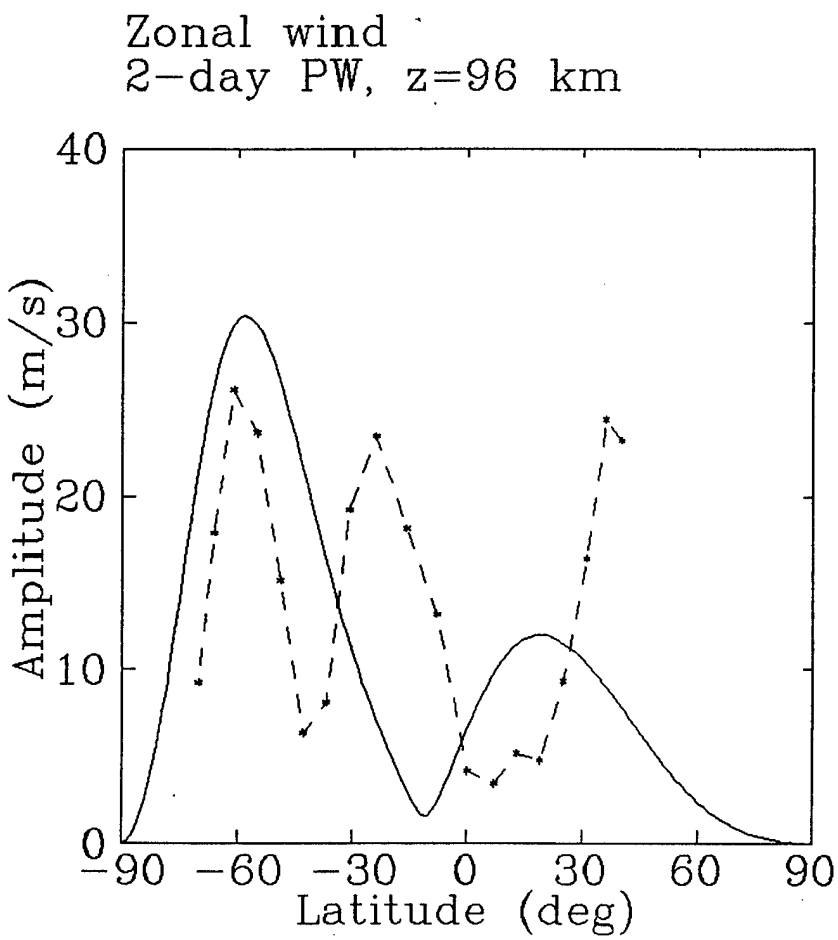

Figure 21: Latitudinal dependencies of the amplitude and phase of the zonal wind perturbation in 2-days PW with zonal wave number m=3 at the altitude z=96 km. Dashed lines show the results obtained from analysis of WINDII data

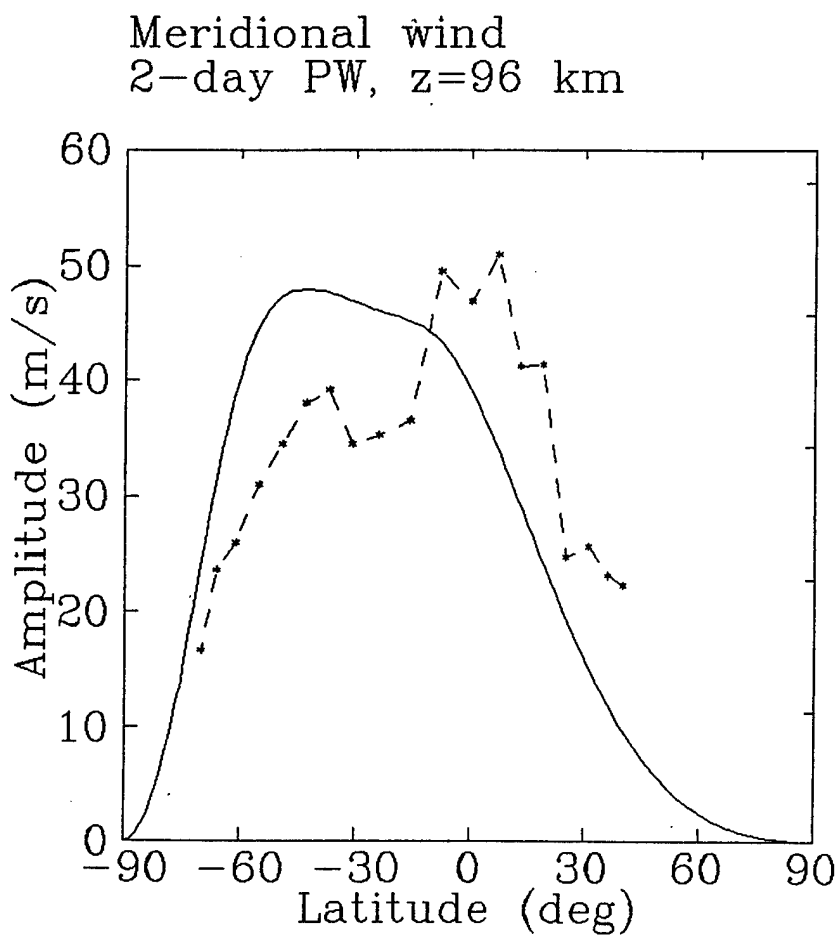

Figure 22: As in Fig. 21, but for the perturbation of meridional wind.

calculated and observed latitudinal variations of the zonal wind is the smoothing of the background wind in the HWM-93 model. The latitudinal structure of the meridional wind shows good agreement between the WINDII data and solution. The latitude-altitude structure of the geopotential height amplitude in 2 days PW is shown in Fig. 23. One can see that 2 days wave propagates from the equatorial stratosphere into the lower thermosphere of the Southern (summer) Hemisphere. The calculated structures of the amplitude of zonal wind, meridional wind, and temperature perturbations due to 2 days PW are shown in Fig. 24-26.

3.9. The Wave-Mean Flow Interaction.

The generalized Eliassen-Palm theorem states that **F** [see (6)] appears as the flux in the wave-activity density conservation law, which can be written for waves of small amplitude α as follows (Andrews and McIntyre, 1976,1978)

$$\partial A/\partial t + \nabla\cdot\mathbf{F} = D + O(\alpha^3), \tag{18}$$

where A, D and $\mathbf{F}$ are mean $O(\alpha^2)$ functions of wave quantities and D vanishes for conservative (i.e. adiabatic, frictionless) waves. Note that in the case of the steady waves $\nabla\cdot\mathbf{F} = D$. Thus, for the steady non-conservative waves $D \neq 0$ and defines the acceleration of the zonally mean flow by the waves.

Andrews (1987) obtained the simple explicit expressions for the wave-activity density A and non-conservative source of wave-activity D, which involve Ertel's potential vorticity, and include only Eulerian quantities

$$A = \rho_0 a \cos\varphi (A_1 + A_2 + A_3), \tag{19}$$

$$A_1 = \frac{1}{2}\rho_0 \overline{\Pi'^2}/\bar{J}, \quad A_2 = \frac{1}{2}\rho_0 (\bar{u}_z/\rho_0)_z \overline{\theta'^2}/\bar{\theta}_z^2, \quad A_3 = -\overline{u_z'\theta'}/\bar{\theta}_z,$$

$$D = \rho_0 a \cos\varphi (D_1 + D_2 + D_3), \tag{20}$$

$$D_1 = \rho_0 \overline{\Pi'\Sigma'}/\bar{J}, \quad D_2 = \rho_0 (\bar{u}_z/\rho_0)_z \overline{\theta' Q'}/\bar{\theta}_z^2, \quad D_3 = -(\overline{X_z'\theta'} + \overline{u_z' Q'})/\bar{\theta}_z,$$

$$\Pi' = P' - \theta' \bar{P}_z/\bar{\theta}_z, \quad \Sigma' = R' - Q'\bar{P}_z/\bar{\theta}_z, \quad \bar{J} = \frac{1}{a}\frac{\partial(\bar{P},\bar{\theta})}{\partial(\varphi, z)} \equiv \frac{1}{a}(\bar{P}_\varphi \bar{\theta}_z - \bar{P}_z \bar{\theta}_\varphi),$$

Ertel's potential vorticity P is given by

$$\rho_0 P = \theta_z \Big[f - \frac{(u\cos\varphi)_\varphi}{a\cos\varphi} + \frac{v_\lambda}{a\cos\varphi} \Big] - \frac{\theta_\lambda v_z}{a\cos\varphi} + \frac{\theta_\varphi u_z}{a}, \tag{21}$$

and Ertel's theorem states that

$$DP/Dt = R, \tag{22}$$

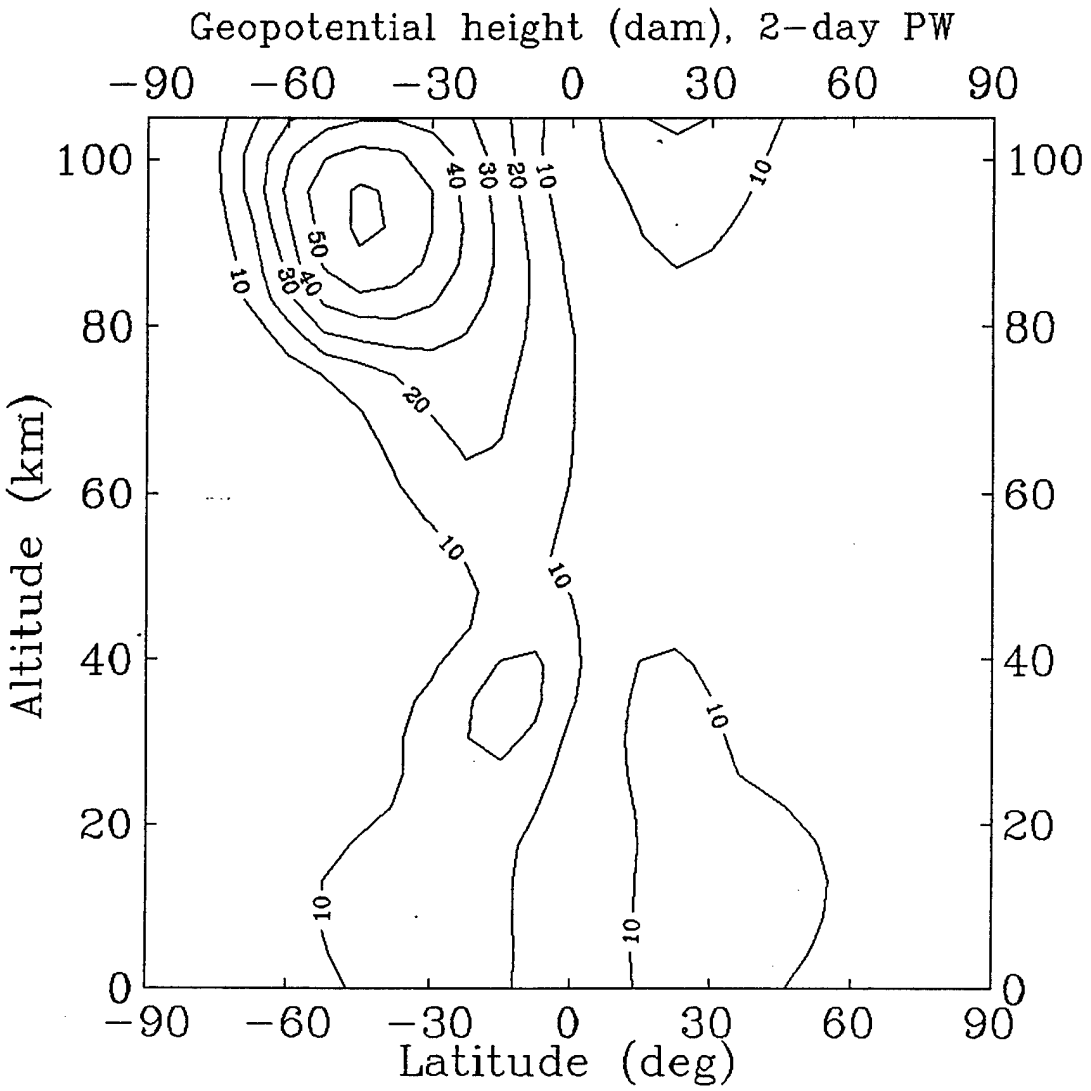

Figure 23: Latitude-height section of amplitude (dam) for the perturbation of the geopotential height in 2-days PW.

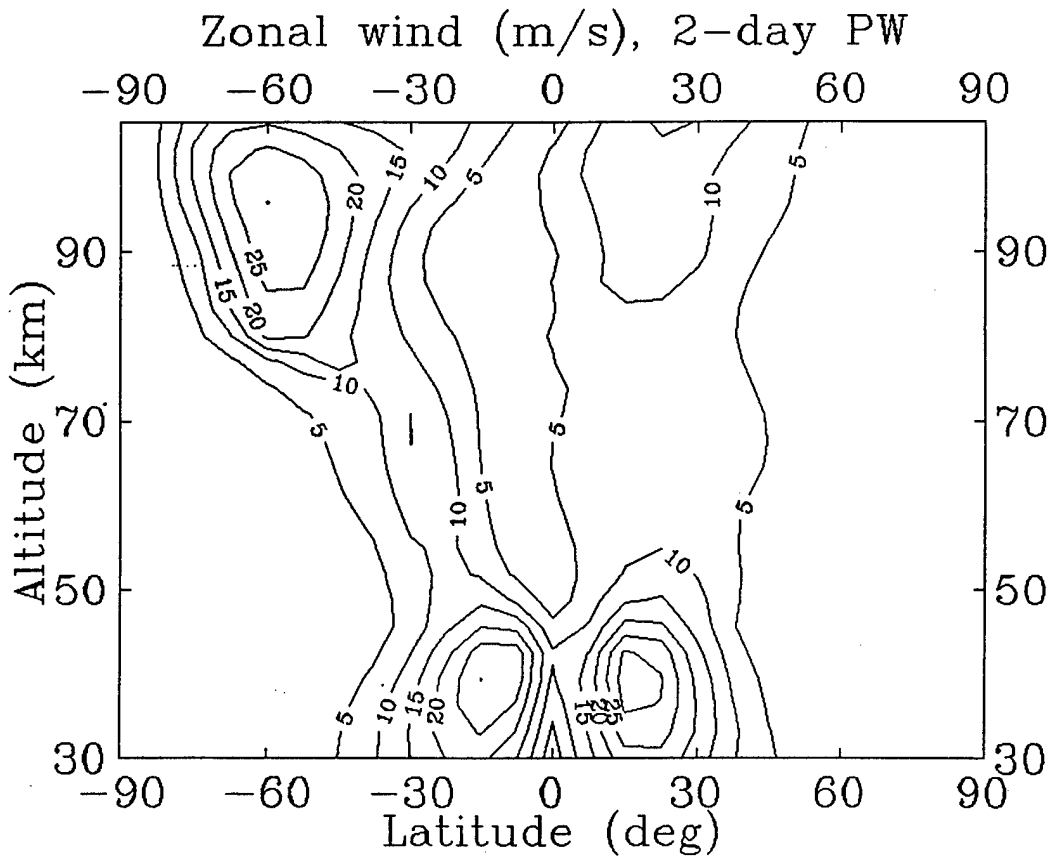

Figure 24: As in Fig. 23, but for the perturbation of zonal wind.

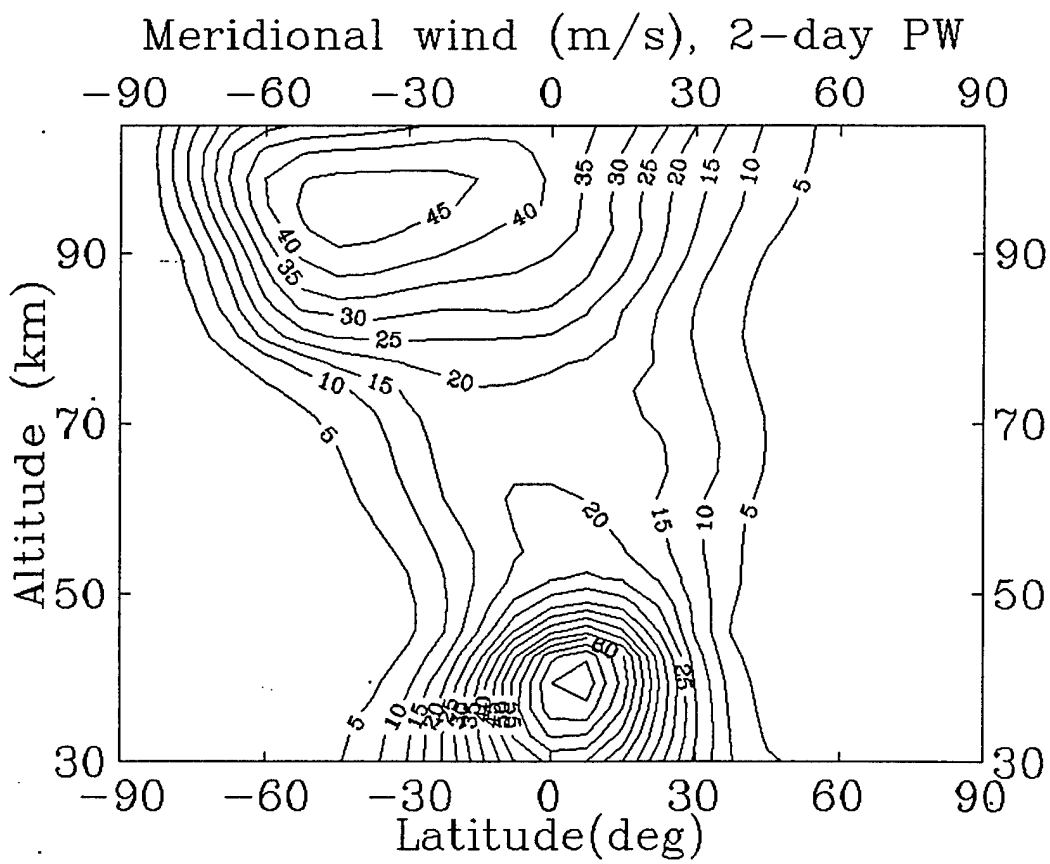

Figure 25: As in Fig. 23, but for the perturbation of meridional wind.

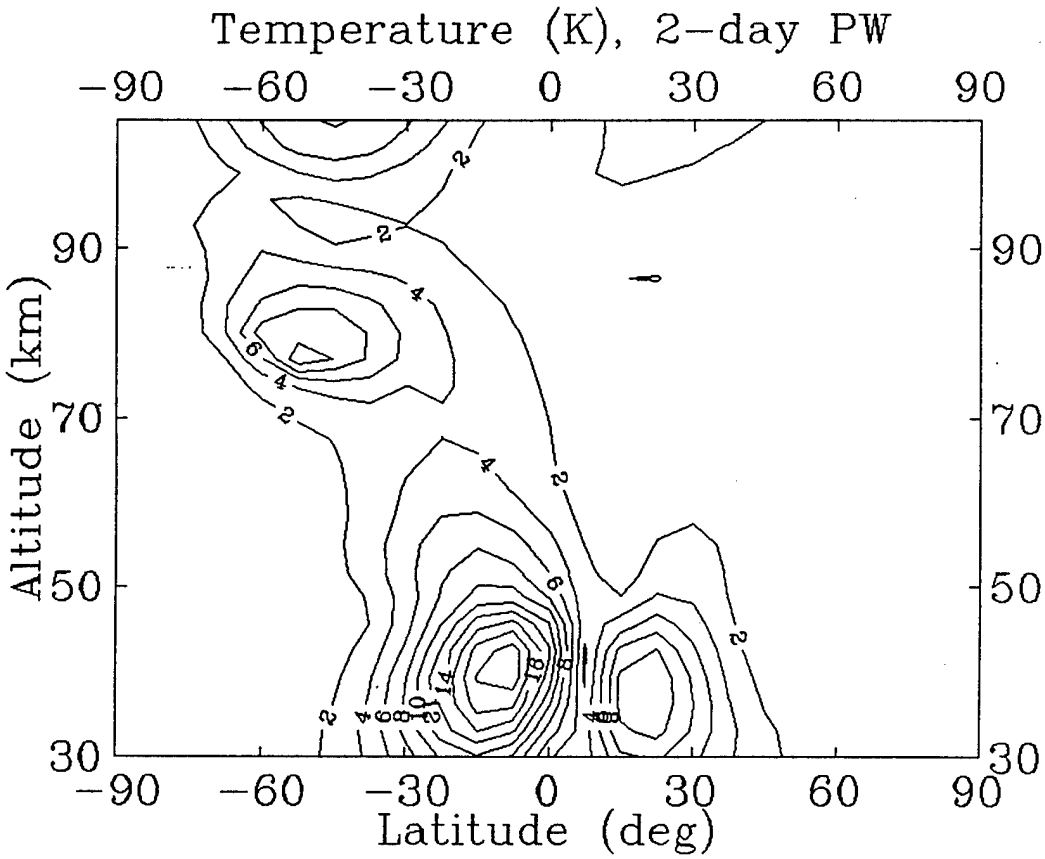

Figure 26: As in Fig. 23, but for the perturbation of temperature.

where D/Dt is the material derivative, and R represents non-conservative effects

$$\begin{aligned}\rho_0 R &= (a\cos\varphi)^{-1}\Big\{-(Y_z\theta + v_z Q)_\lambda + [(X_z\theta + u_z Q)\cos\varphi]_\varphi\Big\} + \\ &+\Big\{(a\cos\varphi)^{-1}[-(X\cos\varphi)_\varphi + Y_\lambda]\theta + \Big[f - \frac{(u\cos\varphi)_\varphi}{a\cos\varphi} + \frac{v_\lambda}{a\cos\varphi}\Big]Q\Big\}_z. \qquad (23)\end{aligned}$$

The expressions for P' and R' are written as follows

$$\rho_0 P' = \frac{\bar{\theta}_z}{a\cos\varphi}[-(u'\cos\varphi)_\varphi + v'_\lambda] + f_1\theta'_z + \frac{\bar{u}_z\theta'_\varphi}{a} + \frac{\bar{\theta}_\varphi u'_z}{a}, \qquad (24)$$

$$\rho_0 R' = \frac{\bar{\theta}_z}{a\cos\varphi}[-(X'\cos\varphi)_\varphi + Y'_\lambda] + f_1 Q'_z + \frac{\bar{u}_z Q'_\varphi}{a} + \frac{\bar{\theta}_\varphi X'_z}{a}. \qquad (25)$$

The divergence of Eliassen-Palm flux can also be calculated using the finite differences. Note that in (φ, z) coordinates

$$\nabla\cdot\mathbf{F} = (F^{(\varphi)}\cos\varphi)_\varphi/(a\cos\varphi) + F_z^{(z)}. \qquad (26)$$

The latitude-height section of the the EP flux divergence [the force per unit mass on the mean flow due to PWs dissipation] for SPW with m=1 are shown in Fig. 27. Our calculations show that in the case of PWs $|A_1| \gg |A_2|, |A_3|$ ($|D_1| \gg |D_2|, |D_3|$), and as a consequence of this fact, the sign of the wave-activity density (and EP divergence) is determined by the sign of $\bar{J}$. The sign of $\bar{J}$ is mainly determined by the sign of the latitudinal gradient of the background Ertel's potential vorticity. As a result, in the region of the negative latitudinal gradient of the Ertel's potential vorticity $A < 0$ and $D > 0$, i.e., we have the eastward acceleration of the zonally averaged flow.

The magnitudes of the accelerations due to the traveling PWs are comparable with the ones due to SPW with m=1. However, if we add together the effects of different westward traveling PWs, the accelerations due to these waves become more significant. In Fig. 28 the force per unit mass on the mean flow due to 2-,5-,10-, and 16-days waves are shown. One can see from this figure that in the mesopause region these accelerations can reach the magnitude about 50 ms^{-1}/day. This value is comparable with the accelerations due to the internal gravity waves and atmospheric tides breakdown and/or saturation (Lindzen, 1981).

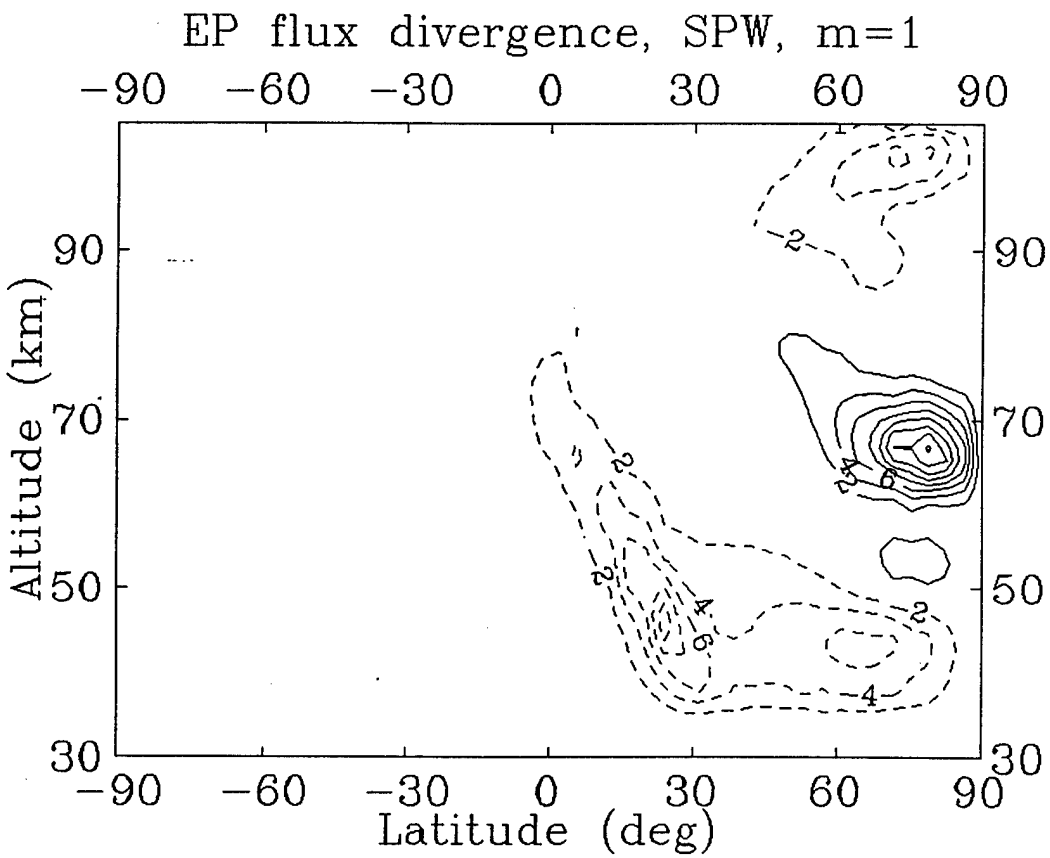

Figure 27: $\nabla \cdot \mathbf{F}/(\rho_0 a \cos\varphi)$ – the force per unit mass on the mean flow due to SPW (m=1) dissipation. Contour interval is 2 m/s, solid contours are positive, dashed negative and zero contour is removed.

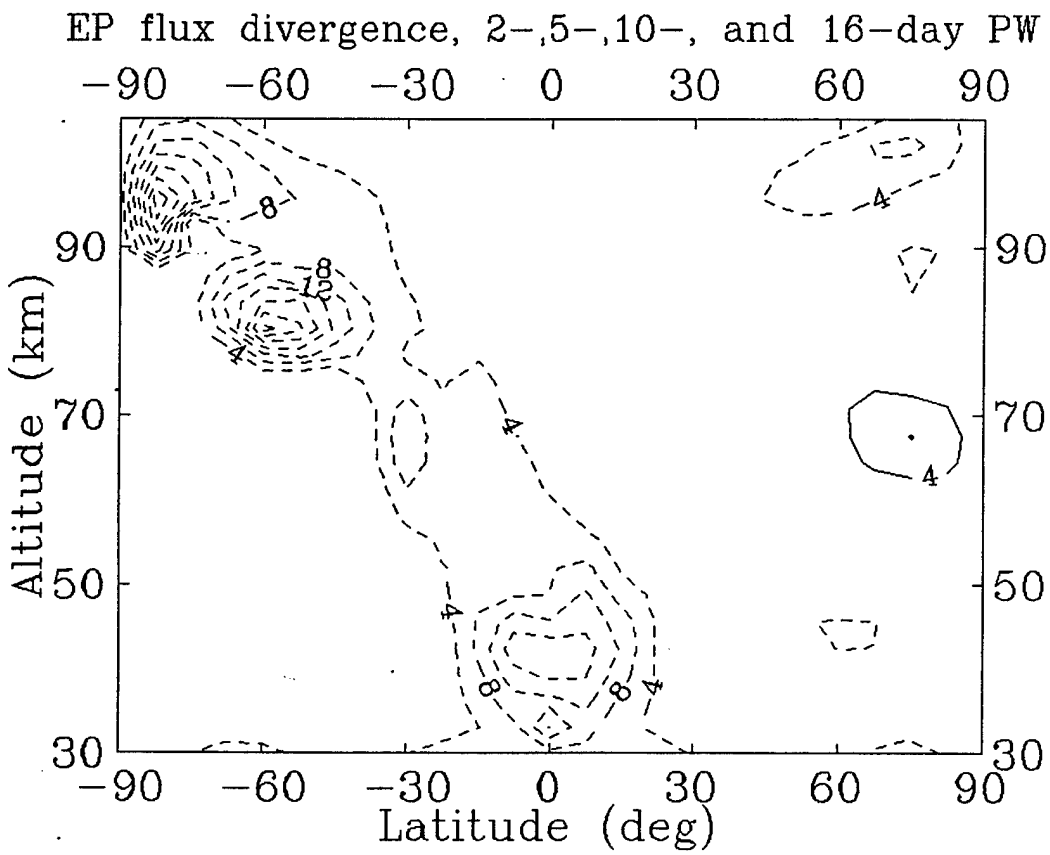

Figure 28: $\nabla \cdot \mathbf{F}/(\rho_0 a \cos\varphi)$ – the force per unit mass on the mean flow due to westward traveling 2-,5-,10-,16-days waves. Contour interval is 4 m/s, solid contours are positive, dashed negative and zero contour is removed.

3.10. Main Results

The results of simulations with the numerical model of the SPW and traveling PWs structure can be formulated as follows

- There is a good qualitative agreement between the results of simulation of the planetary waves and the available experimental data.
- The latitudinal structures of PWs in the middle atmosphere are strongly dependent on the distribution of the background wind, and to provide the detailed comparison of the results of simulation with the characteristics of PWs obtained from experimental data, it is necessary to use (and develop) the background wind models taking into consideration the local latitudinal variations of the zonally averaged wind.
- There is the experimental support (westward slope of the phase) of the cross equatorial propagation of the stationary PWs from the winter stratosphere into the summer lower thermosphere through the westerlies in the low latitude mesosphere, and the question about the existance of eastward zonal wind in this region is crucial for our understanding of the dinamical interaction between Hemispheres.
- Planetary waves can provide the substancial accelerations of the zonally averaged flow in the mesosphere and lower thermosphere so that to simulate the general circulation of these regions it is necessary to develop three dimensional models.
- The magnitude of the perturbations of the meteorological parameters due to presence of PWs in the mesopause region is sufficient to be registrated by satellite and ground-based instruments.

Acknowledgements – This work is sponsored in part by EOARD under Special Contract No SPC-97-4017, and by Grant No 95-0989 from INTAS-RFBR. The author acknowledges the time and effort of W.E.Ward and D.Y.Wang who collected and processed the WINDII data used in this paper.

REFERENCES

Andrews D.G. Wave - mean flow interaction in the middle atmosphere.- Adv. Geophys., 1985, Vol. 28A, p. 244-275.

Andrews D.G. On the interpretation of the Eliassen-Palm flux divergence.- Quart. J. Roy. Meteorol. Soc., 1987, Vol. 113, p. 323-338.

Andrews D.G., McIntyre M.E. Planetary waves in horisontal and vertical shear: the generalized Eliassen-Palm relation and the zonal acceleration.- J. Atmos. Sci., 1976, Vol. 33, No. 11, p.2031-2053.

Andrews D.G., McIntyre M.E. Generalized Eliassen-Palm and Charney-Drazin theorems for waves on axisymmetric mean flows in compressible atmosphere.- J. Atmos. Sci., 1978, Vol. 35, No. 2, p. 175-185.

Barnett J.J., Corney M. Planetary waves. Climatological distribution.- Handbook for MAP, 1985, Vol. 16, p. 86-137.

Boyd J.P. The noninteraction of waves with the zonally averaged flow on a spherical Earth and the interrelationships of energy, heat and momentum.- J. Atmos. Sci., 1976, Vol. 33, No. 11, p. 2285-2291.

Hedin A.E. Extension of the MSIS thermosphere model into the middle and lower atmosphere.- J. Geophys. Res., 1991, Vol. 96, No A2, p. 1159-1172.

Hedin et al. Revised global model of thermosphere winds using satellite and ground-based observations.- J. Geophys. Res., 1991, Vol. 96, p. 7657-7688.

Hedin A.E. et al., Empirical wind model for the upper, middle and lower atmosphere.- J. Atmos. Terr. Phys., 1996, Vol. 58, No 13, p. 1421-1447.

Kirushov B.M. Meridional structure of stationary planetary waves in the middle atmosphere.- Trudy Tsent.Aerol.Obs. U.S.S.R., 1988, Vol. 167, p. 11-15, in Russian.

Kockarts G. Nitric oxide cooling in the terrestrial thermosphere.- Geophys.Res.Lett., 1980, Vol. 7, p. 137-140.

Lieberman R.S. et al., Zonal mean winds in the equatorial mesosphere and lower thermosphere observed by the High Resolution Doppler Imager.- Geophys. Res. Lett., 1993, Vol. 20, No 24, p. 2849-2852.

Lindzen R.S. Turbulence and stress owing to gravity wave and tidal breakdown.- J.Geophys.Res., 1981, Vol. C86, p. 9707-9714.

Linzen R.S. and Blake D. Lamb waves in the presence of realistic distribution of temperature and dissipation.- J. Geophys. Res., 1972, Vol. 77, p. 2166-2176.

Longuet-Higgins M.S. The eigenfunctions of Laplace's tidal equation over a sphere.- Philos. Trans. R. Soc. London, 1968, Ser. A, Vol. 262, p. 511-607.

Pogoreltsev A.I. and Sukhanova S.A. Simulation of the global structure of stationary planetary waves in the mesosphere and lower thermosphere.- J.Atmos.Terr.Phys., 1993, Vol. 55; No. 1, p. 33-40.

Salby M.L. Rossby normal modes in nonuniform background configurations. Part II. Equinox and Solstice conditions.- J.Atmos.Sci., 1981, Vol. 38, No. 9, p. 1827-1840.

Schoeberl M.R. and Clark R., Resonant planetary waves in a spherical atmosphere.- J.Atmos.Sci., 1980, Vol. 37, No. 1, p.20-28.

Shepherd G.G. et al., Longitudinal structure in atomic oxygen concentrations observed with WINDII on UARS.- Geophys. Res. Lett., 1993, Vol. 20, No 12, p. 1303-1306.

Smith A.K. Wave transience and wave mean flow interaction caused by the interference of stationary and traveling waves.- J.Atmos.Sci., 1985, Vol. 42, 529-535.

Smith A.K. Observed correlation of longitudinal variations in stratosphere and mesosphere wind.- Submitted to J.Atmos.Sci., June 1995.

Wang D.Y. et al. Empirical model of 90-120 km horizontal winds from wind-imaging interferometer green line measurements in 1992-1993.- J. Geophys. Res., 1997, Vol. 102, No. D6, p. 6729-6745.

Ward W.E., Wang D.Y., Solheim B.H., and Shepherd G.G. Observations of the two-day wave in WINDII data during January, 1993.- Geophys. Res. Lett., 1996, Vol. 23, No. 21, p. 2923-2926.

Zhu X. Radiative damping revisited: Parameterization of damping rate in the middle atmosphere.- J. Atmos. Sci., 1993, Vol. 50, p. 3008-3021.